

REPORT DOCUMENTATION PAGE

Form Approved
OMB No. 074-0188

Public reporting burden for this collection of information is estimated to average 1 hour per response, including the time for reviewing instructions, searching existing data sources, gathering and maintaining the data needed, and completing and reviewing this collection of information. Send comments regarding this burden estimate or any other aspect of this collection of information, including suggestions for reducing this burden to Washington Headquarters Services, Directorate for Information Operations and Reports, 1215 Jefferson Davis Highway, Suite 1204, Arlington, VA 22202-4302, and to the Office of Management and Budget, Paperwork Reduction Project (0704-0188), Washington, DC 20503

1. AGENCY USE ONLY (Leave blank)

2. REPORT DATE
9/30/97

3. REPORT TYPE AND DATES COVERED
Final Tech. Report 6/1/93 - 7/31/97

4. TITLE AND SUBTITLE

(U)
Spray Vaporization and Combustion in Large Vortical Structures

5. FUNDING NUMBERS

PE - 61103D
PR - 3484
SA - WS
G - F49620-93-1-0400

6. AUTHOR(S)

Suresh K Aggarwal

7. PERFORMING ORGANIZATION NAME(S) AND ADDRESS(ES)

Department of Mechanical Engineering
(M/C) 251, 842 W. Taylor St.
University of Illinois at Chicago
Chicago, IL 60607

8. PERFORMING ORGANIZATION REPORT NUMBER
AFRL-SR-BL-TR-98-

0102

9. SPONSORING / MONITORING AGENCY NAME(S) AND ADDRESS(ES)

AFOSR/NA
110 Duncan Avenue, Suite B115
Bolling AFB DC 20332-8050

NA

10. SPONSORING / MONITORING AGENCY REPORT NUMBER

11. SUPPLEMENTARY NOTES

12a. DISTRIBUTION / AVAILABILITY STATEMENT

Approved for Public Release; distribution is unlimited

12b. DISTRIBUTION CODE

13. ABSTRACT (Maximum 200 Words)

Numerical studies were performed to investigate interactions between large-scale vortical structures and droplets in two-phase shear flows. A generic configuration consisting of a droplet-laden heated air jet in a coflowing air stream was used to analyze several two-phase flows. A time-accurate, axisymmetric, two-phase algorithm was developed for the simulations. Detailed numerical experiments were used to examine the dispersion of evaporating droplets in the presence of vortex structures, the effects of droplet-vortex interactions on the dynamic and steady structure of nonevaporating and evaporating sprays, and the transient and time-averaged structure of a swirling two-phase jet. Results demonstrated that the dispersion of evaporating droplets can be characterized in terms of their lifetimes and Stokes numbers. In addition, it was shown that for a dispersed- to gas-phase mass loading ratio of unity, the shear-layer stability and mixing behavior can be modulated by changing the droplet injection characteristics. Finally, the simulations of a droplet-laden swirling jet revealed that the dynamics of large scale structures was strongly affected by the amount of swirl imparted to the incoming flow, and that the effects of two-way momentum coupling on jet dynamics and mixing were markedly different for nonswirling and swirling jets.

DTIC QUALITY INSPECTED 3

Direct numerical simulations, Two-Phase flows, Droplet-Vortex interactions, Dispersion of evaporating droplets, Swirl effects on vortex dynamics and structure of two-phase jets

15. NUMBER OF PAGES
94

16. PRICE CODE

17. SECURITY CLASSIFICATION OF REPORT
Unclassified

18. SECURITY CLASSIFICATION OF THIS PAGE
Unclassified

19. SECURITY CLASSIFICATION OF ABSTRACT
Unclassified

20. LIMITATION OF ABSTRACT
UL

NSN 7540-01-280-5500

Standard Form 298 (Rev. 2-89)
Prescribed by ANSI Std. Z39-18
298-102

19980129 069

TABLE OF CONTENTS

SUMMARY.....	1
DESCRIPTION.....	1
Droplet Dispersion and Vaporization in a Heated Jet Shear Layer.....	2
Two-Way Droplet-Vortex Interactions in Non-Reacting Spray Jets.....	3
Dynamics of a Two-Phase Swirling Jet.....	4
Publications.....	4
PROJECT PERSONNEL.....	5
PRESENTATIONS.....	6
INTERACTIONS RELATED TO THE RESEARCH.....	7
COPIES OF REPRINTS.....	8

SPRAY VAPORIZATION AND COMBUSTION IN LARGE VORTICAL STRUCTURES

(AFOSR Grant No. F49620-93-1-0400)

Principal Investigator: Suresh K. Aggarwal
Address: Department of Mechanical Engineering (M/C 251)
University of Illinois at Chicago
Chicago, Illinois 60607

SUMMARY

Numerical studies were performed to investigate interactions between large-scale vortical structures and droplets in a variety of two-phase shear flows. Using a generic configuration consisting of a droplet-laden heated air jet in a coflowing air stream, several two-phase flows were analyzed. These included a low-speed buoyancy-dominated two-phase jet, an inertial-dominated jet, and a swirling two-phase jet. A time-accurate, axisymmetric, two-phase algorithm was developed for the simulations. Detailed numerical experiments were used to examine (i) the dispersion of nonevaporating and evaporating droplets in the presence of large vortex structures, (ii) the dynamic structure of nonevaporating and evaporating sprays under the influence of droplet-vortex interactions, and (iii) the dynamic and time-averaged structure of a swirling two-phase jet. Results indicated that while the dispersion of nonevaporating droplets is characterized in terms of the Stokes number, that of evaporating droplets is determined by both the Stokes number and the ratio of droplet lifetime to its response time. Simulations dealing with the two-way coupling indicated that both the dynamic and time-averaged spray behavior is strongly influenced by the two-way coupling between vortex structures and droplets, and is governed by the dispersed-phase to gas-phase mass loading ratio. In addition, it was demonstrated that the shear-layer stability and the mixing characteristics can be modulated by changing the droplet injection characteristics. Finally, the simulations of a droplet-laden swirling jet indicated that the dynamics of large scale structures is strongly affected by amount of swirl (characterized by the swirl number) imparted to the incoming flow, and that the effects of momentum coupling on the dynamic and time-averaged jet behavior are markedly different for nonswirling and swirling jets.

DESCRIPTION

Particle-laden turbulent flows occur in numerous technological applications. The traditional approach for modeling these flows is based on the assumption that the turbulence is isotropic and statistical in nature. Numerous recent studies, however, indicate that the turbulent flows are dominated by large-scale coherent vortical structures. This has raised a number of important questions regarding the role of large-scale structures and their interactions with droplet sprays in determining the entrainment, mixing, and spray processes. Further interest in the study of large scale structures stems from the fact that by manipulating the dynamics of large structures and their interactions with droplets, one may be able to enhance the performance of systems whose dynamics is strongly influenced by these interactions.

The objective of this research was to study the dynamics of two-way interactions between large-scale vortex structures and droplets in shear layers. The transient, two-way interactions pertain to the effect of vortical structures on dispersion and vaporization of droplet, which in turn affect the local state of the gas-phase mixture and thereby the dynamics of two-phase system under consideration. In reacting sprays, the flame dynamics and pollutant formation can be strongly influenced by these interactions. The study of droplet-vortex interactions also provides a

basic building block to the understanding of droplet-turbulence interactions in turbulent two-phase flows. In addition, a fundamental understanding of such interactions is important for devising passive and active control strategies for improving combustor performance.

In the present study, we first investigated the effects of vortex structures on droplet dispersion and vaporization behavior in a heated jet shear layer. Then, a two-way coupled spray system was simulated in order to examine droplet-vortex interactions and effects of these interactions on the dynamic and time-averaged characteristics of nonevaporating and evaporating sprays jets. Finally, the dynamics of a droplet-laden swirling jet was simulated to examine the effects of swirl and two-phase momentum coupling on the swirling jet dynamics and structural characteristics. Results obtained so far are summarized in the following sections.

Droplet Dispersion and Vaporization in a Heated Jet Shear Layer

This study was directed at examining the effect of vaporization on droplet dispersion in the presence of large-scale vortex structures. Most previous studies have focused on the dispersion of solid particles (or nonevaporating droplets), and shown that the presence of large vortex structures leads to a size-dependent dispersion behavior, such that the droplets with response time on the order of relevant vortex time exhibit the maximum dispersion. In many applications, especially those involving spray combustion, the size of a droplet may change significantly during its interaction with a vortex, i.e. the droplet lifetime may be of the same order of magnitude as the droplet-vortex interaction time. It is therefore relevant to investigate the effect of size change on droplet dispersion.

Dispersion behavior of nonevaporating and evaporating droplets was investigated by continuously injecting single-sized n-heptane droplets from a given location into the shear layer of an axisymmetric heated jet issuing into a cold co-annular flow. Both the buoyancy-induced and the shear-induced (Kelvin-Helmholtz) instabilities were considered. For the low-speed case (case 1), the jet velocity was 1 m/s yielding a Reynolds number 150, and large toroidal vortices appeared naturally due to the buoyancy-induced instability of the heated jet. For the high-speed jet (case 2), the jet velocity was 5.0 m/s, and vortex structures were generated due to the Kelvin-Helmholtz instability. In both cases, the dispersion of nonevaporating droplet was characterized by a Stokes number (St) defined as the ratio of the particle response time to the characteristic eddy time, and the maximum dispersion was observed near St of unity. The characteristic eddy time corresponded to the vortex passage frequency for case 1, and the vortex pairing frequency for case 2. The difference was attributable to the fact that while vortex pairing was most responsible for the size-selective dispersion behavior for case 2, the shear layer dynamics of case 1 did not involve any vortex pairing. The effect of vaporization on dispersion was analyzed by using simultaneous snapshots of the flow and evaporating droplets. It was observed that the dispersion of smaller- and medium-sized droplets was significantly modified due to the vaporization process. For case 1, the interaction of nonevaporating droplets with the first and second vortices determined their dispersion behavior. The small- and medium-sized droplets were entrained by the first vortex, and while the small-sized droplets remained within the vortex core, the medium-sized droplets were centrifuged out of the second vortex, which resulted in their enhanced dispersion. For the corresponding evaporating case, there was significant vaporization of both the small-sized and the medium-sized droplets during their interaction with the first and second vortices. As a result, small-sized droplets evaporated almost completely during the interaction, and their dispersion approached that of fluid particles, while medium-sized droplets also evaporated significantly, such that they were not centrifuged out of the second vortex, and exhibited reduced dispersion compared to that of nonevaporating droplets. On the other hand, the large-sized nonevaporating droplets were not entrained by the first vortex and hence were not dispersed in the neighborhood of the second vortex. In addition, due to a relatively small change in their size, the vaporization did not significantly affect their dispersion behavior. For case 2, the effect of vaporization on the size-selective dispersion process was qualitatively similar to that in case 1, except that the vortex pairing process, which was absent in

case 1, played a dominant role in case 2. More detailed results and discussion are provided in Publications No. 1-3.

Two-Way Droplet-Vortex Interactions in Non-Reacting Spray Jets

The objective of this study was to investigate the processes of two-way, droplet-vortex interactions, and the effects of these interactions on the structure and dynamics of two-phase shear flows. The simulations considered an axisymmetric spray formed between a low-speed, droplet-laden heated nitrogen jet and a coflowing air stream. In order to isolate the effects due to interphase momentum coupling from those due to mass and energy couplings, both non-evaporating and evaporating sprays were considered. Two cases were simulated, one involving a low-speed jet (Reynolds number = 150) where large-scale structures were generated by using the buoyancy-induced instability, and the other involving a jet with a Reynolds number of 750, where large structures were generated by the shear-induced (Kelvin-Helmholtz) instability. The effect of droplets on the dynamics of large structures was investigated by varying the spray injection characteristics and liquid-to-gas mass loading ratio (M), defined as the ratio of the liquid fuel mass flow rate to the nitrogen mass flow rate in the jet. Important observations were as follows:

- 1) For both non-evaporating and evaporating sprays, the effect of dispersed phase on vortex dynamics was generally negligible for M less than 0.5. In other words, with regard to the dynamic and time-averaged spray behavior, there were no discernible differences between one-way and two-way coupled systems. However, at higher loading ratios, the vortex dynamics as well as the spray behavior were strongly influenced by the dispersed phase. In addition, it was observed that for a given M , the effect of dispersed phase on the two-phase shear layer could be modified considerably by changing the spray injection characteristics.
- 2) For the low-speed jet, the dispersed phase modified the dynamics of vortex structures but not the time-average behavior of a non-evaporating spray, while it modified both the dynamics and time-averaged behavior for an evaporating spray. For example, for 200- μm spray at $M=1.0$ and with droplets injected into the shear layer, the vortex passage frequency was increased by about 30 % and the vortex structures became weaker and less coherent compared to the gaseous jet case. Results also indicated a strong influence of spray injection characteristics on the processes of droplet-vortex interactions, and thereby on the dynamic structure of the jet shear layer. The detailed results are discussed Publications No. 4.
- 3) For the higher Reynolds number jet with loading ratio of unity, the simulations for a two-way coupled non-evaporating spray indicated that the locations of shear layer rollup, vortex formation and pairing were shifted downstream, and their frequencies were reduced compared to those for the one-way coupled system. In addition, it was demonstrated that the shear layer stability could be modulated by changing the droplet injection characteristics. For example, the shear layer stability was enhanced by injecting droplets at lower velocities compared to the jet, or diminished by increasing the droplet injection velocity compared to the jet. For the corresponding evaporating spray, the effects of two-way coupling were much more complex compared to that for a non-evaporating spray. In general, the dynamics of vortex structures and shear layer in a evaporating spray became much less organized compared to that in a nonevaporating spray. Clearly, the implications of these results would be significant with regard to spray applications, such as gas turbine combustors and liquid propellant rocket engines, where the system performance is strongly linked to some underlying unsteady phenomenon. Further details are provided in Publications No. 5-6.

Dynamics of A Two-Phase Swirling Jet

Numerical simulations of a two-phase swirling jet focused on the dynamic and time-averaged characteristics of single-phase and two-phase swirling jets. Results for the single-phase swirling jet at a Reynolds number of 800 indicated that the dynamics of large scale structures is strongly affected by the degree of swirl (characterized by a swirl number S) imparted to the incoming flow. For low and intermediate swirl intensities ($S < 0.5$), the vortex rings rollup occurred closer to the nozzle exit, their frequency increased, and pairing interactions became stronger as the swirl number (S) was increased. Essentially, swirl modified vortex dynamics in a way that it enhanced the shear layer growth entrainment rates. As the swirl number was increased further (strongly swirling jet), the numerical results indicated the presence of a central stagnant zone and recirculation bubble, which modified vortex dynamic drastically and caused a dramatic increase in the jet spreading angle. The structure of the two-phase swirling jet was found to be strongly influenced by both the interphase momentum coupling and swirl intensity. For the nonswirling case, the momentum coupling modified the dynamics of large vortex structures, including their rollup location and frequency, causing enhanced mixing and entrainment of colder fluid into the shear layer. In contrast, for weakly and moderately swirling two-phase jets ($S < 0.5$), the momentum coupling reduced the shear layer growth, as well as mixing and entrainment rate. At higher swirl numbers, the momentum-coupling effect was found to be even stronger, manifested by the reduced rate of decay of gas velocity and temperature along the jet axis. In addition, the relation between rollup frequency and swirl was modified compared to that for the single-phase jet. Further details are provided in Publications No. 7-8.

The dispersion behavior of nonevaporating and evaporating droplets in a swirling axisymmetric jet was also investigated. The objective was to characterize the effects of swirl and vaporization on droplet dispersion. For all the swirl cases investigated, the droplet dispersion exhibited a non-monotonic behavior, with the maximum dispersion occurring at Stokes numbers on the order of unity. With an increase in the swirl number, the radial dispersion of both nonevaporating and evaporating droplets was significantly enhanced. The effect of vaporization on droplet dispersion was characterized in terms of a droplet lifetime compared to its response time and a characteristic flow (vortex) time. For the conditions investigated, the dispersion of evaporating droplets was noticeably reduced compared to the nonevaporating case. In addition, the dispersion function versus Stokes number (St) behavior was modified due to vaporization. These results are discussed in Publication No. 9.

Publications

1. T.W. Park, S.K. Aggarwal, and V.R. Katta, "Effect of Gravity on the Structure of an Unsteady Spray Diffusion Flame," Combustion and Flame, Vol. 99, pp. 767-774, 1994, Also presented at the 25th (International) Symposium on Combustion, Irvine, California, August 1-5, 1994.
2. S.K. Aggarwal, "Dynamics of Droplets and Sprays in Vortical Flows, "Invited Presentation at the IUTAM Symposium on Mechanics and Combustion of Droplets and Sprays, Tainan, Taiwan, R.O.C., December 6-10, 1994.
3. T.W. Park, S.K. Aggarwal, and V.R. Katta, "Gravity Effect on the Dynamics of Evaporating Droplets in a Heated Jet," AIAA Journal of Propulsion & Power, Vol. 11, No.3, pp. 519-528, 1995.
4. T.W. Park, S.K. Aggarwal, and V.R. Katta, "A Numerical Study Of Droplet-Vortex Interactions In an Evaporating Spray," International J. of Heat & Mass Transfer, Vol. 39, No. 11, pp. 2205-2219, 1996.

5. S.K. Aggarwal, T.W. Park, and V.R. Katta, "Unsteady Spray Behavior In a Heated Jet Shear Layer," 15th ICDERS Meeting, Boulder, Colorado, July 31-Aug. 4, 1995.
6. S.K. Aggarwal, T.W. Park, and V.R. Katta, "Unsteady Spray Behavior in a Heated Jet Shear Layer: Droplet-Vortex Interactions," Combustion Science and Technology Vol. 113-114, pp. 429-450, 1996.
7. T.W. Park, S.K. Aggarwal, and V.R. Katta, "Momentum-Coupling Effects in a Two-Phase Jet," presented at the 26th International Symposium on Combustion, Naples, Italy, August 2-5, 1996.
8. T.W. Park, S.K. Aggarwal, and V.R. Katta, "On The Dynamics of a Two-Phase Swirling Jet," Int. J. Multiphase Flow, to appear.
9. S.K. Aggarwal and T.W. Park, "Droplet Dispersion in an Axisymmetric Heated Swirling Jet," Twenty-Seventh Symposium (International) on Combustion, The Combustion Institute, Pittsburgh. (under review).

PROJECT PERSONNEL

Suresh K. Aggarwal was the principal investigator. In addition, two graduate students were directly involved in the project. The first student, Mr. T.W. Park, completed his Ph.D. Dissertation in 1995. His research focused on the dynamics of two-way interactions between large-scale vortex structures and droplets in evaporating and reacting sprays. First, one-way interactions, pertaining to the effects of large-scale vortex structures on the dispersion of nonevaporating and evaporating droplets, were investigated. A detailed, multidimensional two-phase algorithm was developed during this investigation. Then, the research examined the processes of two-way, droplet-vortex interactions, and the effects these interactions have on the structure and dynamics of nonreacting and reacting spray jets. Another student, Mr. D. Brandon, is expected to complete his M.S. Dissertation this semester.

PUBLICATIONS

1. T.W. Park, "Numerical Analysis of Droplet-Vortex Interactions in Nonreacting and Reacting Spray Jets," Ph.D. Thesis, Department of Mechanical Engineering, The University of Illinois at Chicago, 1995.
2. T.W. Park, S.K. Aggarwal, and V.R. Katta, "Effect of Gravity on the Structure of an Unsteady Spray Diffusion Flame," Combustion and Flame, Vol. 99, pp. 767-774, 1994. Also presented at the 25th (International) Symposium on Combustion, Irvine, California, August 1-5, 1994.
3. T.W. Park, S.K. Aggarwal, and V.R. Katta, "Gravity Effect on the Dynamics of Evaporating Droplets in a Heated Jet," AIAA Journal of Propulsion & Power, Vol. 11, No.3, pp. 519-528, 1995.
4. S.K. Aggarwal, "Dynamics of Droplets and Sprays in Vortical Flows," Invited Presentation at the IUTAM Symposium on Mechanics and Combustion of Droplets and Sprays, Tainan, Taiwan, R.O.C., December 6-10, 1994.
5. T.W. Park, S.K. Aggarwal, and V.R. Katta, "A Numerical Study Of Droplet-Vortex Interactions In an Evaporating Spray," International J. of Heat & Mass Transfer, Vol. 39, No. 11, pp. 2205-2219, 1996.

6. S.K. Aggarwal, T.W. Park, and V.R. Katta, "Unsteady Spray Behavior In a Heated Jet Shear Layer," 15th ICDERS Meeting, Boulder, Colorado, July 31-Aug. 4, 1995.
7. S.K. Aggarwal, T.W. Park, and V.R. Katta, "Unsteady Spray Behavior in a Heated Jet Shear Layer: Droplet-Vortex Interactions," Combustion Science and Technology Vol. 113-114, pp. 429-450, 1996.
8. T.W. Park, S.K. Aggarwal, and V.R. Katta, "Momentum-Coupling Effects in a Two-Phase Jet," Proceedings of the 1996 Technical Meeting of the Central States Section of The Combustion Institute, St. Louis, Missouri, May 5-7, 1996.
9. T.W. Park, S.K. Aggarwal, and V.R. Katta, "On The Dynamics of a Two-Phase Swirling Jet," Int. J. Multiphase Flow, to appear.
10. S.K. Aggarwal and T.W. Park, "Droplet Dispersion in an Axisymmetric Heated Swirling Jet," Twenty-Seventh Symposium (International) on Combustion, The Combustion Institute, Pittsburgh. (under review).

PRESENTATIONS

Seven conference papers were presented at various national and international meetings. These include presentations at the Central States Meeting of the Combustion Institute, the 25th (International) Symposium of the Combustion Institute, AIAA 30th Joint Propulsion Conference, AIAA 35th Aerospace Sciences Meeting, the 15th ICDERS Meeting in Boulder, Colorado, and an invited presentation at the IUTAM Symposium on Mechanics and Combustion of Droplets and Sprays in Tainan, Taiwan, R.O.C. In addition, P.I. presented invited seminars at the Naval Research Laboratory, Wright-Patterson Air Force Base, National Institute of Standards and Technology, and the University of Illinois at Urbana-Champaign.

1. T.W. Park, S.K. Aggarwal, and V.R. Katta, "A Numerical Investigation on the Dynamics of Laminar Spray Flames Under the Influence of Gravity," Paper AIAA-94-3276, 30th Joint Propulsion Conference, Indianapolis, June 27-29, 1994.
2. T.W. Park, S.K. Aggarwal, and V.R. Katta, "Effect of Gravity on the Structure of an Unsteady Spray Diffusion Flame," 25th (International) Symposium on Combustion, Irvine, California, August 1-5, 1994.
3. S.K. Aggarwal, "Dynamics of Droplets and Sprays in Vortical Flows," Invited Presentation at the IUTAM Symposium on Mechanics and Combustion of Droplets and Sprays, Tainan, Taiwan, R.O.C., December 6-10, 1994.
4. S.K. Aggarwal, T.W. Park, and V.R. Katta, "Unsteady Spray Behavior In a Heated Jet Shear Layer," Central States/Western States/Mexican National Sections Meeting of The Combustion Institute, San Antonio, Texas, April 23-26, 1995.
5. S.K. Aggarwal, T.W. Park, and V.R. Katta, "Unsteady Spray Behavior In a Heated Jet Shear Layer," 15th ICDERS Meeting, Boulder, Colorado, July 31-Aug. 4, 1995.
6. T.W. Park, S.K. Aggarwal, and V.R. Katta, "Momentum-Coupling Effects in a Two-Phase Jet," presented at the 26th International Symposium on Combustion, Naples, Italy, August 2-5, 1996.

7. T.W. Park, S.K. Aggarwal, and V.R. Katta, "Momentum-Coupling Effects in a Two-Phase Swirling Jet," Paper 97-0259, AIAA 35th Aerospace Sciences Meeting, Reno, Nevada, Jan. 6-9, 1997.

INTERACTIONS RELATED TO THE RESEARCH

The research involved active interactions with the personnel at Wright-Patterson Air Force Base (WPAFB), Ohio. In particular, Dr. M. Roquemore and Dr. V. R. Katta actively collaborated on this research. The collaboration, which resulted in several journal and conference papers, is continuing in a productive manner. Dr. Roquemore also served on the Ph.D. thesis committee of Mr. T.W. Park. Another notable outcome of this interaction was that Dr. T. W. Park received a NRC Post-Doctoral Research Fellowship and worked with Dr. Roquemore at the WPAFB.

Effect of Gravity on the Structure of an Unsteady Spray Diffusion Flame

T. W. PARK and S. K. AGGARWAL*

Department of Mechanical Engineering, University of Illinois at Chicago, Chicago, IL 60607

and

V. R. KATTA

Systems Research Laboratories, Inc., A Division of Arvin/Calspan, 2800 Indian Ripple Road, Dayton, OH 45440-3696

In this paper, we present time-dependent axisymmetric numerical simulation of an unsteady *n*-heptane spray flame, and examine the effects of gravity on the flame structure. The flame is formed between a droplet-laden nitrogen jet and a coflowing air stream. A detailed, multidimensional two-phase algorithm is developed for the simulation. The gas-phase model includes a one step global chemistry model, multicomponent diffusion, and variable transport properties. A comprehensive vaporization model is employed to calculate the instantaneous droplet size and surface temperature along the trajectory of each droplet group. The model includes the effects of variable thermophysical properties and nonunity Lewis number in the gas film, the effect of Stefan flow on the heat and mass transfer between the droplet and the gas, and the transient liquid heating. Results indicate that the laminar spray flame structure is strongly influenced by gravity. Large-scale buoyancy-driven structures are observed outside the flame surface, similar to those in a gaseous jet diffusion flame. These outer structures develop naturally and sustain themselves without any external excitation. Results also indicate the occurrence of strong two-way interactions between droplets and large structures. The large vortex structures cause droplets to disperse radially outward, and this in turn modifies the vortex dynamics. The dynamics of spray flames and their structural characteristics are strongly influenced by these interactions.

INTRODUCTION

Gravity plays an intrinsic role in determining the structure of gaseous jet diffusion flames [1-8]. At normal gravity, the diffusion flame at laminar and transitional speeds is subjected to the buoyancy-induced hydrodynamic instability, which is responsible for the presence of large vortical structures outside the flame surface. These low-frequency, slowly moving structures are known [5-8] to interact strongly with the flame surface, creating a wrinkled flickering flame. In addition, the shear-induced smaller structures from a Kelvin-Helmholtz instability develop inside the flame surface. The dynamics of these smaller structures may also be significantly influenced by the presence of buoyancy-induced outer structures. The

structural and transitional characteristics of normal-gravity (1 *g*) and microgravity (μg) diffusion flames also differ in other important aspects [4-7]. These include their global behavior, sooting characteristics, dependence on pressure and oxygen concentration, and transition to turbulence.

While the gaseous jet diffusion flames under 1-*g* and μg conditions have been investigated extensively, the corresponding research on spray diffusion flame has been rather limited [9-12]. Levy and Bulzan [9] report an experimental study of a laminar spray flame in a coaxial flow system with the inner nitrogen stream carrying liquid fuel droplets and fuel vapor in a coflowing air stream. The spray flame exhibits large-amplitude self-induced oscillations that are unique to the spray case (not observed for the gaseous fuel case) and believed to be due to a nonlinear coupling of two-phase flow dynamics and gravity effects. Li et al. [10] and Lucas et al. [11] employ a

* Corresponding author.

Presented at the Twenty-Fifth Symposium (International) on Combustion, Irvine, California, 31 July-5 August 1994.

Copyright © 1994 by The Combustion Institute
Published by Elsevier Science Inc.

counterflow spray burner to investigate experimentally and theoretically the structure of a laminar spray flame. Chen and Gomez [12] use an electrostatic spray generator in a counterflow spray burner and report an experimental study of a laminar spray flame. All of these investigations are performed under 1-g conditions. It may be argued that compared with a gaseous diffusion flame, the role of gravity in a spray flame is even more complex and scientifically more interesting to study. The additional complications arising from gravity are due to the effect of gravity on droplet motion, causing droplet settling and stratification in droplet concentration at low flow speeds, and the dynamic interactions of droplets with the outer buoyancy-driven structures. The influence of outer structures in dispersing the droplets and the effect of dispersed phase on the development of buoyancy-driven instability need to be understood in order to quantify the gravity-induced interactions between the phases and the effects of these interactions on the dynamics of spray flame. The understanding of these interactions is also relevant to the dynamics of fires in earth as well as space environments.

In this paper, we present time-dependent axisymmetric numerical simulation of an unsteady spray flame. The flame is formed between a droplet-laden nitrogen jet and a coflowing air stream. The major objective is to investigate the effect of gravity on the dynamics and structural characteristics of spray flames at laminar speeds. A time-dependent, multidimensional, two-phase algorithm is developed for the simulation. Following a brief description of the physical and numerical models, the computational results are reported for a *n*-heptane spray flame at 1 g and 0 g. The results although qualitative highlight the presence of large-scale buoyancy-generated structures outside the flame surface, the strong two-way interactions between droplets and large structures, and the influence these interactions have on the dynamics of spray flames at 1 g.

THE PHYSICAL MODEL

The spray flame simulated in the present study is shown schematically in Fig. 1. The flame is supported by a droplet-laden nitrogen jet issu-

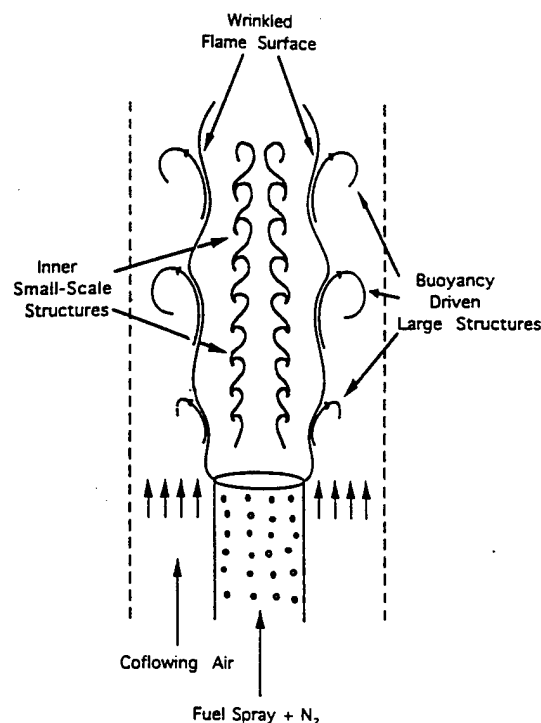


Fig. 1. A schematic of a spray diffusion flame at normal gravity.

ing into a coflowing oxidizer medium. At normal gravity, the structural characteristics of this spray flame are strongly influenced by gravity. First of all, the buoyancy-driven large-scale structures outside the flame surface interact with the flame surface, creating a wrinkled, flickering flame. The outer structures also modify the dispersion and vaporization behavior of droplets, which in turn modify the development of outer structures and their subsequent dynamic behavior. In addition, if the jet Reynolds number is in the transitional range, the small structures due to the Kelvin-Helmholtz instability develop inside the flame. In the present study, however, the jet Reynolds number is in the laminar range and the inner structures are not observed.

The spray flame dynamics is simulated by developing a detailed reacting two-phase flow algorithm. The solution of gas-phase properties is based on the time-dependent equations [8] for the species densities, axial and radial velocities, and enthalpy, written for an axisymmetric flow. The gas-phase model used includes multicomponent diffusion, variable

transport properties, and finite-rate chemistry. The gas-phase fluid consists of five species (nC_7H_{16} , O_2 , CO_2 , H_2O , and N_2). Nitrogen in the present model is assumed to be an inert species and is obtained from the global mass continuity. A single-step, global reaction mechanism is used to describe the combustion process. However, the activation energy is assumed to be small in order to simulate a "flame sheet" approximation. The effect of dispersed phase is incorporated through the source/sink terms, representing the exchange of mass, momentum, and energy between the gas and liquid phases. The liquid-phase equations are based on the Lagrangian formulation. Using the dilute-spray assumption, the spray is characterized by a discrete number of droplet groups, distinguished by their injection location, initial size, and time of injection. The governing equations are written for the dynamics and vaporization history of each droplet group. These include equations for the position and velocity vectors, and the instantaneous size of each group. A comprehensive vaporization model is employed to calculate the instantaneous droplet size and surface temperature along the trajectory of each group. The model includes the effects of variable thermophysical properties and nonunity Lewis number in the gas film outside the droplet, the effect of Stefan flow on the heat and mass transfer between the droplet and the gas, and the transient liquid heating. The variable thermophysical properties are calculated at reference film temperature and concentrations, obtained by using the 1/3 rule, except for the gas density which is calculated at the free stream value [13]. The Wilke rule [14] is used to calculate the dynamic viscosity and thermal conductivity of the gas film. The fuel (nC_7H_{16}) properties are collected from the various sources and approximated as a function of the temperature. The effect of transient liquid heating is incorporated by using the conduction-limit model [15]. This model is deemed satisfactory in the present study, since the maximum droplet Reynolds number during droplet lifetime is less than ten and thus the effect of internal circulation is expected to be negligible. For the same reason, the effects of gas-phase convection on the heat and mass trans-

port are represented by the Ranz-Marshall correlation [15]. It should be noted, however, that the two-phase algorithm developed is quite general and more refined models [13] such as the "effective conductivity" model for transient liquid heating and the "film theory" model for gas-phase convection can be easily implemented in the algorithm.

THE NUMERICAL MODEL

The numerical solution of the unsteady two-phase equations employs an implicit algorithm for solving the gas-phase equations, and an explicit Runge-Kutta procedure for the liquid-phase equations. The finite-difference forms of momentum equations are obtained using an implicit QUICKEST scheme [16] which is fourth-order in space and third-order accurate temporally, while those of species and energy equations are obtained using an hybrid scheme of Spalding [17]. A "finite control volume" approach with a staggered, non-uniform grid system is utilized. An iterative ADI (Alternating Direction Implicit) technique is used for solving the resulting sets of algebraic equations. A stable numerical integration procedure is achieved by coupling the species and energy equations through the source terms. At every time step, the pressure field is calculated by solving the pressure Poisson equations using the LU matrix decomposition technique. It should be noted that the pressure Poisson equations consider the effect of mass transfer from the liquid phase to the gas phase, represented by including a source term in the gas-phase mass continuity equation.

The liquid-phase equations are advanced in time by a second-order accurate Runge-Kutta method. Since the gas-phase solution employs an implicit procedure, the temporal step size used for integrating the liquid-phase equations is smaller than that for gas-phase equations. An automatic procedure is implemented in order to select an optimum liquid-phase time step. The procedure involves calculating the characteristic thermal response time, velocity response time, and vaporization time for each droplet group, and then selecting the temporal step size as a fraction (at least one-hundredth) of the smallest of these time scales. A detailed

examination of various time scales based on numerical experiments revealed that the temporal step size is determined by either the thermal response time or the velocity response time of a given droplet group. The number of subcycles for advancing the liquid-phase solution for each gas-phase cycle varies typically from two to ten, depending upon the droplet size.

The procedure to advance the two-phase solution over one gas-phase time step is as follows. Using the known gas-phase properties, the liquid-phase equations are solved over a specified number of liquid-phase subcycles. A third-order accurate Lagrangian polynomial method is used for interpolating the gas-phase properties from the nonuniform fixed grid to the instantaneous droplet location. The droplet location and other properties are updated after every liquid-phase subcycle. Also, during each subcycle, the liquid-phase source terms appearing in the gas-phase equations are calculated at the characteristic location, and then distributed to the surrounding gas-phase grid points. These source terms are then used in the implicit solution of the gas-phase equations. At each time-step, the four species conservation equations and the energy equation are first solved simultaneously to obtain the new density and temperature of the mixture. The momentum and mass continuity equations are then solved to complete the gas-phase calculations.

Flat initial profiles are used at the exit of the central fuel (or nitrogen) nozzle and the coannular air duct. The outflow boundaries are shifted sufficiently to minimize the propagation of any disturbance from the boundaries into the region of interest. The flow variables at the outflow boundary are obtained by using an interpolation procedure with weighted zero- and first-order terms. The weighting functions are selected by the trial-and-error approach, and the main criterion used is that the vortices crossing the outflow boundary should leave smoothly without being distorted.

RESULTS

The spray flame is established between a droplet-laden nitrogen jet and a coannular air flow.

The liquid fuel is *n*-heptane. Since the objective of this study is to investigate the behavior of laminar spray flame under the influence of gravity, a low-speed nitrogen jet at room temperature and at a velocity of 20 cm/s is considered for the base case. The jet Reynolds number based on the jet velocity and diameter is about 350. The computational domain is 15×80 cm and has 151×51 grid points. A nonuniform grid system, with a large number of grid lines clustered near the flame surface to resolve the steep gradients, is utilized. The minimum grid spacing is approximately 0.1 cm. The CFL number of 0.1 is used in all the spray flame simulations discussed in this paper. It should be noted that several diagnostic runs were first made to assess the grid-independence of gas-phase calculations, and the effects of temporal step size and droplet injection frequency. The details of these results, and of physical-numerical model are given in Ref. [18].

Figure 2 shows the instantaneous iso-temperature contours for the spray flames at 1 g and 0 g. The spray injection process is simulated by injecting monodisperse droplets into the jet shear layer. The number of droplets

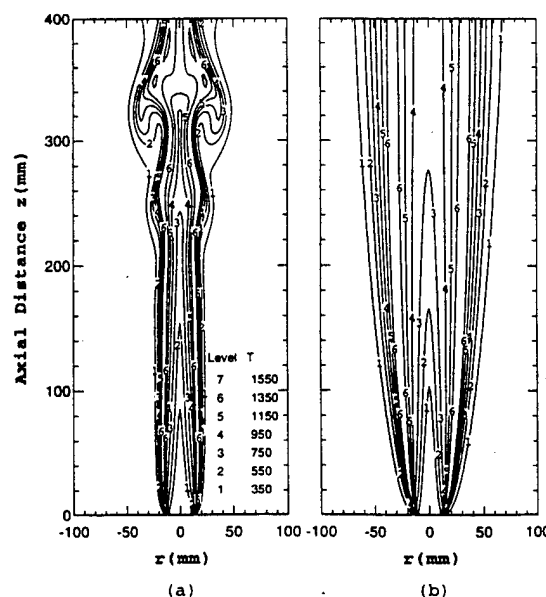


Fig. 2. Temperature contours for (a) normal-gravity and (b) zero-gravity spray flames. The droplet diameter is 200 μ m.

injected per unit time is determined from the overall liquid flow rate and the droplet diameter. For the results shown in Fig. 2, the droplet diameter is $200\text{ }\mu\text{m}$ and one droplet group with 50 droplets is injected every five gas-phase time steps. The outer toroidal vortices shown for the 1-g case appear as a part of the solution resulting from the buoyancy-driven instability; no artificial (external) excitation is needed to generate the outer structures. If the gravity is removed from the simulation, a steady laminar spray flame is obtained, as shown in Fig. 2b. It should also be noted that the smaller Kelvin-Helmholtz type vortices inside the flame, as discussed by Chen et al. [6], are not observed in the present simulations, since the jet Reynolds number is in the laminar range and no external perturbation is used to drive the jet instability. In this context, it is also important to note the differences between the shear-layer and buoyancy-induced instabilities. While the shear-layer instability is described as a convective instability, the buoyancy-induced instability is an absolute one [19].

The contours of fuel vapor mass fraction for the above two cases are portrayed in Fig. 3. The maximum fuel mass fraction occurs in the jet shear region, where the droplets are in-

jected. The flame is located outside the shear layer as fuel vapor diffuses radially outward, and mixes with the inwardly diffusing oxygen. As the mixing occurs, the chemical reaction occurs immediately due to the low activation energy used. The buoyant convection resulting from the heat release is believed to be responsible for the generation of large-scale outer structures.

The temporal evolution of toroidal vortices for $200\text{-}\mu\text{m}$ spray flame is shown in Fig. 4. Computed temperature data along the radial direction at two axial locations are recorded over a period of 600 ms, and the evolution is shown in the form of iso-temperature contours. The plots indicate a vortex-pairing interaction, which we believe is unique to the spray flame and has not been observed previously in gaseous diffusion flames at 1 g. The plot at $z = 30\text{ cm}$ shows a sequence of vortex pairs, with a smaller vortex following a larger one. By the time these vortices reach a height of 40 cm from the nozzle exit, the fast-moving smaller vortices are penetrating into the slowly moving larger ones causing a merging. The vortex frequency is found to be 14 Hz with a subharmonic of 7 Hz. When the droplet size was reduced to $100\text{ }\mu\text{m}$, outer vortices established (Fig. 6) at a location very close to the nozzle exit (closer than that of the gaseous flame) and vortex merging (not shown) took place at an height less than 20 cm.

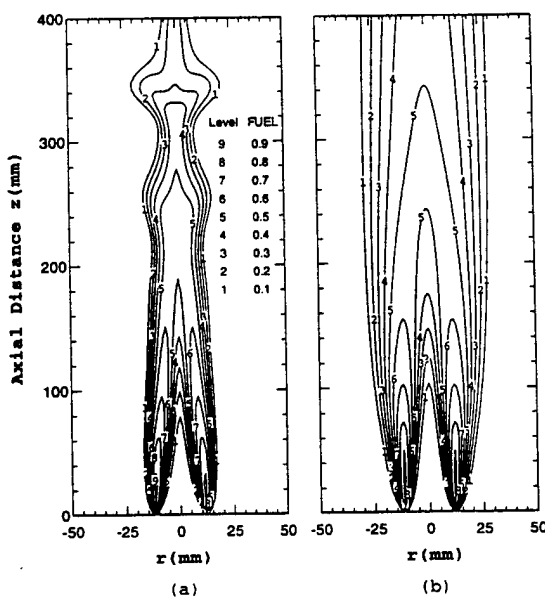


Fig. 3. Contours of fuel vapor mass fractions for (a) normal-gravity and (b) zero-gravity spray flames. The droplet diameter is $200\text{ }\mu\text{m}$.

Droplet-Vortex Interactions: Effects of Gravity and Droplet Size

In addition to the direct effect of gravity, the droplet trajectory and vaporization history may also be affected by the buoyancy-generated large structures. In order to examine these effects, the histories of droplet diameter, surface temperature, and droplet Reynolds number are plotted in Fig. 5 for 1-g and 0-g cases. One striking observation is that due to the buoyancy-generated convection, the droplet Reynolds number is much larger (maximum value ~ 9.0) for 1-g case compared with that (maximum value ~ 1.0) for 0-g case. In addition, Fig. 5 indicates that the droplet lifetime is shorter, although the surface temperature is mostly lower for 1-g case compared with that

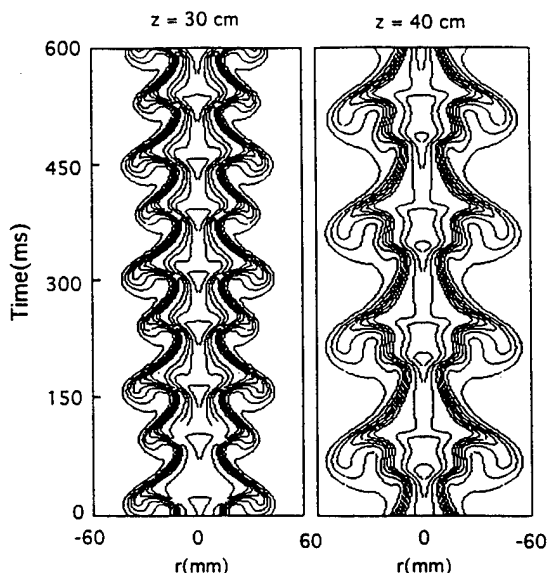


Fig. 4. Temporal evolution of buoyancy-generated outer structures at three axial locations for the spray flame (of Fig. 2) at 1 g.

for 0-g case. This is probably due to the relatively large droplet Reynolds number for 1-g case. The important conclusion seems to be that the droplet behavior in a 1-g laminar spray flame is strongly influenced by the large vortex structures. This effect is further highlighted in Fig. 5c, which shows the plot of droplet Reynolds number history for a 1-g spray flame with initial droplet diameter of 100 μm . The comparison of Reynolds number histories for the 100- and 200- μm cases shows that the vortex structures affect the motion of the 100- μm droplet more strongly than that of the 200- μm droplet. This has important implications for the two-way droplet-vortex interactions discussed next.

Effect of Droplet Size

Figure 6 shows the iso-temperature contours for three computed flames at 1 g, namely a *n*-heptane gaseous diffusion flame (Fig. 6a) and two spray diffusion flames (Figs. 6b and 6c) with initial droplet diameters of 100 and 200 μm , respectively. The corresponding flames computed at 0 g are shown in Fig. 7. The gaseous flame is calculated by assuming that the jet carries a mixture of N_2 and *n*-heptane

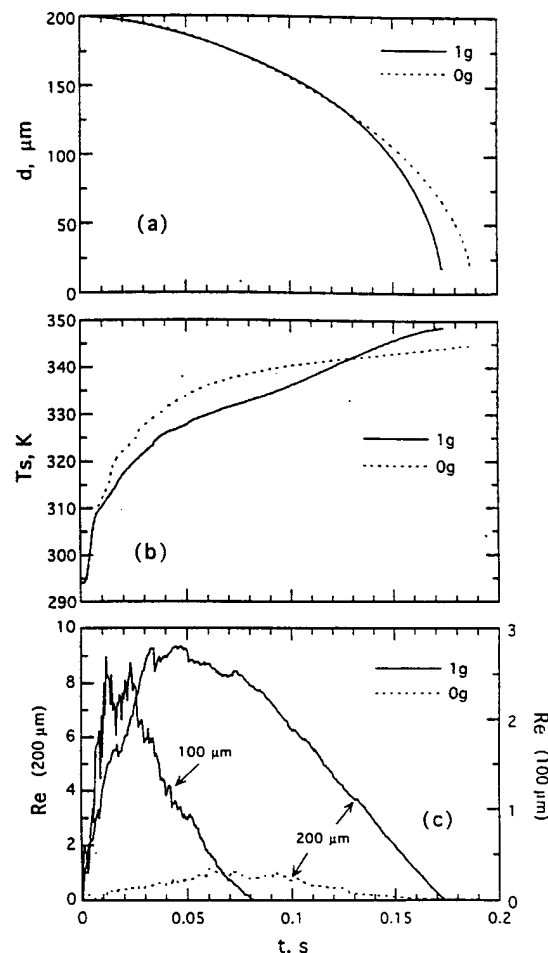


Fig. 5. Histories of (a) droplet diameter, (b) surface temperature, and (c) droplet Reynolds number for 200- and 100- μm spray flames at 1 g and 0 g.

in gaseous form, and may be approximated as a spray flame in the limit of initial droplet diameter going to zero. The important observation from these figures is that the initial droplet size has a strong influence on the structural characteristics of 1-g spray flames, but negligible effect on 0-g spray flames. For the latter, three flames (Fig. 7) appear to be qualitatively similar, although there are quantitative differences; the spray flame is generally thicker due to the distribution of droplets, but develops faster compared to the gaseous flame. Figure 6 clearly highlights the strong interaction between droplets and buoyancy-driven vortex structures, and the significant effect these interactions have on the dynamics of 1-g spray flames. Moreover, the droplet-vortex in-

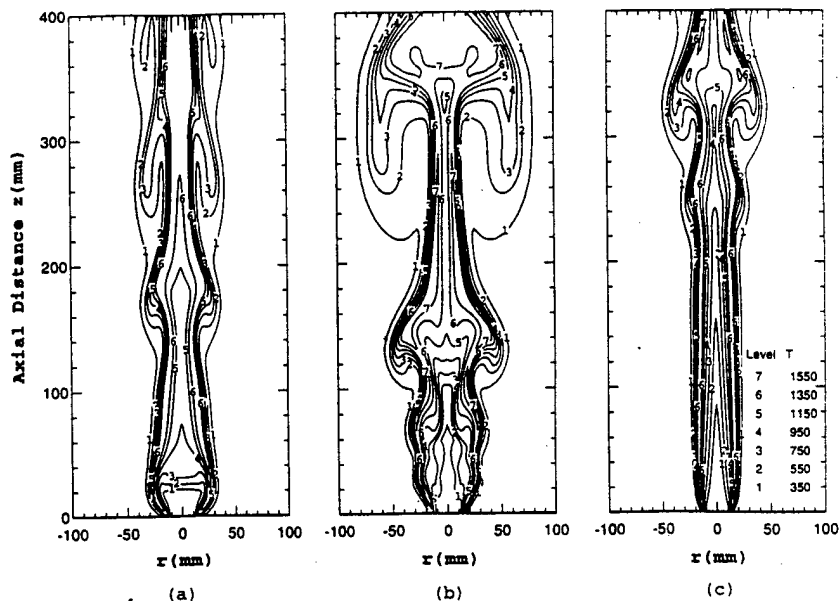


Fig. 6. Iso-temperature contours for three different flames at 1 g. (a) *n*-heptane gaseous diffusion flame (b) and (c) *n*-heptane spray diffusion flame with initial droplet diameter of 100 and 200 μm , respectively.

teraction is clearly a two-way interaction. The initial development of buoyancy-driven instability seems to depend upon the droplet size, which can be seen by comparing the initial appearance of vortex structures for the 100- and 200- μm cases in Fig. 6. The vortex struc-

tures, once they develop, influence the droplet dispersion and vaporization behavior, which in turn modifies the heat release process and thus the dynamics of vortex structures. Another important observation is that the effect of droplet size is not monotonic, i.e., there appears to be

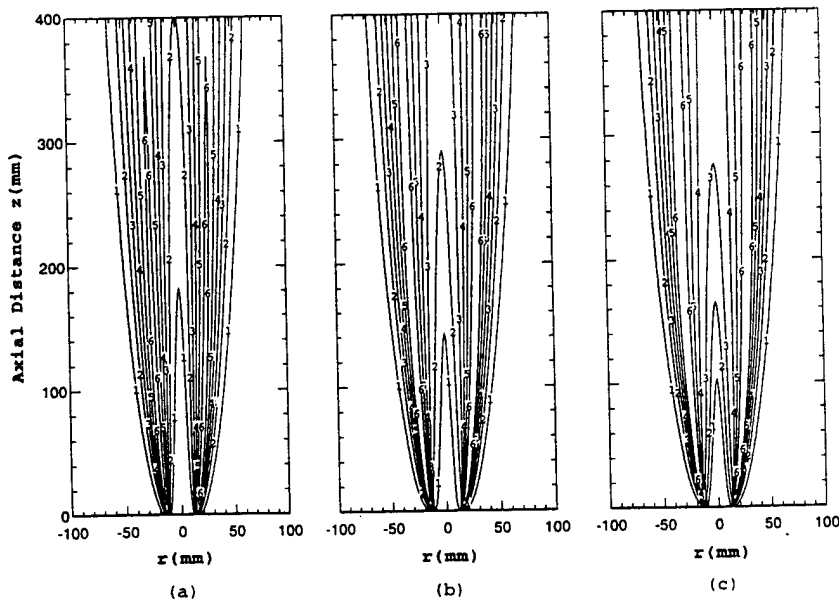


Fig. 7. Iso-temperature contours for three different flames at 0 g. For details see caption of Fig. 6.

an intermediate droplet size where the droplet-vortex interactions are the strongest. Whether this can be explained in terms of an intermediate Stokes number (ratio of droplet response time to time scale of large structures) remains to be investigated. For nonevaporating droplets in shear layers, it is found [20, 21] that the droplet dispersion in the presence of large vortical structures maximizes near Stokes number of unity. More detailed numerical experiments are needed to examine if a similar behavior exists in the presence of two-way droplet-vortex interactions.

CONCLUSIONS

A detailed multidimensional two-phase algorithm is developed to study the dynamics of laminar spray flames under the influence of gravity. The flame is formed between a droplet-laden nitrogen jet and a coflowing air stream. Results indicate that the dynamics of laminar spray flames is strongly influenced by gravity. While the computed spray flame at 0 g exhibits a steady laminar behavior, the simulations at 1 g show an oscillating flame, which is due to the presence of large-scale buoyancy-driven structures outside the flame surface. These large outer structures develop naturally as a part of the solution, without any external excitation. Results further indicate the occurrence of strong two-way interactions between large vortex structures and droplets. The relative intensity of two-way interactions appears to depend upon the initial droplet size. The dynamics and structural characteristics of laminar spray flames at 1 g are determined by these droplet-vortex interactions. Another effect of these interactions is the pairing of vortex structures, which we believe is unique to spray flames, and not observed previously for gaseous diffusion flames. It should be noted, however, that the results at this time can only be considered qualitative rather than quantitative.

This work was supported by AFOSR Grant F49620-92-J-0231, with Dr. Julian M. Tishkoff as the Program Manager. Many fruitful discussions with Dr. W. M. Roquemore at Wright-Patterson Air Force Base are greatly appreciated.

REFERENCES

1. Law, C. K., AIAA-90-0120, Twenty-Eighth Aerospace Sciences Meeting, Reno, January, 1990.
2. Bahadori, M. Y., Edleman, R. B., Stocker, D. P., and Olson, S. L., *ALAA J.* 28:236-244 (1990).
3. Ellzey, J. L., and Oran, E. S., *Twenty-Third Symposium (International) on Combustion*, The Combustion Institute, Pittsburgh, 1991, pp. 1635-1640.
4. Bahadori, M. Y., Hegde, U., Zou, L., and Stocker, D. P., Paper 93-0710, Thirty-First Aerospace Sciences Meeting and Exhibit, Reno, Nevada, January 11-14, 1993.
5. Davis, R. W., Moore, E. F., Roquemore, W. M., Chen, L. D., Vilimpoc, V., and Goss, L. P., *Combust. Flame* 83:263-270 (1991).
6. Chen, L.-D., Roquemore, W. M., Goss, L. P., and Vilimpoc, V., *Combust. Sci. Technol.* 77:41 (1991).
7. Katta, V. R., Goss, L. P., and Roquemore, W. M., AIAA Paper 93-0454, Thirty-First Aerospace Sciences Meeting and Exhibit, Reno, Nevada, January 11-14, 1993.
8. Katta, V. R., Goss, L. P., and Roquemore, W. M., *Combust. Flame* 96:60-74 (1994).
9. Levy, Y., and Bulzan, D. L., Proceedings of the Fifth International Conference on Liquid Atomization and Spray Systems, ILASS-91, Gaithersburg, MD, 1991.
10. Li, S. C., Libby, P. A., and Williams, F. A., *Twenty-Fourth Symposium (International) on Combustion*, The Combustion Institute, Pittsburgh, 1992, pp. 1503-1512.
11. Lacas, F., Darabiha, P., Versaev, P., Rolon, J. C., and Candel, S., *Twenty-Fourth Symposium (International) on Combustion*, The Combustion Institute, Pittsburgh, 1992, pp. 1523-1529.
12. Chen, G., and Gomez, A., *Twenty-Fourth Symposium (International) on Combustion*, The Combustion Institute, Pittsburgh, 1993, pp. 1531-1539.
13. Abramzon, B., and Sirignano, W. A., *Int. J. Heat Mass Trans.*, 32:1605-1618 (1989).
14. Edwards, D. K., Denny, V. E. and Mills, A. F., *Transfer Processes: An Introduction to Diffusion, Convection and Radiation*, 2nd ed., McGraw-Hill, New York, 1979.
15. Aggarwal, S. K., Tong, A. Y., and Sirignano, W. A., *ALAA J.* 22:1448-1457 (1984).
16. Leonard, B. P., *Comput. Methods Appl. Mech. Eng.* 19:59 (1979).
17. Spalding, D. B., *Int. J. Num. Meth. Eng.* 4:551-559 (1972).
18. Park, T. W., Aggarwal, S. K., and Katta, V. R., AIAA Paper 94-0684, Thirty-Second Aerospace Sciences Meeting and Exhibit, Reno, 1994.
19. Katta, V. R., Goss, L. P., and Roquemore, W. M., *ALAA J.* 32:84-94 (1994).
20. Crowe, C. T., Chung, J. N., and Trout, T. R., *Prog. Ener. Combust. Sci.* 14:171-194 (1988).
21. Aggarwal, S. K., *ALAA J.* 32:1322-1325 (1994).

Received 1 December 1993; revised 19 April 1994

Gravity Effects on the Dynamics of Evaporating Droplets in a Heated Jet

T. W. Park* and S. K. Aggarwal†

University of Illinois at Chicago, Chicago, Illinois 60607
and

V. R. Katta‡

System Research Laboratory, Inc., Dayton, Ohio 45440

Dispersion and vaporization behavior of liquid fuel droplets in a heated axisymmetric jet is studied using detailed flow visualization based on numerical simulations. Results show that the gravity has a strong effect on the dynamics of jet shear layer and droplets. The presence of gravity introduces the buoyancy-induced hydrodynamic instability, causing the large vortical structures to appear without any external perturbation. The droplet dispersion and vaporization behavior is influenced by both the vortex structures and the gravity. Three regimes, distinguished by the Stokes number St and the ratio of droplet terminal velocity to characteristic gas velocity V_r , are identified to characterize the effects of vortex structures and gravity on droplet dispersion. At low St and V_r , the droplets behave like gas particles. In the second regime, $0.1 < St < 0.64$ and $0.04 < V_r < 0.3$, due to the centrifugal action of the vortex structures the droplets are dispersed more than the gas particles. At the lower end of the third regime, the droplet motion is affected by both the vortex structures and the gravity, whereas at the higher end it is affected more by gravity. The effect of vaporization is to shift the Stokes number range for the three regimes.

Nomenclature

B = Spalding transfer number
 C_D = droplet drag coefficient
 C_p = specific heat
 D = vapor/air binary diffusion coefficient
 d_k = droplet diameter
 g = acceleration of gravity
 H = heat transferred from gas phase to droplet per unit mass of fuel vaporized
 \dot{H} = H/L
 h = heat transfer coefficient
 L = latent heat of vaporization
 Le = Lewis number, $\lambda/(\rho DC_p)$
 M = molecular weight
 \dot{m}_k = droplet vaporization rate
 \dot{m}_k'' = droplet vaporization flux rate, $\dot{m}_k/(\pi d_k^2)$
 \dot{m}_k^* = normalized droplet vaporization rate, $\dot{m}_k/(2\pi\rho D d_k)$
 Nu = Nusselt number
 P = pressure
 Pe = Peclet number, $RePr$
 Pr = Prandtl number
 R = universal gas constant
 Re = Reynolds number
 r = radial distance for gas-phase
 Sc = Schmidt number
 Sh = Sherwood number
 St = Stokes number, t_k/t_f
 T = temperature
 T_b = boiling temperature
 T_u = initial droplet temperature

t = time
 t_f = characteristic flow time
 t_k = droplet aerodynamic response time, $\rho_k d_k^2/(18\mu_k)$
 u = axial velocity
 V_r = droplet terminal velocity, $\rho_k d_k^2 g/(18\mu_k)$
 v = radial velocity
 x = axial location of droplet
 Y = mass fraction
 y = radial location of droplet
 z = axial distance
 α = thermal diffusivity
 λ = thermal conductivity
 μ = dynamic viscosity
 ρ = density

Subscripts

F = fuel vapor
 g = gas-phase
 i = i th species
 k = droplet characteristic or group
 l = liquid-phase
 s = surface
 ∞ = ambient condition

Introduction

GRAVITY influences combustion phenomena in many significant ways. Combustion systems where gravity plays a key role include burning droplets, jet diffusion flames, freely propagating premixed flames, candle flames, flames over solid and liquid pools, and other heterogeneous flames.¹ Since the pioneering work of Burke and Schumann² and Hottel and Hawthorne,³ the gaseous diffusion flames, because of their practical and scientific importance, have been extensively studied over many decades. More recently, opportunities provided by the microgravity (μg) environment at ground-based and space facilities have motivated additional research in this area, focusing on the effects of gravity on the diffusion flames.⁴⁻⁶ It has been found⁴⁻⁶ that the reduction of gravity introduces drastic changes in both the steady-state and the dynamic characteristics of these flames. Under μg conditions,

Received May 27, 1994; revision received Sept. 2, 1994; accepted for publication Sept. 16, 1994. Copyright © 1994 by the authors. Published by the American Institute of Aeronautics and Astronautics, Inc., with permission.

*Graduate Student, Department of Mechanical Engineering, Student Member AIAA.

†Associate Professor, Department of Mechanical Engineering, Associate Fellow AIAA.

‡Senior Engineer, Member AIAA.

the diffusion becomes a more dominant transport mechanism and the residence time is increased. Consequently, the μg diffusion flames are much taller, wider, sootier, and more radiating compared to the corresponding normal gravity (1g) flames. The μg and 1g flames also differ in structural details and their dependence on pressure, oxygen concentration, and Reynolds number. In addition, the 1g flames are subjected to the buoyancy-induced hydrodynamic instability, which is responsible for the presence of large vortical structures outside of the flame.⁷⁻⁹ These low-frequency, slowly moving outer structures interact strongly with the flame surface, creating a wrinkled flame, and are responsible for the flame flicker. In μg conditions, these structures are not present.

The transitional behavior of diffusion flames also exhibit fundamental differences in 1g and μg conditions.^{5,6} At 1g, transition is first observed at the flame tip, and with increasing Reynolds number, instability moves closer to the flame base. At μg , transition is associated with the appearance of intermittent disturbances that form at the base and move downstream. In addition, the buoyancy-generated turbulence aids in transition to turbulent flame at 1g, whereas the transition occurs over a much longer range of Reynolds number at μg . The blowoff limits are also significantly extended for μg diffusion flames.

While the gaseous diffusion flames under 1g and μg conditions have been extensively investigated, the research focusing on the effects of gravity on liquid-fuel spray diffusion flames is rather limited. Additional complications arising from gravity in a spray flame are due to the effect of gravity on droplet motion, causing droplet settling and stratification in droplet concentration, and the dynamic interactions of droplets with outer buoyancy-driven structures. These interactions, which involve the influence of outer structures on the dispersion and vaporization behavior of droplets, and the effect of dispersed phase on the development of buoyancy-driven instability, are expected to play an intrinsic role in the dynamics of spray flames.

In this article, the dynamics and dispersion behavior of *n*-heptane droplets in a heated axisymmetric jet is studied via numerical simulations. The gravity is considered a parameter. The overall objective is to study the fundamental processes of spray diffusion flames in laminar and transitional regimes under the influence of gravity. In this first study, the physical model is simplified by considering a heated jet issuing into a slower cold coflow, so that the complexities due to chemical reactions and the effects of dispersed phase on gas-phase processes can be avoided. The dispersion behavior of nonevaporating and evaporating droplets injected into the jet shear layer, where the fluid dynamics and heat transport processes are dominated by buoyancy-induced vortical structures, is investigated. Results presented focus on the effect of evaporation on the droplet dispersion behavior in the presence of large vortex structures, and the role of gravity in the dispersion process. Several experimental and computational studies¹⁰⁻¹⁸ have been reported in recent years, examining the dispersion behavior of particles or nonevaporating droplets in the presence of shear-induced vortex structures. These studies indicate that the dynamics of particles in the near shear-layer region is controlled by the large structures, which enhance the dispersion of intermediate size particles. The effect of vortex structures on particle dispersion is characterized by St , defined as the ratio of the particle response time to the characteristic flow time. The cited studies, however, do not consider the effect of evaporation on the dispersion behavior.

Physical Model

Figure 1 shows the physical system simulated in the present study. The heated air jet at a velocity of 1.0 m/s and temperature of 1200 K issuing into a coflow at velocity of 0.2 m/s and temperature of 294 K is considered. The jet diameter is 2.54 cm, and the computational domain in the radial di-

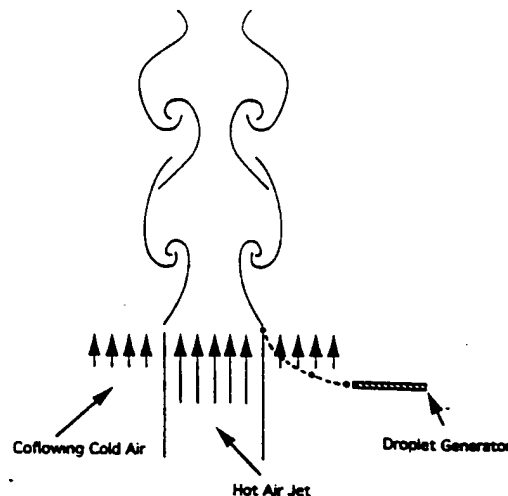


Fig. 1 Schematic of a buoyant hot air jet in a coflowing cold airstream at 1g.

rection is 15 cm. For the heated jet at 1g, the buoyancy-induced vortex structures are observed in the jet shear layer. The dynamics of these structures is simulated by solving the time-dependent, axisymmetric gas-phase equations. The *n*-heptane droplets of different diameters are then injected into the jet shear layer from the specified radial locations, and their dispersion and vaporization behavior is investigated by solving the appropriate droplet equations.

Gas-Phase Equations

The time-dependent governing equations written in cylindrical (z, r) coordinate system for an axisymmetric heated jet are

$$\begin{aligned} \frac{\partial(\rho\Phi)}{\partial t} + \frac{\partial(\rho u\Phi)}{\partial z} + \frac{\partial(\rho v\Phi)}{\partial r} &= \frac{\partial}{\partial z} \left(\Gamma^* \Phi \frac{\partial\Phi}{\partial r} \right) \\ &+ \frac{\partial}{\partial r} \left(\Gamma^* \Phi \frac{\partial\Phi}{\partial z} \right) - \frac{\rho v\Phi}{r} + \frac{\Gamma^* \Phi}{r} \frac{\partial\Phi}{\partial r} + S_r^* \end{aligned} \quad (1)$$

The general form of Eq. (1) represents the continuity, momentum, or energy equation, depending on the variable used for Φ . Table 1 gives the transport coefficients Γ^* and the source terms S_r^* that appear in the governing equations. In this table, μ , λ , and C_p are, respectively, the viscosity, thermal conductivity, and specific heat of air. They are considered functions of temperature.

Liquid-Phase Equations

The Lagrangian approach is employed to compute the properties of each droplet as it travels in a heated jet shear flow. The equations governing the variation of position, velocity, and size for a given droplet k along its trajectory are

$$\frac{dx_k}{dt} = u_k \quad (2)$$

$$\frac{dy_k}{dt} = v_k \quad (3)$$

$$\frac{du_k}{dt} = \frac{3C_p\rho_c}{4d_k\rho_k} |u_c - u_k| (u_c - u_k) + \left(\frac{\rho_c}{\rho_k} - 1 \right) g \quad (4)$$

$$\frac{dv_k}{dt} = \frac{3C_p\rho_c}{4d_k\rho_k} |v_c - v_k| (v_c - v_k) \quad (5)$$

$$\frac{dd_k}{dt} = -\frac{2\dot{m}_k''}{\rho_k} \quad (6)$$

Table 1 Transport coefficients and source terms appearing in governing equations

Equations	Φ	Γ^{Φ}	S_{Φ}^{Φ}
Continuity	1	0	0
Axial momentum	u	μ	$-\frac{\partial p}{\partial z} + (\rho_0 - \rho)g + \frac{\partial}{\partial z} \left(\mu \frac{\partial u}{\partial z} \right) + \frac{\partial}{\partial r} \left(\mu \frac{\partial v}{\partial z} \right) + \frac{\mu}{r} \frac{\partial v}{\partial z} - \frac{2}{3} \left[\frac{\partial}{\partial z} \left(\mu \frac{\partial u}{\partial z} \right) + \frac{\partial}{\partial z} \left(\mu \frac{\partial v}{\partial r} \right) + \frac{\partial}{\partial z} \left(\mu \frac{v}{r} \right) \right]$
Radial momentum	v	μ	$-\frac{\partial p}{\partial r} + \frac{\partial}{\partial z} \left(\mu \frac{\partial u}{\partial r} \right) + \frac{\partial}{\partial r} \left(\mu \frac{\partial v}{\partial r} \right) + \frac{\mu}{r} \frac{\partial v}{\partial r} - 2\mu \frac{v}{r^2} - \frac{2}{3} \left[\frac{\partial}{\partial r} \left(\mu \frac{\partial u}{\partial z} \right) + \frac{\partial}{\partial r} \left(\mu \frac{\partial v}{\partial r} \right) + \frac{\partial}{\partial r} \left(\mu \frac{v}{r} \right) \right]$
Energy	T	λ/C_p	0

where

$$C_D = \frac{24}{Re_k} \left(1 + \frac{Re_k^{2/3}}{6} \right) \quad (7)$$

$$Re_k = \frac{\rho_k [(u_k - u_\infty)^2 + (v_k - v_\infty)^2]^{1/2} d_k}{\mu_k} \quad (8)$$

The following expressions¹⁹ are used for heat and mass transfer rates to the drop:

$$\frac{hd_k}{\lambda} = \frac{2(N_p/Le)^{1/2}(1+B)}{(1+B)^{1/2} - 1} \quad (9)$$

$$\frac{\dot{m}_k d_k}{\rho D} = 2N_s^{1/2}(1+B) \quad (10)$$

and B is given by

$$B = (Y_{F_s} - Y_{F_\infty})/(1 - Y_{F_\infty}) \quad (11)$$

N_p and N_s are the corrective factors to consider the convective effect on heat and mass transfer, and are calculated using semi-empirical relations¹⁹:

$$N_p \text{ or } N_s = 1 + \frac{0.278 Re_k^{1/2} (Pr \text{ or } Sc)^{1/3}}{[1 + 1.232(Re_k(Pr \text{ or } Sc)^{4/3})^{1/2}]} \quad (12)$$

In order to complete the solution, the drop surface temperature and the fuel mass fraction at the drop surface must be known. The two equations required to solve for these quantities are provided by the fuel vapor pressure relationship and the energy equation in the liquid. The vapor pressure relationship has the form

$$Y_{F_s} = f(T_s, P, Y_\infty) \quad (13)$$

The transient heat transport within the droplet is represented by the unsteady heat diffusion equation in a spherically symmetric geometry. The solution of this equation involves a moving boundary-value problem as the droplet is evaporating. This problem can be reformulated by using a transformation to make the boundary stationary. The transformed governing equation²⁰ is

$$\frac{\partial \hat{T}_l}{\partial \hat{t}} = \frac{1}{\hat{r}^2} \frac{\partial}{\partial \hat{r}} \left(\hat{r}^2 \frac{\partial \hat{T}_l}{\partial \hat{r}} \right) - \frac{\hat{r} \dot{m}_k \lambda}{Le C_p \rho \alpha_l} \left(\frac{\partial \hat{T}_l}{\partial \hat{r}} \right) \quad (14)$$

with the initial and boundary conditions as

$$\hat{T}_l = 0 \quad \text{at} \quad \hat{t} = 0 \quad (15)$$

$$\frac{\partial \hat{T}_l}{\partial \hat{r}} = 0 \quad \text{at} \quad \hat{r} = 0 \quad (16)$$

$$\frac{\partial \hat{T}_l}{\partial \hat{r}} = \frac{\dot{m}_k (\hat{H} - 1) \lambda}{Le C_p \lambda_l (T_\infty - T_s)} \quad \text{at} \quad \hat{r} = 1 \quad (17)$$

where $\hat{T}_l(\hat{r}, \hat{t})$ and \hat{r} are, respectively, the normalized liquid temperature and radial location inside the droplet, and \hat{t} is the normalized time variable. These are given by

$$\hat{T}_l = (T_l - T_\infty)/(T_s - T_\infty) \quad (18)$$

$$\hat{r} = 2r/d_k \quad (19)$$

$$\hat{t} = \alpha_l \int_0^t \frac{4}{d_k^2} dt \quad (20)$$

The vapor pressure relationship and other properties used for the liquid and gas phases are summarized in the Appendix. The droplet model includes the effects of variable thermophysical properties and nonunity Lewis number in the gas film outside the droplet. The thermophysical properties are calculated at an average reference state defined as

$$\Phi_{avg} = \alpha \Phi_{gs} + (1 - \alpha) \Phi_g \quad (21)$$

where Φ is a generic quantity representing either mass fraction or temperature, and α is selected to be 0.7. The subscripts gs and g represent the gas-phase property at the droplet surface and outside the gas film, respectively.

It should be noted that in the present vaporization model, the effect of transient heating is incorporated by using the conduction-limit model.²⁰ This model is deemed satisfactory in the present study, since the maximum droplet Reynolds number during droplet lifetime is less than 10, and, therefore, the effect of internal circulation is expected to be negligible. For the same reason, the effect of gas-phase convection on the heat and mass transport is represented by semi-empirical correlations, Eq. (12).

Numerical Model

An implicit algorithm is employed to solve the unsteady gas-phase equations. The finite difference forms of the momentum equations are obtained using an implicit QUICKEST scheme.²¹ The governing equations are integrated on a non-uniform staggered-grid system. An iterative alternative direction implicit (ADI) technique is used for solving the resulting sets of algebraic equations. At every time step, the pressure field is calculated by solving the pressure Poisson equations simultaneously and utilizing the lower and upper diagonal (LU) matrix decomposition technique.

Figure 2 shows the grid system and the computational domain used in the present study. Grid lines are clustered near the shear layer to resolve the steep gradients of the dependent variables. Boundaries of the computational domain are shifted sufficiently to minimize the propagation of disturbances into region of interest. The flow variables at the outflow boundary are obtained using an extrapolation procedure with weighted zero and first-order terms. The main criterion used in selecting the weighting functions is that the vortices crossing this outflow boundary should leave smoothly without being distorted.

The liquid-phase equations are advanced in time by a second-order accurate Runge-Kutta method. Since the gas-phase

solution employs an implicit procedure. the temporal step size used for integrating the liquid-phase equations is usually smaller than that for gas-phase equations. An automatic procedure is implemented in order to select an optimum liquid-phase time step. The procedure involves calculating the characteristic thermal response time, velocity response time, and vaporization time for each droplet group, and then selecting the temporal step size as a fraction (two-hundredth) of the smallest of these time scales. A detailed examination of the various time scales, based on numerical experiments, revealed that the temporal step size is determined by either the thermal response time or the velocity response time of a given droplet group. The number of subcycles for advancing the liquid-phase solution for each gas-phase cycle typically varies from 1 to 30, depending upon the droplet size.

The procedure to advance the two-phase solution over one gas-phase time step Δt_g is as follows. Using the known gas-phase properties, the liquid-phase equations are solved over the specified number of liquid-phase subcycles. A third-order accurate Lagrangian polynomial method is used for interpolating the gas-phase properties from the nonuniform fixed grid to the droplet characteristic location. Figure 3 shows the gas-phase cells surrounding a droplet characteristic. The variable $\Phi_{g,k}$ represents the interpolated value of the gas-phase variable at the k -characteristic location. It should be noted that the interpolation scheme for the gas-phase velocities u and v

is based on their respective grid cells because of the use of a staggered grid in gas-phase calculation. It is also important to find the best-fit nine grid points at each characteristic location for better interpolation. The nine grid points shown in Fig. 3 correspond to the characteristic location in the shaded region. The droplet properties are updated after every liquid-phase subcycle. The gas-phase properties are then updated by solving Eq. (1), as described earlier.

Results and Discussion

For the base case, a jet at a velocity of 1.0 m/s and temperature of 1200 K issuing into a coflow at a velocity of 0.2 m/s and temperature of 294 K is considered. The computational domain is 15 cm in the radial direction and 40 cm in the axial direction. The jet diameter is 2.54 cm. A nonuniform grid system with 151×61 grid points, with a large number of grid points clustered in the shear layer, is utilized. The minimum grid spacing is about 0.079 cm, and the Courant, Friedrichs, and Lewy (CFL) number is 0.2. Several diagnostic runs were made to assure that the gas-phase simulations are reasonably independent of the grid size and CFL number. Results from one of these runs, indicating the grid-independence of the gas-phase solution, are given in Fig. 4, which shows the instantaneous iso-temperature contours for two grid densities for the heated jet at 1g. The effect of CFL number on the gas-phase solution was also evaluated, and the CFL number of 0.2 was found to be in the range where the solution is insensitive to the temporal step size Δt_g . The temporal step size for droplet calculation Δt_p was also taken in the range where the droplet results are independent of Δt_p , as described earlier.

Dynamics of Cold and Heated Jets

The stability characteristics of cold and heated jets under 0 and 1g conditions are examined first without injecting droplets into the jet shear layer. Based on the jet velocity of 1.0 m/s and the diameter of 2.54 cm, the cold and heated jets represent flows with Reynolds number of 1.546×10^3 and 1.50×10^3 , respectively. The latter is calculated using the density and viscosity of air at 1200 K. Due to the velocity gradient, the jet shear layer exhibits Kelvin-Helmholtz-type instability, which is characterized by the formation of large toroidal vortices. However, to simulate these vortices a low-amplitude perturbation, either external or inherent in the calculations, is required. Numerical experiments were per-

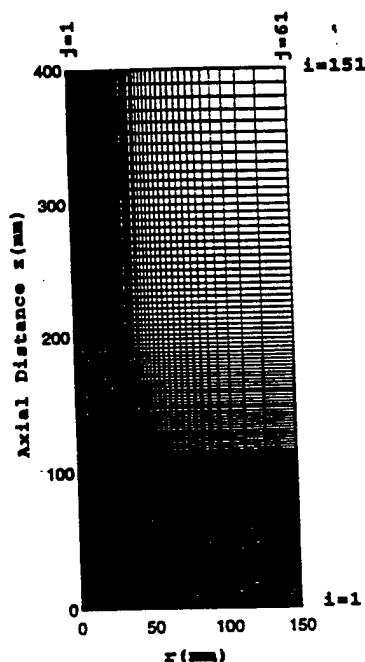


Fig. 2 Typical grid system used for simulations.

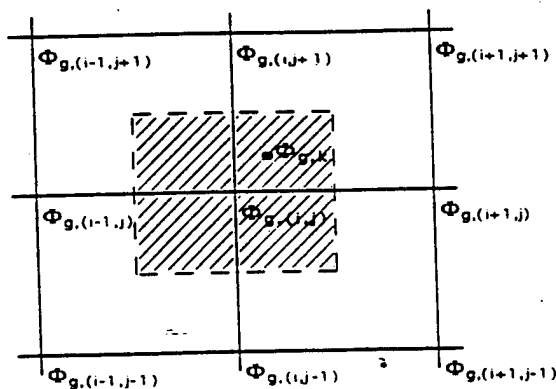


Fig. 3 Best-fit grid cells for the interpolation.

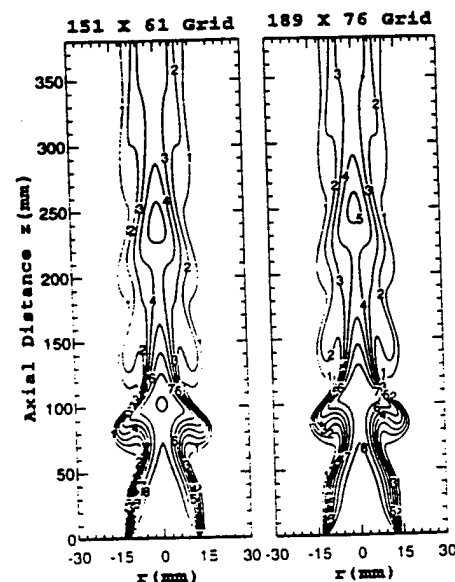


Fig. 4 Comparison of temperature contours for the heated jet with two grid densities.

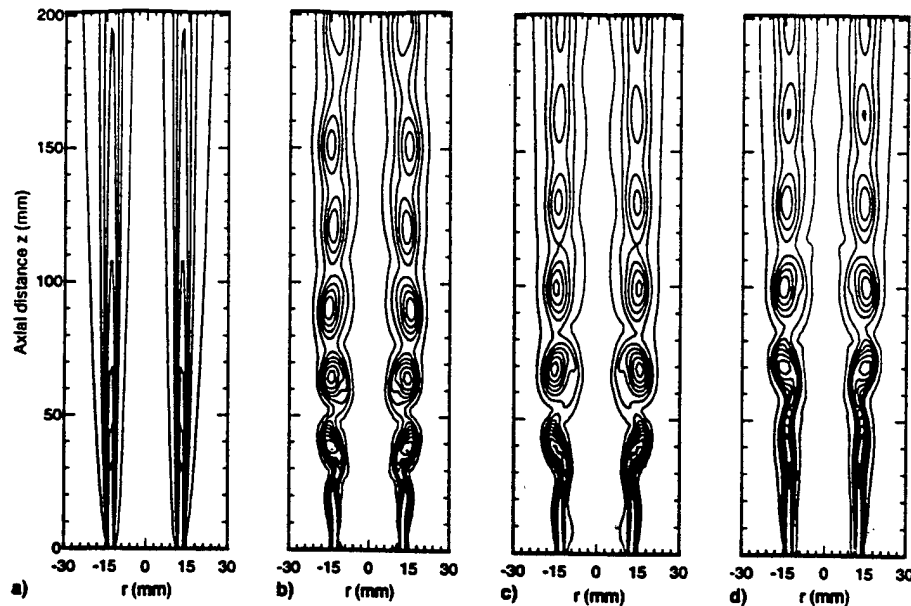


Fig. 5 Iso-vorticity contours for the cold jet for four different cases: a) without external forcing, b) white-noise forcing, c) forcing the central high-speed jet at a frequency of 20 Hz, and d) forcing the low-speed annulus flow at a frequency of 20 Hz. Jet Reynolds number is 1.546×10^3 .

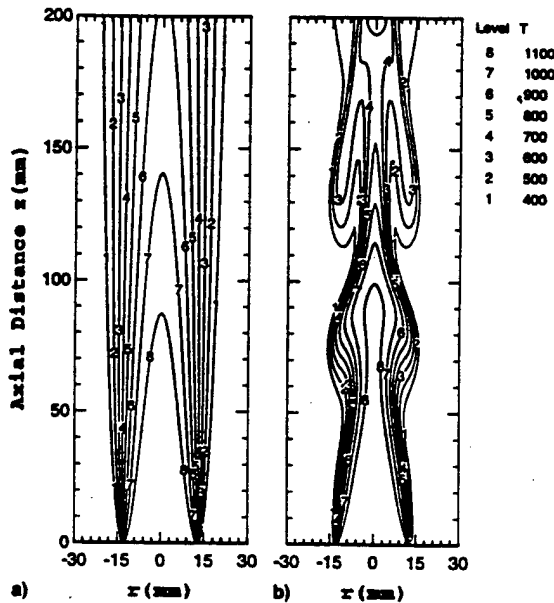


Fig. 6 Iso-temperature contours for the hot jet at a) 0 and b) 1g.

formed on these jets for triggering the shear-layer instability and the results are summarized in Figs. 5 and 6.

To determine whether the noise inherent in the calculations is sufficient or not for the development of the shear-layer instabilities, both the cold and heated jets are simulated without introducing any external perturbation. Cold-jet calculations performed with different grid systems and time steps have converged to a steady-state solution that is given in Fig. 5a. The iso-vorticity contours of this figure show that the shear layer is laminar without having flow instabilities. These calculations suggest that the noise in the present simulations is not sufficient for the manifestation and growth of the shear-layer instabilities. Therefore, as an alternative, attempts were made to make the calculated jet shear layer unsteady by providing it with external perturbations.

The following types of external perturbations are considered in the present study: 1) computer-generated white noise superimposed on the convective flow at all the grid points within a circular region of two-grid radius and centered in the jet shear layer at $z = 8$ mm. 2) forcing the entire central high-

speed jet to oscillate at a frequency of 20 Hz, and 3) forcing the low-speed annulus flow to oscillate at 20 Hz. Instantaneous vorticity fields resulting from the calculations using the above three types of perturbations are depicted in Figs. 5b–5d, respectively. The magnitude of forcing (velocity fluctuation) for different perturbation modes was fixed at 3% of the local axial velocity. Forcing frequency (20 Hz) used for the latter two modes was equal to the peak-amplification frequency noted from the calculations made with white-noise perturbations (obtained from the fast Fourier transformation of the time data). The iso-vorticity contours of Figs. 5b–5d indicate that all the three types of external perturbation are magnified similarly and resulted in toroidal vortices of same size. Due to the lower-magnitude velocity fluctuations used in the last case (3% of the annulus air velocity of 0.2 m/s) the instability is somewhat weaker (Fig. 5b) in the region $z < 80$ mm compared to that seen for the other two cases (Fig. 5c and 5d).

It is clearly evident from Fig. 5 that the shear layer of the cold jet ($Re = 1.546 \times 10^3$) becomes unsteady only in the presence of external perturbations, and the flow structure seems to be insensitive to the type of perturbation used. For the corresponding heated jet case (jet velocities the same as those of the cold-flow case) the shear layer might be expected to be stable as the effective Reynolds number based on air density and viscosity at 1200 K is reduced by a factor of about 10. Because of the presence of density variation in the heated-jet case, simulations are made by 1) neglecting the gravitational force and 2) assuming that gravity acts in a direction opposite to that of the jet flow, which represents the vertically mounted jets. Computed jets for both the cases are shown in Fig. 6 using iso-temperature contours.

Calculations made by neglecting gravitational force yielded a solution that has no vortical structures in the shear layer (Fig. 6a). Kelvin-Helmholtz instabilities did not develop even when the shear layer was excited using the previously described perturbation methods. However, when the gravity term was introduced in the axial momentum equation, large-scale vortex structures appeared due to the buoyancy-induced instability of the heated-jet shear layer (Fig. 6b). It is important to note that these structures are produced without using any external forcing, and their dynamics are found to be unaltered by the superimposition of the three different external perturbations discussed earlier. This is in contrast to the dynamics of shear-induced vortex structures. The buoyant

acceleration of hot gases at 1g helps the formation of large vortex structures, while at 0g, due to the low Reynolds number, the jet shear layer exhibits a behavior typical of a laminar flow. The temporal evolution of buoyancy-induced vortices for the 1g case is shown in Fig. 7. Computed temperature data along the radial direction at two axial locations are recorded over a period of 250 ms, and the evolution is shown in the form of iso-temperature contours. It can be seen that the vortex structures are highly coherent and periodic. The frequency of oscillation is 15.8 Hz. Even though the frequencies of the Kelvin-Helmholtz instability of the cold jet and the buoyancy-induced instability of the heated jet are not much different (20 and 15.8 Hz, respectively), the sizes of the vortical structures in these two cases (Figs. 5b and 6b) are significantly different. The number of vortical structures present within an axial distance of 200 mm in the cold and heated jets are about 6 and 2, respectively. Based on the average vortex size and the crossing frequency, the average convective velocities for the cold and heated jets must be approximately 0.6 and 1.5 m/s, respectively. The higher convective velocity in the case of heated jet is the result of buoyancy.

Effect of Gravity on Droplet Motion

The motion and dispersion characteristics of droplets in the dynamically evolving flow of heated jet (Fig. 6b) are studied by injecting droplets of varying size into the shear layer. Figure 8 shows the effect of gravity on the trajectories of evaporating droplets that are injected at the nozzle rim and traverse the unsteady flowfield dominated by large-scale vortical structures. For this case, the gas-phase simulation is started at $t = 0$ and the droplets are injected at $t = 0.954$ s. During the period of $0 < t < 0.954$ s, the initial flow transient is convected out of the computational domain. The trajectories shown in Fig. 8 are computed from $t = 0.954$ –2.226 s by solving the gas-phase and the droplet equations simultaneously. For all the cases considered, the initial droplet velocity is assumed to be equal to the jet velocity. For the 0g case (Fig. 8b), due to the absence of buoyant vortex structures, the jet flow has little influence on the droplet trajectory. In particular, there is virtually no radial dispersion of droplets, and the initial droplet size does not have much effect on the trajectory. For the corresponding 1g case, however, the droplet motion is strongly influenced by the buoyancy-induced vortex structures. In addition, it may also be affected by grav-

ity directly, depending upon the initial droplet size. In fact, we can identify three different droplet-size regimes given in Table 2, that are distinguished by the Stokes number and the ratio of droplet terminal velocity [$V_t = \rho_d d_i^2 g / (18 \mu g)$] to characteristic gas velocity. Here, the Stokes number is defined by the ratio of t_k to t_p , the latter defined by the time scale of large structures. At low Stokes number (initial diameter $d_i < 50 \mu\text{m}$), the droplets behave like gas particles, and gravity has no direct influence on their motion as their terminal velocity is small compared to the characteristic gas velocity ($V_{\text{gas}} = 1.5$ m/s), the latter being taken as the average convective velocity of the buoyancy-induced structures. In the second regime, the Stokes number in the range $0.1 < St < 0.64$, the droplet terminal velocity is still small relative to V_{gas} . In this regime, due to the centrifugal action of the vortex structures,^{10,16,17} the droplets are dispersed more than the gas particles. This will be discussed quantitatively in the next section. The third regime is characterized by intermediate to large values of the Stokes number. At the lower end of this regime, the droplet motion is affected by both the vortex structures and the gravity, whereas at the higher end, it is affected more strongly by gravity. For example, as shown in Fig. 8, the 500- μm evaporating droplets fall back to the inner jet region due to the strong effect of gravity.

Table 2 Stokes numbers and droplet terminal velocities for various droplet diameters

$d_i, \mu\text{m}$	St	$V_t, \text{m/s}$
25	0.01	0.006
50	0.04	0.025
100	0.16	0.10
150	0.36	0.23
200	0.64	0.40
250	1.00	0.63
300	1.44	0.90
500	4.00	2.52

Characteristic flow time used in the calculation of Stokes numbers is 0.063 s based on a vortex frequency of 15.8 Hz.

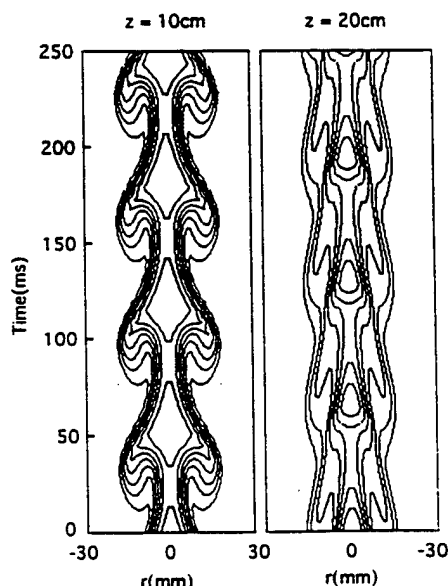


Fig. 7 Temporal evolution of buoyancy-generated vortex structures in terms of iso-temperature contours at two axial locations for the 1g case of Fig. 6.

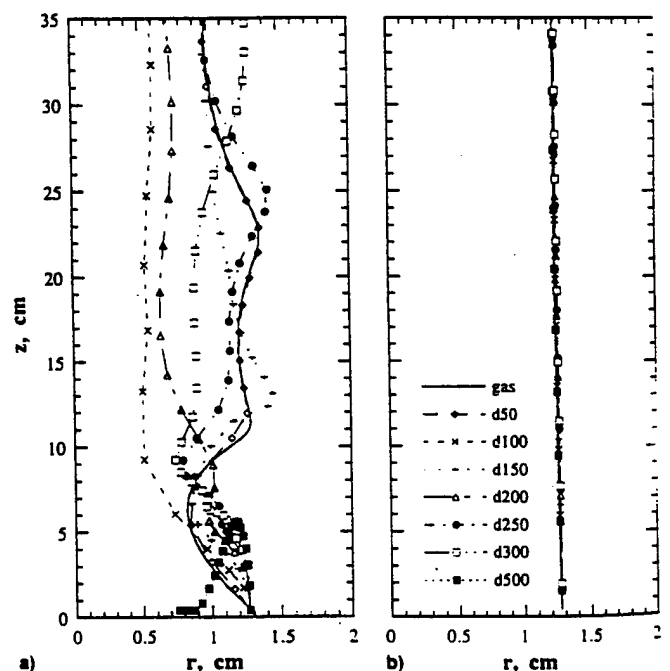


Fig. 8 Trajectories of evaporating droplets injected into the hot jet shear layer under a) 1 and b) 0g conditions. Results are shown for a gas particle and droplets of different initial diameters, with d50 representing diameter of 50 μm , etc.

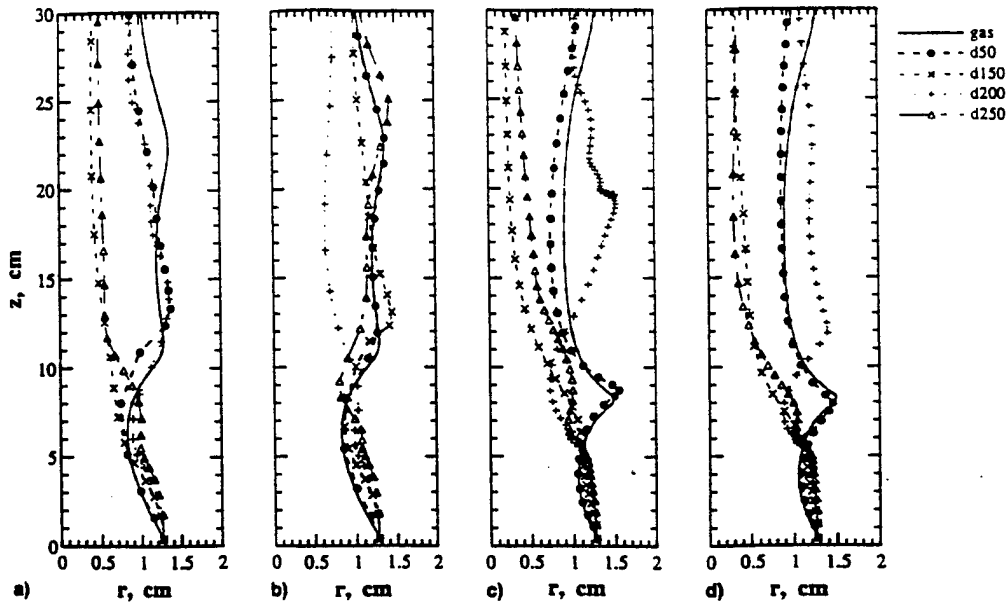


Fig. 9 Trajectories of nonevaporating (a and c) and evaporating (b and d) droplets injected at two different injection times for the 1g case. Droplets in a) and b) are injected at $t = 0.954$ s and those in c) and d) at $t = 0.986$ s.

The effect of evaporation on droplet trajectories for the 1g case is portrayed in Fig. 9, which shows the trajectories of nonevaporating and evaporating droplets injected at two different times. The difference in the two injection times (t_{diff}) is one-half the time period of the dominant instability frequency, i.e., the droplets in Figs. 9a and 9b are injected at time $t = t_{inj}$, while those in Figs. 9c and 9d are injected at $t = t_{inj} + t_{diff}$. Important observations from this figure are as follows:

1) In the low Stokes number range, the trajectories of evaporating droplets are qualitatively similar to those of nonevaporating droplets, except that the Stokes number decreases along the trajectory for the evaporating case. As a consequence, the evaporating droplets follow the gas motion more closely than the corresponding nonevaporating droplets (see Figs. 9a and 9b).

2) In the intermediate Stokes number range ($0.36 < St < 1.4$), due to the combined effect of vaporization and large structures in a dynamically evolving flowfield, the trajectories of evaporating and nonevaporating droplets are significantly different. For example, compare the trajectories of 200- μ m nonevaporating and evaporating droplets in Figs. 9a and 9b, respectively.

3) The droplet trajectory exhibits strong sensitivity to the time (during the dominant instability period) as to when the droplet is introduced into the shear layer. This can be seen by comparing the trajectories of same-size droplets in Figs. 9a and 9c. This sensitivity is important, however, only over the time scale of the dominant frequency. For example, in the dispersion analysis that involves a time scale much longer than the instability time scale, this sensitivity would not be important.

4) The trajectory of a 200- μ m droplet is distinctly different from those of 150- and 250- μ m droplets. This has some important implication in the size-dependence of the dispersion function discussed in the next section.

Dispersion Behavior

In order to quantify the effects of vortex structures and gravity on droplet dispersion, the dispersion function is defined as

$$D(t, N) = \left(\left\{ \sum_{i=1}^N [r_i(t) - r_{inj}]^2 \right\} / N \right)^{1/2} \quad (22)$$

where N is the total number of droplets in the flowfield at time t , r_i the radial location of droplet i at time t , and r_{inj} the radial injection location of the same droplet at nozzle exit. It can be expected that the dispersion function is a strong function of t and droplet diameter d_p . In addition, it may be a function of r_{inj} , N , and starting time of injection t_0 . In the results presented here, the dispersion function was made statistically independent of N by using a sufficiently large number of droplets in the dispersion calculation, and of t_0 by performing calculations over a sufficiently large time t . It is also worth noting that the above dispersion function does not distinguish between the droplets that move away from the jet axis and those that move toward it.

Dispersion behavior of droplets in the heated-jet flow is investigated by continuously injecting single-sized droplets from a given location. Results of the calculations made with a large number of droplet injections are shown in Fig. 10 in the form of simultaneous snapshots (or instantaneous images) of the flow and droplets. Iso-temperature contours are plotted using broken lines and the droplet locations are marked with solid circles. Snapshots for different size droplets are depicted in this figure, whereas in each individual snapshot locations of the evaporating and nonevaporating droplets are plotted on the left and right sides of the symmetric jet, respectively. Color (represents the size) of the droplet changes from red to blue as it evaporates from the initial size (at the instant of injection) to the size of a gas particle, which is taken as 10 μ m or one-tenth of the initial size, whichever is smaller. Since the droplets on the right side of the jet represent nonevaporating ones, the color of the droplets remains red. As expected, the snapshot of 50- μ m-evaporating droplets shows that these droplets behave like tracer particles and follow the iso-temperature contours. In general, due to the higher momentum, the nonevaporating droplets deviate more from the iso-temperature contours compared to the evaporating ones.

Dispersion of evaporating and nonevaporating droplets in a dynamically evolving flow are quite different. The instantaneous flowfield shown in Fig. 10 has two large-scale vortices that are located approximately at $z = 70$ and 140 mm. The first vortex ($z = 70$ mm) is pulling the smaller size droplets (both the evaporating and nonevaporating ones) radially outward and has little impact on the droplets that are larger than 150 μ m. On the other hand, the medium-sized (~ 150 μ m) nonevaporating and smaller evaporating droplets are impacted more by the second vortex ($z = 140$ mm). It may also

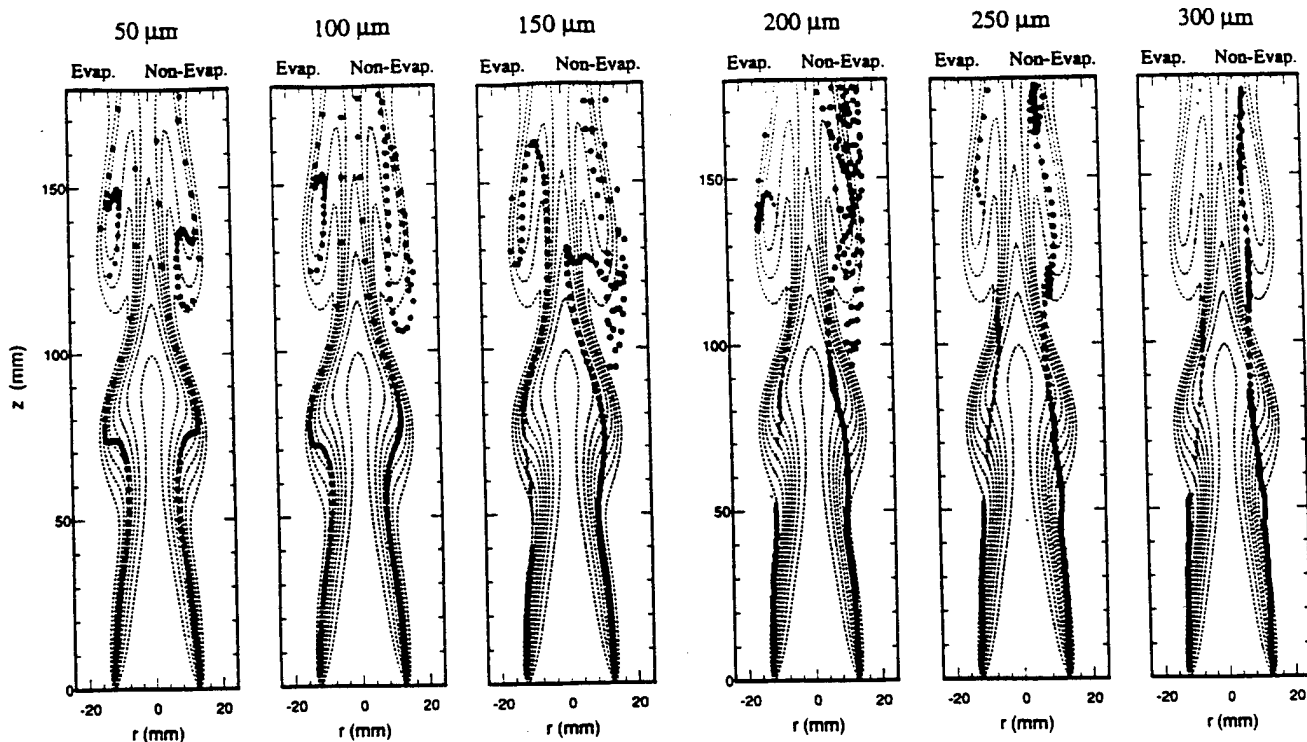


Fig. 10 Simultaneous snapshots of the flow (iso-temperature contours) and droplets (solid circles) of different initial sizes: in each individual snapshot locations of the evaporating and nonevaporating droplets are plotted on the left and right sides of the symmetric jet, respectively.

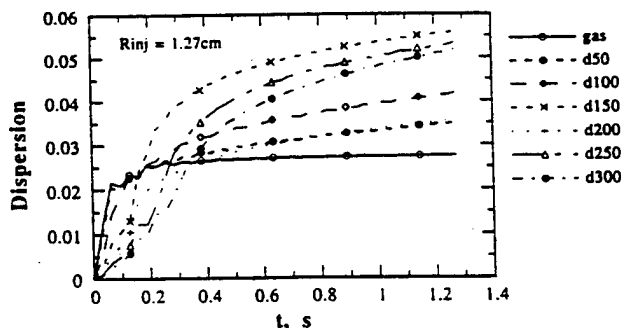


Fig. 11 Variation of dispersion function with time for evaporating droplets at 1g.

be noted from Fig. 10 that in the neighborhood of the second vortex the evaporating droplets are not dispersed as much as the nonevaporating ones. The reason for this difference may be explained as follows:

The flowfield and the droplet locations near the second vortex are, in fact, the evolution of the respective ones associated with the first vortex. It is known that the entrainment of droplets into the first vortex decreases with the size of the droplet with a maximum occurring for the gas-like particles. On the other hand, as the vortex evolves in space and time, the entrained droplets are centrifuged out of the vortex due to their inertia, which increases with the droplet size. As a result, dispersion of nonevaporating droplets in the neighborhood of the second vortex is more for the medium-sized droplets ($\sim 150 \mu\text{m}$). However, evaporating droplets exhibit a different behavior. Due to the evaporation process that occurs during the evolution of the flowfield in time and space, the smaller- and medium-sized droplets are not centrifuged out of the second vortex. On the other hand, the larger-sized droplets are not entrained by the first vortex, and hence, are not dispersed in the neighborhood of the second vortex.

Figure 11 shows the variation of dispersion function with time for the gas particle and evaporating droplets for different

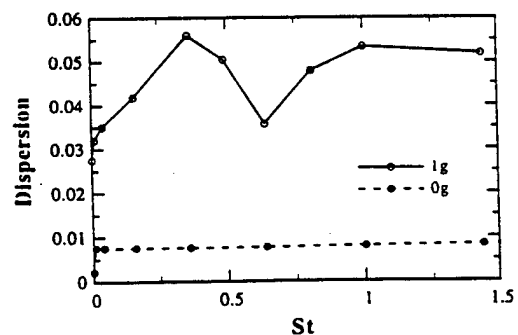


Fig. 12 Variation of dispersion function with Stokes number for the evaporating case at 1 and 0g.

initial diameter for the 1g case. The dispersion function generally increases with time as the droplets, that are continuously being injected into the shear layer, are either pulled radially inward by the heated jet or dispersed radially outward by the large structures. After $t = 0.8 \text{ s}$, the dispersion function starts leveling out, since some of the injected droplets are being convected out of the computational domain. In order to examine the effect of initial droplet size, it is convenient to plot dispersion function vs size at a fixed t . Figure 12 shows this plot for the 1 and 0g cases, where the dispersion function at $t = 1.27 \text{ ms}$ is plotted vs the Stokes number. Three observations can be made from this figure. First, as expected and consistent with the results in Fig. 8, the droplet dispersion for the 0g case is negligible compared to that for the 1g case. Second, the effect of large vortex structures is to enhance the dispersion of intermediate size droplets. Third, there is a range of Stokes number near $St \sim O(1)$, where the droplet dispersion behavior is modified by the direct effect of gravity. For example, the maximization of dispersion function for the intermediate Stokes numbers, which is typically observed in the shear-induced vortical structures,^{16,17} is modified by gravity. As indicated in Fig. 12, there is a drop in the dispersion

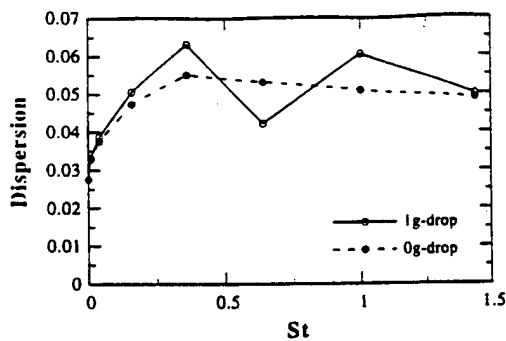


Fig. 13 Variation of dispersion function with Stokes number for nonevaporating droplets with and without the effect of gravity on droplet motion.

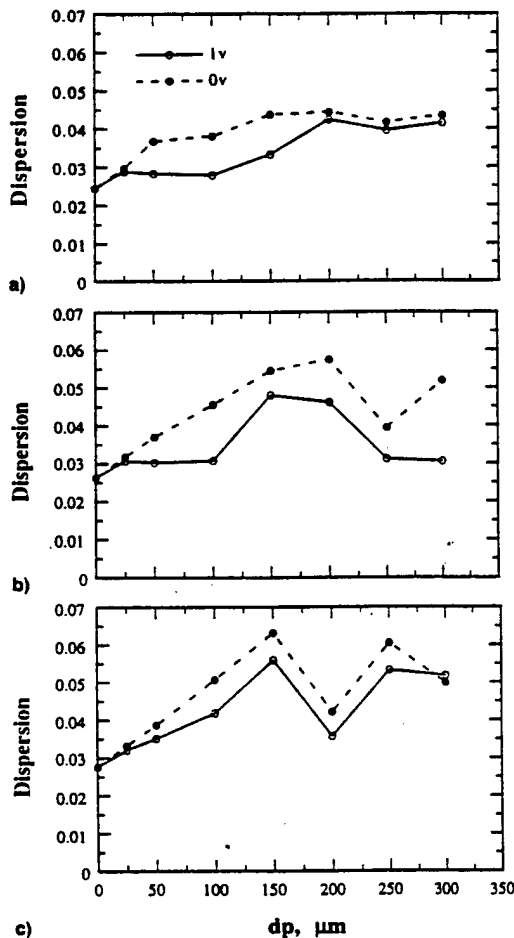


Fig. 14 Variation of dispersion function with initial droplet size for three different injection locations: r_{inj} = a) 1.10, b) 1.20, and c) 1.27 cm. 1v and 0v represent evaporating and nonevaporating cases, respectively.

function near $St = 0.64$ ($d_p = 200 \mu m$), which is believed to be due to the fact that the effect of gravity on droplet motion becomes comparable to that of large-scale structures. This is confirmed by performing a dispersion calculation without the effect of gravity on droplet motion. The result given in Fig. 13 for the nonevaporating case indicates that the dispersion function does not experience a drop near $St = 0.64$ ($d_p = 200 \mu m$), when the gravity term is excluded from the droplet equations. Rather, an optimum droplet size is seen to exist, where the dispersion is maximized. This is consistent with the results of previous experimental^{15,16} and computational^{10,17}

Figure 14 shows the effect of injection location on droplet dispersion for evaporating and nonevaporating droplets at 1g. The dispersion function is plotted vs initial droplet size for three injection locations. The important observation is that the maximum droplet dispersion is achieved by injecting droplets in the jet shear layer ($r_{inj} = 1.27$ cm), and that the evaporating droplets are dispersed less compared to the nonevaporating droplets. It is also important to note that as the injection location is moved to the jet core, the dispersion function does not show a sudden drop near $d_p = 200 \mu m$. This is related to the fact that the direct effect of gravity is not as strong in the jet core region as it is in the shear layer region.

Conclusions

Dynamics and dispersions of *n*-heptane liquid fuel droplets in a heated jet are studied via numerical simulations and flow visualization. The objective of this study is to investigate the droplet dynamics and vaporization behavior in a heated shear layer under normal-gravity and zero-gravity environments. An implicit, third-order accurate upwind numerical scheme is used to solve the unsteady gas-phase equations. The Lagrangian approach is employed to study the droplet dynamics and dispersion in a heated shear layer.

Results show that the gravity has a strong effect on the dynamics of the heated jet shear layer, as well as on the dispersion and vaporization behavior of droplets. The presence of gravity introduces the buoyancy-induced hydrodynamic instability, causing the large vortical structures to appear without any external perturbation. The dynamics of the buoyancy-induced instability in a hot jet is compared to that of the Kelvin-Helmholtz instability in a cold jet. While the large-scale structures in both these cases are highly coherent and periodic with the respective frequencies of 15.8 and 20 Hz, their sizes and convective velocities are significantly different.

The droplets trajectory plots and the simultaneous snapshots of the flow and droplets are employed to analyze the dynamics of nonevaporating and evaporating droplets under the influence of buoyancy-induced vortex structures and gravity. Three different droplet-size regimes are identified to characterize the effects of large structures and gravity. These regimes are characterized by the values of St and Vr . In the first regime, characterized by small values of St and Vr , the droplet behavior is akin to that of gas particles. In the second regime, the droplet dispersion and vaporization behavior is strongly influenced by large vortical structures and gravity, whereas in the third regime, the droplet motion is more strongly affected by the direct effect of gravity.

In order to quantify the effect of gravity and large vortex structures on droplet dynamics, the dispersion function is calculated as a function of initial droplet size for evaporating and nonevaporating droplets for 1 and 0g conditions. The important observations are as follows:

- 1) At zero gravity, in the absence of buoyancy-induced vortex structures, the droplet dispersion is negligibly small compared to that at normal gravity.
- 2) The effect of large buoyant structures is to enhance the dispersion of intermediate size droplets, and can be represented in terms of the Stokes number.
- 3) There is a range of Stokes number near unity, where the correlation between dispersion function and Stokes number, reported previously for particle-laden shear flows,^{10,17} is modified by the direct effect of gravity.
- 4) The dispersion behavior of nonevaporating droplets is quite different from that of evaporating droplets. Due to the centrifugal action of the vortical structures, the intermediate-sized nonevaporating droplets disperse more than the gas particles. However, due to the evaporation process, the intermediate-sized evaporating droplets are not centrifuged out of the vortical structures and consequently disperse less than the nonevaporating droplets.

Appendix: Mixture and Fuel Properties

The viscosity and thermal conductivity of the gas mixture are calculated by using the semiempirical formula of Wilke:

$$\mu_m \text{ or } \lambda_m = \sum_{i=1}^N \left[X_i (\mu_i \text{ or } \lambda_i) / \left(\sum_{i=1}^N X_i \varphi_{ii} \right) \right]$$

where

$$\varphi_{ii} = \{1 + [(\mu_i \text{ or } \lambda_i)/(\mu_i \text{ or } \lambda_j)]^{1/2} (M_j/M_i)^{1/4}\}^2 / (8 + 8M_j/M_i)^{1/2}$$

The mixture specific heat was calculated as a mole fraction weighted average of the specific heats of each contributing species:

$$C_{pm} = \left(\sum_{i=1}^N X_i C_{pi} \right) / M$$

Fuel properties for *n*-heptane were approximated as a function of the temperature from the various sources.^{22,23} In this study, the following correlations were used:

latent heat of vaporization

$$L = 316.3(3.204 - T_r/168.6)^{0.38}, \text{ kJ kg}^{-1}$$

vapor mass fraction at the droplet surface

$$Y_{F,s} = \left(1 + \frac{M_s}{M_F} \left\{ \exp \left[\frac{LM_F}{R} \left(\frac{1}{T} - \frac{1}{T_s} \right) \right] - 1 \right\} \right)^{-1}$$

binary diffusion coefficient

$$D = 5.94 \times 10^{-6} (T/273)^{1.60} P^{-1}, \text{ m}^2 \text{ s}^{-1}, \text{ with } P \text{ in atm}$$

vapor specific heat

$$C_{pF} = -51.56 + 6.776T - 3.658 \times 10^{-3}T^2 - 7.673 \times 10^{-7}T^3, \text{ J kg}^{-1} \text{ K}^{-1}$$

vapor thermal conductivity

$$\lambda_F = -4.401 \times 10^{-2} + 2.514 \times 10^{-4}T - 3.173 \times 10^{-7}T^2 + 2.487 \times 10^{-10}T^3, \text{ J m}^{-1} \text{ s}^{-1} \text{ K}^{-1}$$

vapor dynamic viscosity

$$\mu_F = 3.83 \times 10^{-6} - 3.613 \times 10^{-9}T + 4.911 \times 10^{-11}T^2 - 3.577 \times 10^{-14}T^3, \text{ kg m}^{-1} \text{ s}^{-1}$$

Liquid fuel properties were assumed to be constant and evaluated at some average temperature $T_l = (T_u + T_b)/2 = 332.8 \text{ K}$. They are as follows:

$$\begin{aligned} C_{pl} &= 2383.89, \text{ J kg}^{-1} \text{ K}^{-1} \\ \lambda_l &= 1.1768 \times 10^{-1}, \text{ J m}^{-1} \text{ s}^{-1} \text{ K}^{-1} \\ \rho_l &= 649.38, \text{ kg m}^{-3} \end{aligned}$$

Acknowledgments

This work is supported by AFOSR Grant F49620-92-J-0231, with Julian M. Tishkoff as the Program Manager. Many fruit-

ful discussions with W. M. Roquemore at Wright-Patterson Air Force Base, Dayton, Ohio, are greatly appreciated.

References

- Ross, H. D., "Overview of NASA's Microgravity Combustion Science and Fire Safety Program," Second International Microgravity Combustion Workshop, Cleveland, OH, 1992.
- Burke, S. P., and Schumann, T. E. W., *Industrial and Engineering Chemistry*, Vol. 20, 1928, p. 998.
- Hottel, H. C., and Hawthorne, W. R., *Third Symposium on Combustion*, Williams and Wilkins, Baltimore, MD, 1949, p. 254.
- Bahadori, M. Y., Edelman, R. B., Stocker, D. P., and Olson, S. L., "Ignition and Behavior of Laminar Gas-Jet Diffusion Flames in Microgravity," *AIAA Journal*, Vol. 28, No. 2, 1990, pp. 236-244.
- Bahadori, M. Y., Stocker, D. P., Vaughan, D. F., Zhou, L., and Edelman, R. B., "Effects of Buoyancy on Laminar, Transitional, and Turbulent Gas Jet Diffusion Flames," Second International Microgravity Combustion Workshop, NASA CP 10113, Cleveland, OH, 1992.
- Bahadori, M. Y., Hegde, U., Zhou, L., and Stocker, D. P., "Effect of Gravity on the Transition to Turbulence of Gas-Jet Diffusion Flames," AIAA Paper 93-0710, Jan. 1993.
- Davis, R. W., Moore, E. F., Roquemore, W. M., Chen, L. D., Vilimoc, V., and Goss, L. P., *Combustion and Flame*, Vol. 83, 1991, pp. 263-270.
- Katta, V. R., and Roquemore, W. M., "Role of Inner and Outer Structures in Transitional Jet Diffusion Flame," *Combustion and Flame*, Vol. 92, 1993, pp. 274-282.
- Katta, V. R., Goss, L. P., and Roquemore, W. M., "Effect of Nonunity Lewis Number and Finite-Rate Chemistry on the Dynamics of a Hydrogen-Air Jet Diffusion Flame," *Combustion and Flame*, Vol. 96, 1994, pp. 60-74.
- Chung, J. N., and Troutt, T. R., "Simulation of Particle Dispersion in an Axisymmetric Jet," *Journal of Fluid Mechanics*, Vol. 186, 1988, pp. 199-222.
- Hansell, D., Kennedy, I. M., and Kolmann, W., "A Simulation of Particle Dispersion in a Turbulent Jet," *International Journal of Multiphase Flow*, Vol. 18, No. 4, 1992, pp. 559-576.
- Lazaro, B. J., and Lasheras, J. C., "Particle Dispersion in the Developing Free Shear Layer. Part 1-Unforced Flow," *Journal of Fluid Mechanics*, Vol. 235, 1992, pp. 143-178.
- Lazaro, B. J., and Lasheras, J. C., "Particle Dispersion in the Developing Free Shear Layer. Part 2-Forced Flow," *Journal of Fluid Mechanics*, Vol. 235, 1992, pp. 179-221.
- Samimy, M., and Lele, S. K., "Motion of Particles with Inertia in a Compressible Free Layer," *Physics of Fluids*, Vol. A3, 1991, pp. 1915-1923.
- Hishida, K., Ando, A., and Maeda, M., "Experiments on Particle Dispersion in a Turbulent Mixing Layer," *International Journal of Multiphase Flow*, Vol. 18, No. 2, 1992, pp. 181-194.
- Longer, E. K., and Eaton, J. K., "Structure of a Particle-Laden Round Jet," *Journal of Fluid Mechanics*, Vol. 236, 1992, pp. 217-257.
- Uthuppan, J., Aggarwal, S. K., Grinstein, F. F., and Kailasanath, K., "Particle Dispersion in a Transitional Axisymmetric Jet: A Numerical Simulation," AIAA Paper 93-0105, Jan. 1993.
- Aggarwal, S. K., "Relationship Between Stokes Number and Intrinsic Frequencies in Particle Laden Flows," *AIAA Journal*, Vol. 32, No. 6, 1994, pp. 1322-1325.
- Faeth, G. M., "Evaporation and Combustion of Sprays," *Progress in Energy and Combustion Science*, Vol. 9, No. 2, 1983, pp. 1-76.
- Aggarwal, S. K., Tong, A., and Sirignano, W. A., "A Comparison of Vaporization Models for Spray Calculation," *AIAA Journal*, Vol. 22, No. 10, 1984, pp. 1448-1457.
- Leonard, B. P., "A Stable and Accurate Convective Modelling Procedure Based on Quadratic Upstream Interpolation," *Computational Methods in Applied Mechanics and Engineering*, Vol. 19, 1979, pp. 59-98.
- Vargaftik, N. B., *Handbook of Physical Properties of Liquids and Gases*, 2nd ed., Hemisphere, New York, 1983, pp. 632-643.
- Ho, C. Y., Liley, P. E., Makita, T., and Tanaka, Y., *Properties of Inorganic and Organic Fluids*, Hemisphere, New York, 1988, pp. 137-150.



0017-9310(95)00324-X

A numerical study of droplet–vortex interactions in an evaporating spray

T. W. PARK† and S. K. AGGARWAL‡

Department of Mechanical Engineering, University of Illinois at Chicago, Chicago, IL 60607, U.S.A.

and

V. R. KATTA§

System Research Laboratory, Inc., Dayton, OH 45440, U.S.A.

(Received 23 March 1995 and in final form 28 August 1995)

Abstract—In this paper, we present the time-dependent axisymmetric numerical simulation of a n-heptane evaporating spray, and investigate the droplet–vortex interactions which determine the structural and dynamic characteristics of a spray jet flow. The spray is formed between a droplet-laden heated nitrogen jet and a coflowing air stream. A detailed, multidimensional, two-phase algorithm is developed for the simulation. Monodisperse spray is introduced into the large vortex structures that are generated by the buoyancy-induced hydrodynamic instability of the heated jet. Results focus on the two-way interactions between vortical structures and droplets, and the dynamics of both non-evaporating and evaporating sprays. The vortex structures cause droplets to disperse radially outward, and this in turn determines the fuel vapor distribution and also modifies the vortex dynamics. Thus, the dynamics and structural characteristics of evaporating sprays are strongly influenced by the two-way transient interactions. The effects of initial droplet size, injection location, and liquid-to-gas mass loading ratio on these interactions are investigated. These studies indicate that the effect of dispersed phase on gas phase is negligible for mass loading ratio less than 0.5. At higher mass loading ratios, the dispersed phase modifies the dynamics of vortex structures but not the time-average behavior for non-evaporating spray, while for evaporating spray it influences both the dynamics and the time-averaged behavior. It is also found that the spray injection characteristics have strong influence on the processes of droplet–vortex interactions. Copyright © 1996 Elsevier Science Ltd.

INTRODUCTION

Large-scale, coherent vortical structures have been found to exist in a variety of shear flows including those involving combustion and multiple phases [1–4]. In two-phase shear flows involving solid particles or liquid droplets, the transient interactions between dispersed phase and large vortical structures are expected to play a central role in determining the dynamics and structural characteristics of these flows. The transient interactions pertain to the effect of large vortical structures on the behavior of droplets/particles, and the influence of droplets on the dynamics of large vortical structures. These two effects coupled in a nonlinear manner; the vortex structures determine the droplet dispersion and gasification behavior, which in turn affects the local environment surrounding each droplet and thereby the dynamics

of the two-phase system under consideration. Several numerical [5, 6] and experimental [7–10] studies in recent years have focused on the one-way coupling, examining the influence of large eddies on the dynamics of droplets/particles injected into a shear flow. These studies show that the effect of large structures on particle motion is characterized by the ratio of particle response time to characteristic time of structures. This ratio is defined as the Stokes number (St). When the particle response time is of the same order of magnitude as the vortex time scale, $St \sim O(1)$, particles can disperse significantly more than the fluid particles, the enhanced dispersion being attributed to the centrifugal action of vortices. For small Stokes number, $St \ll 1.0$, particles behave similar to the fluid particles, while for large Stokes number, particles remain largely unaffected by the vortices. More recent works [11, 12] on particle-laden flows have examined the effect of external forcing on the particle dispersion behavior. A general observation from these studies [11, 12] is that the dynamics of vortex structures, and thereby the dispersion behavior of particles in a shear layer can be manipulated by a subharmonic forcing of the shear layer.

Particle-laden shear flows in practical applications

† Currently at Wright Laboratory, Aero Propulsion and Power Directorate, Wright-Patterson Air Force Base, OH 45433, U.S.A., as a National Research Council Research Associate.

‡ Author to whom correspondence should be addressed.

§ Present address: Innovative Scientific Solutions, Inc., Dayton, OH 45430, U.S.A.

NOMENCLATURE

C_p	specific heat	u	axial velocity
d_o	initial droplet diameter	v	radial velocity
D	vapor/air binary diffusion coefficient	Y	mass fraction
g	acceleration of gravity	z	axial distance.
h_{fs}	enthalpy of fuel vapor at droplet surface	Greek symbols	
$l_{k,eff}$	effective latent heat, or the heat transferred from gas phase to droplet	μ	dynamic viscosity
\dot{m}_k	droplet vaporization rate	λ	thermal conductivity
M	ratio of the liquid fuel mass flow rate to the nitrogen mass flow rate	ρ	density.
M_k	mass of each group of droplets	Subscripts	
n_k	number of droplets in each group	f	fuel vapor
p	pressure	g	gas-phase
r	radial distance	k	droplet characteristic
t	time	l	liquid-phase
T	temperature	o	oxygen
		s	surface.

involve two-way, nonlinear interactions between the continuous and dispersed phases. Previous studies cited above focus mainly on the one-way interactions, i.e. on characterizing the effect of vortex structures on droplet motion and dispersion behavior. The effects of dispersed phase on vortex dynamics, and subsequently on fuel vapor distribution and flame behavior remain largely unexplored. In this paper, we report a numerical study of two-way droplet-vortex interactions in an unsteady evaporating spray. The spray is formed between a droplet-laden heated nitrogen jet and a coflowing air stream. The jet velocity and temperature are considered in a range where the large vortical structures are generated due to the buoyancy-induced hydrodynamic instability rather than the shear-induced Kelvin-Helmholtz instability. The vaporization characteristics of n-heptane fuel spray under the influence of two-way droplet-vortex interactions are investigated. The additional complexities due to chemical reactions and heat release are avoided so as to focus on the dynamics of two-way interactions. A non-evaporating spray is also analyzed in order to distinguish the interactions involving only momentum transfer between the phases from those involving mass, momentum, and energy transfer. Results are presented that highlight the dynamics as well as the time-averaged structure of these sprays.

PHYSICAL MODEL

The evaporating spray investigated in the present study is shown schematically in Fig. 1. It consists of a central fuel jet which is a two-phase mixture of gaseous nitrogen and liquid fuel droplets and a low-speed coannulus air flow. The central jet is heated primarily to enhance the fuel evaporation; however, in the pre-

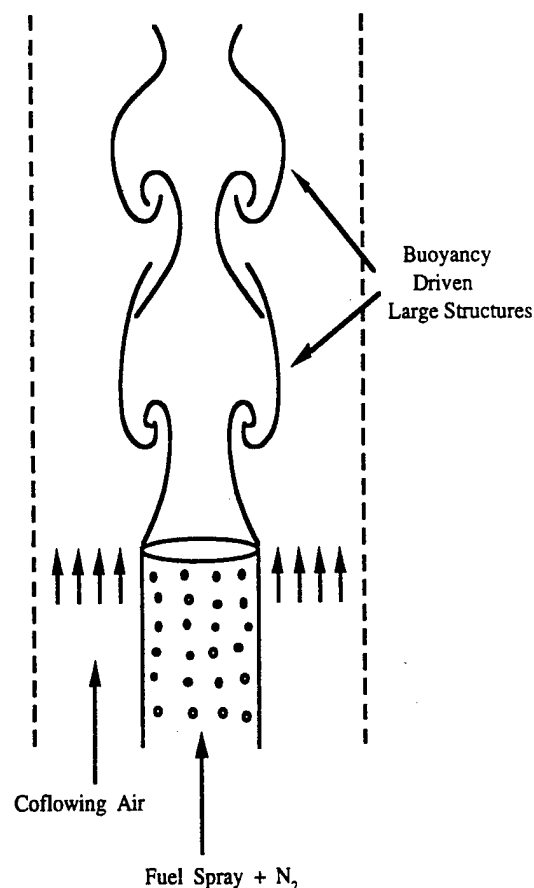


Fig. 1. A schematic of evaporating spray jet at 1 g.

sent studies, it also plays a key role for the formation of buoyancy induced vortical structures. Numerical studies on the two-way interactions between the vor-

Table 1. Transport coefficients and source terms appearing in governing equations

Equations	Φ	Γ^Φ	S_s^Φ	S_i^Φ
Continuity	1	0	0	$\sum_k n_k \dot{m}_k$
Axial momentum	u	μ	$-\frac{\partial p}{\partial z} + (\rho_o - \rho)g + \frac{\partial}{\partial z}\left(\mu \frac{\partial u}{\partial z}\right) + \frac{\partial}{\partial r}\left(\mu \frac{\partial v}{\partial z}\right) + \frac{\mu}{r} \frac{\partial v}{\partial z}$ $-\frac{2}{3}\left\{\frac{\partial}{\partial z}\left(\mu \frac{\partial u}{\partial z}\right) + \frac{\partial}{\partial z}\left(\mu \frac{\partial v}{\partial r}\right) + \frac{\partial}{\partial z}\left(\mu \frac{v}{r}\right)\right\}$	$\sum_k \left(n_k \dot{m}_k u_k - n_k M_k \frac{du_k}{dt}\right)$
Radial momentum	v	μ	$-\frac{\partial p}{\partial r} + \frac{\partial}{\partial z}\left(\mu \frac{\partial u}{\partial r}\right) + \frac{\partial}{\partial r}\left(\mu \frac{\partial v}{\partial r}\right) + \frac{\mu}{r} \frac{\partial v}{\partial r} - 2\mu \frac{v}{r^2}$ $-\frac{2}{3}\left\{\frac{\partial}{\partial r}\left(\mu \frac{\partial u}{\partial z}\right) + \frac{\partial}{\partial r}\left(\mu \frac{\partial v}{\partial r}\right) + \frac{\partial}{\partial r}\left(\mu \frac{v}{r}\right)\right\}$	$\sum_k \left(n_k \dot{m}_k v_k - n_k M_k \frac{dv_k}{dt}\right)$
Mass fraction of fuel	Y_f	ρD_f	0	$\sum_k n_k \dot{m}_k$
Mass fraction of oxygen	Y_o	ρD_o	0	0
Energy	T	λ/C_p	0	$\sum_k n_k \dot{m}_k (h_{fs} - 1_{k,eff})$

tex structures and the evaporating droplets are conducted by solving the unsteady, axisymmetric gas-phase equations that include the droplet source terms, and the appropriate droplet equations.

The unsteady, axisymmetric governing equations in cylindrical (z, r) coordinate system for a droplet-laden heated jet are

$$\begin{aligned} \frac{\partial(\rho\Phi)}{\partial t} + \frac{\partial(\rho u\Phi)}{\partial z} + \frac{\partial(\rho v\Phi)}{\partial r} \\ = \frac{\partial}{\partial z}\left(\Gamma^\Phi \frac{\partial\Phi}{\partial z}\right) + \frac{\partial}{\partial r}\left(\Gamma^\Phi \frac{\partial\Phi}{\partial r}\right) \\ - \frac{\rho v\Phi}{r} + \frac{\Gamma^\Phi}{r} \frac{\partial\Phi}{\partial r} + S_s^\Phi + S_i^\Phi. \quad (1) \end{aligned}$$

The general form of equation (1) represents the continuity, momentum, species, or energy conservation equation depending on the variable used for Φ . Table 1 gives the transport coefficients Γ^Φ and the source terms S_s^Φ and S_i^Φ that appear in the governing equations. In this table, μ , λ and C_p represent the viscosity, the thermal conductivity and the specific heat, respectively. They are considered functions of temperature and species concentration.

The effect of dispersed phase on gas-phase properties is incorporated through the source/sink terms (S_i^Φ), representing the exchange of mass, momentum, and energy between the gas and liquid phases. In order to evaluate these terms, it is necessary to establish droplet trajectories, size and temperature histories. The Lagrangian approach is employed to solve the liquid-phase governing equations for the dynamics and vaporization history of each droplet group. The spray is characterized by a discrete number of droplet groups, distinguished by their injection location, initial size and time of injection. A droplet group in a Lagrangian treatment represents a characteristic containing a finite number of droplets. Since an axi-

symmetric configuration is analyzed, the liquid properties are implicitly averaged in the azimuthal direction and the number of droplets associated with each characteristic represents droplets uniformly distributed in an annual ring. The equations governing the variation of position, velocity, and size for each droplet group and other expressions are available in ref. [13]. A comprehensive vaporization model is employed to calculate the instantaneous droplet size and surface temperature along the trajectory of each group. The model includes the effects of variable thermophysical properties, non-unity Lewis number in the gas film outside the droplet, the effect of Stefan flow on the heat and mass transfer between the droplet and the gas, and the effect of transient liquid heating. The variable thermophysical properties are calculated at reference film temperature and concentrations, obtained by using the 1/3 rule, except for the gas density which is calculated at the free stream value [14]. The Wilke rule [15] is used to calculate the dynamic viscosity and thermal conductivity of the gas film. The liquid fuel ($n\text{-C}_7\text{H}_{16}$) properties are collected from the various sources and approximated as a function of the temperature [13]. The effect of transient liquid heating is incorporated by using the finite-conductivity model [16]. This model is deemed satisfactory in the present study, since the maximum droplet Reynolds number during droplet lifetime is less than ten and thus the effect of internal circulation is expected to be negligible. For the same reason, the effects of gas-phase convection on the heat and mass transport are represented by the Ranz-Marshall correlation [16].

SOLUTION PROCEDURE

The numerical solution of the unsteady two-phase equations employs an implicit algorithm for solving the gas-phase equations, and an explicit Runge-Kutta procedure for the liquid-phase equations. The finite-

difference forms of the momentum equations are obtained using an implicit QUICKEST scheme [17], while those of the species and energy equations are obtained using a hybrid scheme of Spalding [18]. A "finite control volume" approach with a staggered, non-uniform grid system is utilized. Body force term due to gravitational field is included in the axial momentum equation for gas-phase and the droplet motion equation for liquid-phase. An iterative ADI (Alternative Direction Implicit) technique is used for solving the resulting sets of algebraic equations. A stable numerical integration procedure is achieved by coupling the species and energy equations through the source terms (cf. Table 1). At every time step, the pressure field is calculated by solving the pressure Poisson equations simultaneously and utilizing the LU (Lower and Upper diagonal) matrix decomposition technique. It should be noted that the pressure Poisson equations consider the effect of mass transfer from the liquid phase to the gas phase, represented by a source term in the gas-phase mass continuity equation.

The liquid-phase equations are advanced in time by a second-order accurate Runge-Kutta method. Since the gas-phase solution employs an implicit procedure, the temporal step size used for integrating the liquid-phase equations is smaller than that for gas-phase equations. An automatic procedure is implemented in order to select an optimum liquid-phase time step. The procedure involves calculating the characteristic thermal response time, velocity response time and vaporization time for each droplet group, and then selecting the temporal step size as a fraction (one-hundredth) of the smallest of these time scales. A detailed examination of the various time scales, based on numerical experiments, revealed that the temporal step size is determined by either the thermal response time or the velocity response time of a given droplet group. The number of subcycles for advancing the liquid-phase solution for each gas-phase cycle typically varies from two to ten, depending upon the droplet size.

The procedure to advance the two-phase solution over one gas-phase time step is as follows. Using the known gas-phase properties, the liquid-phase equations are solved over a specified number of liquid-phase subcycles. A third-order accurate Lagrangian polynomial method is used for interpolating the gas-phase properties from the non-uniform fixed grid to the droplet characteristic location. It should be noted that the interpolation scheme for the gas-phase velocities u and v is based on their respective grid cells because of the use of a staggered grid in gas-phase calculation. The droplet properties are updated after every liquid-phase subcycle. Also, during each subcycle, the liquid-phase source terms appearing in the gas-phase equations are calculated at the characteristic location, and then distributed to the surrounding gas-phase grid points. These source terms are added at each gas-phase grid points during one gas-phase time step and then used in the implicit solution of the gas-phase equations.

RESULTS

The jet diameter of the vertically mounted evaporating spray considered in the present study is 2.54 cm. The jet velocities for the central fuel and coannular air streams are 1.0 and 0.2 m s⁻¹, respectively. Flat velocity profiles are used as the inflow conditions. Temperature chosen for the fuel jet is 1200 K while that of the surrounding annulus air is 294 K. Calculations are made for a physical domain having dimensions of 15 and 40 cm in the radial and axial direction, respectively. It should be noted that the physical domain used in the calculations is much larger than the domain of interest (3 × 20 cm) and hence, the results are not influenced by the computational boundaries. Results reported in the present paper are obtained using a grid system having 151 and 61 points in the axial and radial directions, respectively. Grid lines are clustered near the shear layer to resolve the steep gradients of the dependent variables. Calculations are advanced in time utilizing a low CFL number of 0.2. In an earlier study [13], it was found that the results obtained on a 151 × 61 mesh system (with grid spacings similar to the ones used in the present investigation) and using a CFL number less than 0.5 are grid independent and time accurate.

Numerical experiments are conducted by injecting different groups of droplets into the fuel stream to examine the changes in the flow structure due to the two-way nonlinear, two-phase interactions. The injection process consists of introducing a group of monodisperse droplets at a given instant of time. The number of droplets in each group depends on the mass loading (ratio of the liquid fuel mass flow rate to the nitrogen mass flow rate), initial droplet size, and injection time interval. As a base case for the spray calculations reported in this work, a monodisperse *n*-heptane spray with an initial diameter of 200 μm and mass loading of unity is considered. At a mass loading of unity, the volume occupied by liquid phase is about three orders of magnitude smaller than that of the gas-phase volume due to the high density of the liquid fuel and hence, the dilute-spray assumption is still valid. At higher mass loading, however, the assumption would become increasingly more questionable. For this reason, the mass loading of unity is the highest loading considered in the present study. The droplets are injected continuously into the jet shear layer from a radial location of 1.25 cm. A time difference of 1.428 ms ($= 9 \Delta t_{\text{gas}}$) is used between two consecutive injections for all the spray calculations reported in this work. This time interval was determined based on the constraint that the spatial separation between two successive droplet groups is large enough for neglecting the interaction between the droplets. This yields the number of droplets in each group to be 76. Three different droplet injection intervals are chosen to examine their effect on the time-averaged temperature and axial velocity profiles in the flow field. Figure 2 shows the time-averaged axial profiles of

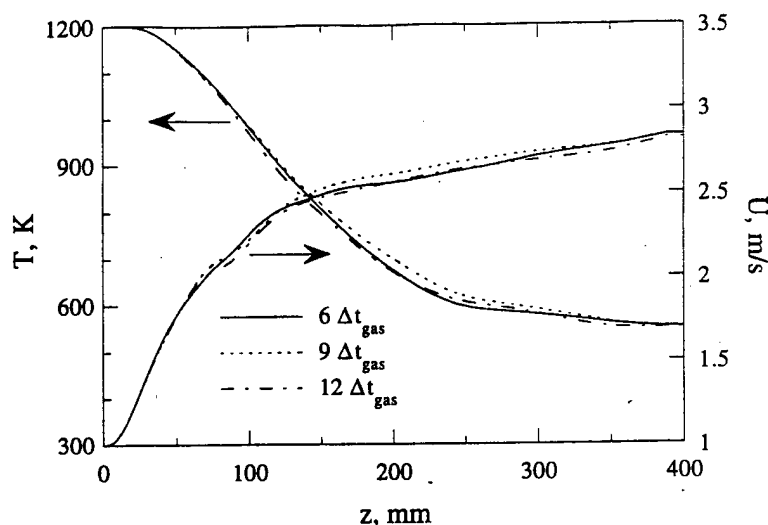


Fig. 2. Effect of droplet interval on the time-averaged temperature and axial velocity profiles of 200- μm evaporating spray with mass loading value of $M = 1.0$.

temperature and axial velocity for the three cases. As expected, the average temperature decreases along the jet axis due to gas-phase heat transport processes and cooling caused by the dispersed phase. The average axial velocity, however, increases in the axial direction due to buoyant acceleration. The important observation is that the gas-phase calculations are not sensitive to the droplet injection interval used for the base case.

The effect of dispersed phase on the dynamics of vortex structures and heated jet is portrayed in Figs. 3 and 4. Calculations are initially made without inject-

ing droplets into the fuel stream. The shear layer between the 1200-K nitrogen jet and the cold annulus air flow became unsteady with the development of large-scale vortices. Iso-temperature contours of this heated jet are shown in Fig. 3(a). It is important to note that these vortical structures are generated without using any external forcing, and their dynamics is found to be highly periodic. The role of gravity on the

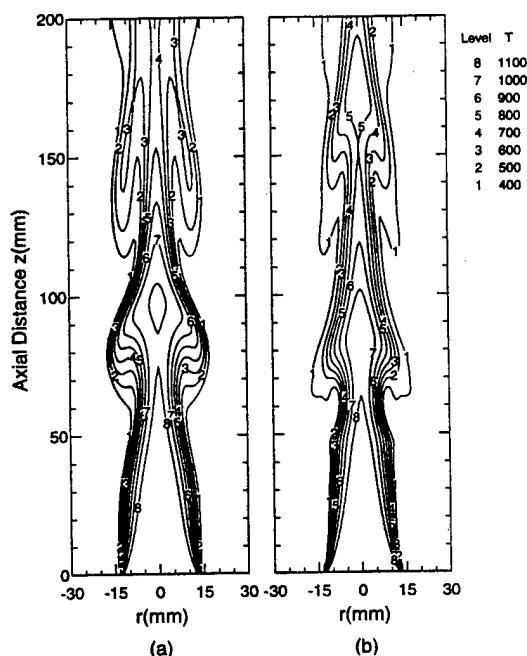


Fig. 3. Instantaneous iso-temperature contours for the heated jet: (a) without fuel spray; (b) with fuel spray.

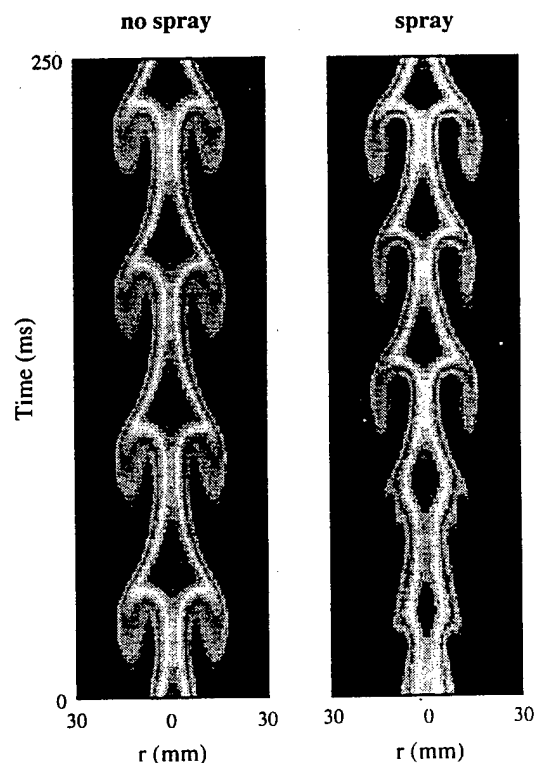


Fig. 4. Time evolution of temperature contours at axial location of 10 cm above the inlet for the cases of Fig. 3.

dynamics of the heated jet was confirmed by performing numerical experiments. When the gravitational term in the axial momentum was set equal to zero, the simulation yielded a steady laminar jet flow. This observation is in contrast with that made for heated jet flows at higher Reynolds number, in which Kelvin-Helmholtz instabilities develop independent of the assumption made for gravitational force. Most of the experimental studies on heated jets [19, 20] were focused on the higher Reynolds-number flow and did not provide insight on buoyancy-induced instabilities. However, the latter ones were extensively investigated experimentally in jet diffusion flames [21, 22] and helium jets [23]. The numerical studies [24, 25] performed on these flames and helium jet flows using the code discussed in the present study predicted the growth of buoyancy-induced instabilities very accurately.

Instantaneous iso-temperature contours for the case with fuel spray [plotted in Fig. 3(b)] are compared with the ones obtained without introducing fuel spray in Fig. 3(a). All the droplet source terms (Table 1) are incorporated in the gas-phase equations for the simulation with fuel spray. For both the cases, the buoyancy-induced vortex structures shown in Fig. 3 appear naturally without any external forcing. It is apparent from the figure that the injection of 200- μm droplets into the shear layer weakened the vortical structures and decreased the spreading of the heated jet. The weakening of vortical structures is probably caused by the cooling effect of the dispersed phase, while the decrease in the spreading rate may be expected due to fact that the addition of fuel spray to the nitrogen gas increases the jet momentum. Figure 3 further indicates that the jet oscillations are highly coherent for the gaseous (no spray) case and somewhat less coherent for the spray case. Since the presence of liquid phase modifies the spectral characteristics or the dominant instability frequency, an attempt was made to phase-lock the instantaneous images for the two cases. Consequently, the temperature contour plots in Fig. 3 for the gaseous and spray cases represent the results that are obtained at slightly different times from the start of the respective calculation.

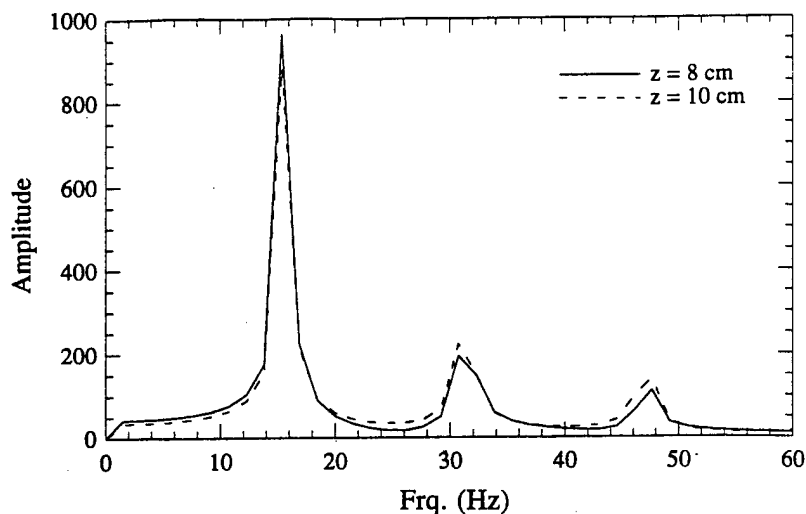
The dynamics of vortex structures is examined by plotting the time evolution of temperature contours in Fig. 4. Temperature data along the radial location at an axial location of 10 cm above the jet exit for the gaseous and spray cases are recorded over a time period of 250 ms and shown in this figure. Again, an attempt was made to phase-lock the images for the gaseous and spray case. It can be seen from Fig. 4(a) that the vortex structures in the case of gaseous jet are highly coherent and periodic. With the addition of fuel spray the dynamics of jet has become aperiodic and the vortex crossing frequency (obtained by counting the number of vortices in a fixed time interval) has increased by about 30%. This can be confirmed by performing the spectral analysis at different axial

locations in the shear layer. Temperature data were recorded at different locations during more than 10 vortex crossing times ($4096 \Delta t_{\text{gas}}$). Figure 5 clearly shows that the dominant frequency for the spray case is increased to 20.5 Hz which is about 30% higher compared to the frequency observed for the gaseous jet case. In addition, the deterioration in coherency can be seen for the spray case. The increase in frequency for the spray case is resulting from the momentum transfer between the liquid drops and the gaseous flow. The fuel drops are injected into the gaseous jet shear layer at the same velocity as that of the local gas velocity which yields higher momentum to the fuel drops. As the gaseous flow and drops convect downstream, the higher momentum of the latter transfer to the former which, in turn, increases the local gas velocity. As a result, the crossing frequency of the vortices in the shear layer, which is proportional to the local gas velocity, also increases. The increase in frequency is observed for both non-evaporating and evaporating sprays, implying again that this is primarily a momentum-transfer effect. It is also interesting to note that no vortex merging is observed for these two cases.

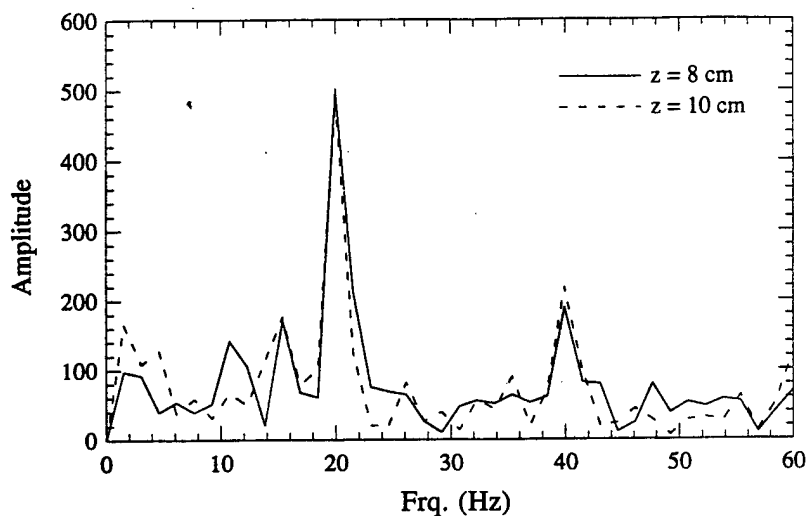
Effect of liquid mass loading

The structural changes noted in a buoyancy driven heated jet with the addition of fuel spray are resulting from (1) liquid mass loading, (2) droplet evaporation and (3) the two-way interaction between vortices and droplets. To further understand the impact of the above individual parameters, numerical experiments are performed by changing the liquid mass loading, evaporation characteristics, spray injection location and droplet size.

The instantaneous iso-temperature contours for five different mass loading values ($M = 0, 0.125, 0.25, 0.5$ and 1.0) for a non-evaporating spray are shown in Fig. 6. Again, the images shown in Fig. 6 are phase locked. Liquid mass flow rate is controlled by changing the number of droplets in each injected group. As the droplets are assumed to be non-evaporating in this case, only the source terms in the momentum equation (cf. Table 1) are considered in the gas-phase equations. In other words, only the momenta are exchanged in this two-phase flow calculation. The single-phase gaseous flow shown in Fig. 3(a) may be approximated as a non-evaporating spray in the limiting case of $M = 0$ [Fig. 6(a)]. It seems that the structural characteristics of low mass loading cases like $M = 0.125$ and 0.25 are similar to that of single-phase flow even though the vortex-crossing frequencies in these flows are somewhat different. The time history plots of the dynamic heated jets for different mass loading values are shown in Fig. 7. This plot clearly shows the changes in the sizes of the vortex structures and their crossing frequency for different cases. It may be observed from Fig. 7 that as the mass loading ratio is increased, the crossing frequency of vortex structures is also increasing. At higher mass loading



(a)



(b)

Fig. 5. Frequency spectra obtained from temperature data recorded within the shear layer at two different axial locations.

values ($M = 0.5$ and 1.0), the structural characteristics seem to change more significantly.

The effect of mass loading in an evaporating spray is depicted in Fig. 8 by plotting the phase-locked instantaneous temperature contours for the three different mass loading values ($M = 0.25, 0.5$ and 1.0). The gas-phase governing equations for this case include all the source/sink terms due to the exchange of mass, momentum and energy due to droplet dynamics and vaporization. Structure of the heated jet seems to change more significantly with the addition of evaporating spray compared to that of a non-evaporating one. Figure 9 shows the time evolution of temperature contours at $z = 7.5$ cm for the three cases shown in Fig. 8. It is interesting to compare

the structures of high mass loading values ($M = 0.5$ and 1.0) for the evaporating (Fig. 9) and non-evaporating (Fig. 7) cases. The development of vortical structures for evaporating spray is more periodic than that observed in the corresponding non-evaporating cases. This is probably due to the fact that for the evaporating case the effect of momentum coupling between the phases is reduced due to droplet vaporization.

The effect of dispersed phase on the time-averaged gas-phase properties for both non-evaporating and evaporating sprays with different mass loading values is portrayed in Fig. 10. The time period used in obtaining the average values was at least 10 vortex periods. In addition, it was verified that the average values

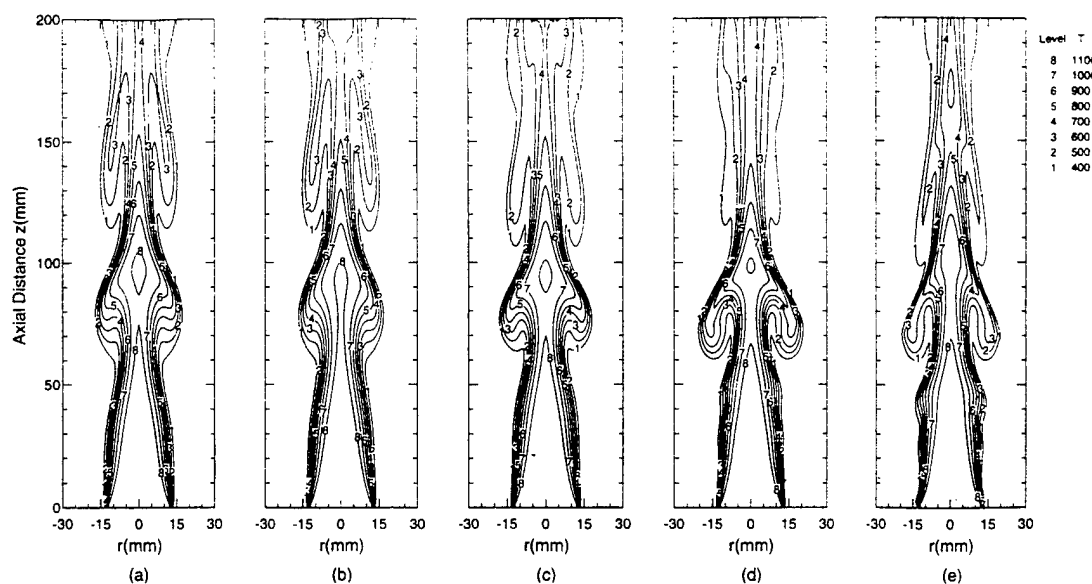


Fig. 6. Instantaneous iso-temperature contours for a 200- μ m non-evaporating spray jet with five different mass loading values; (a) $M = 0$, (b) $M = 0.125$, (c) $M = 0.25$, (d) $M = 0.5$ and (e) $M = 1.0$.

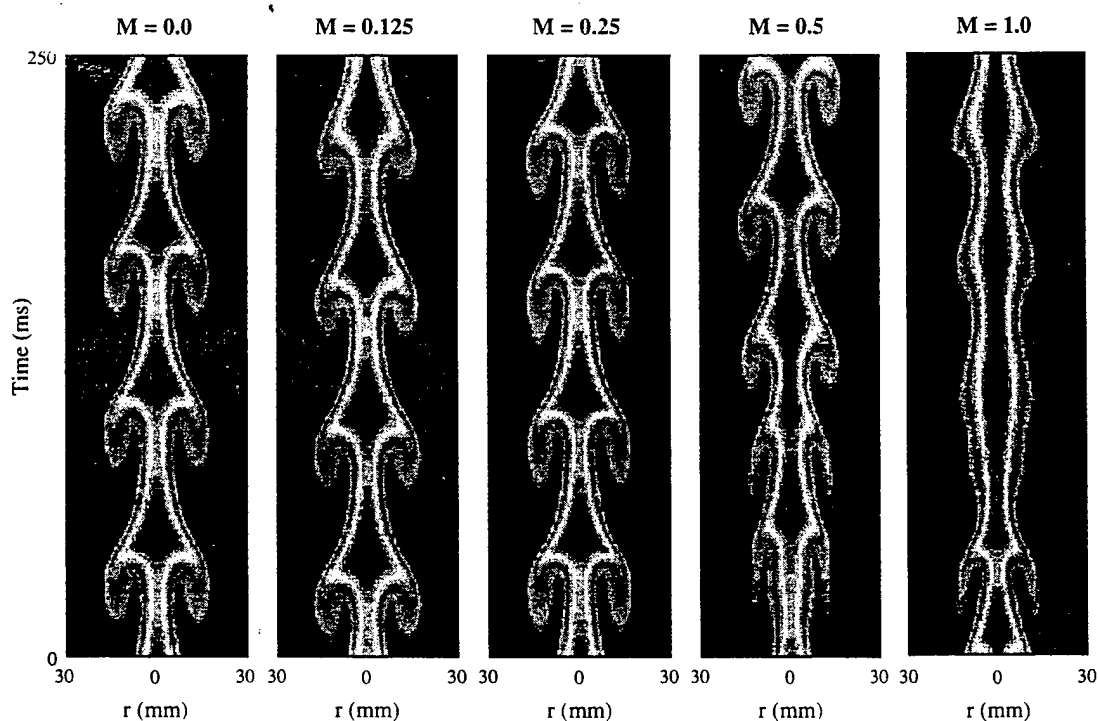


Fig. 7. Time evolution of temperature contours at axial location of 10 cm above inlet for the cases of Fig. 6.

shown in Fig. 10 were independent of this time period. An important observation is that the dispersed phase does not have any discernible influence on the time-averaged properties of non-evaporating spray jet. This is especially interesting in view of the fact that the vortex dynamics for the non-evaporation spray case is modified by the presence of the dispersed phase. As

expected, the average gas-phase properties of evaporating spray are significantly affected by the dispersed phase. The average gas temperature decreases along the jet axis due to the cooling caused by droplet vaporization. The decrease in gas temperature reduces the magnitude of buoyant acceleration, resulting in a lowering of average gas velocity compared to that for

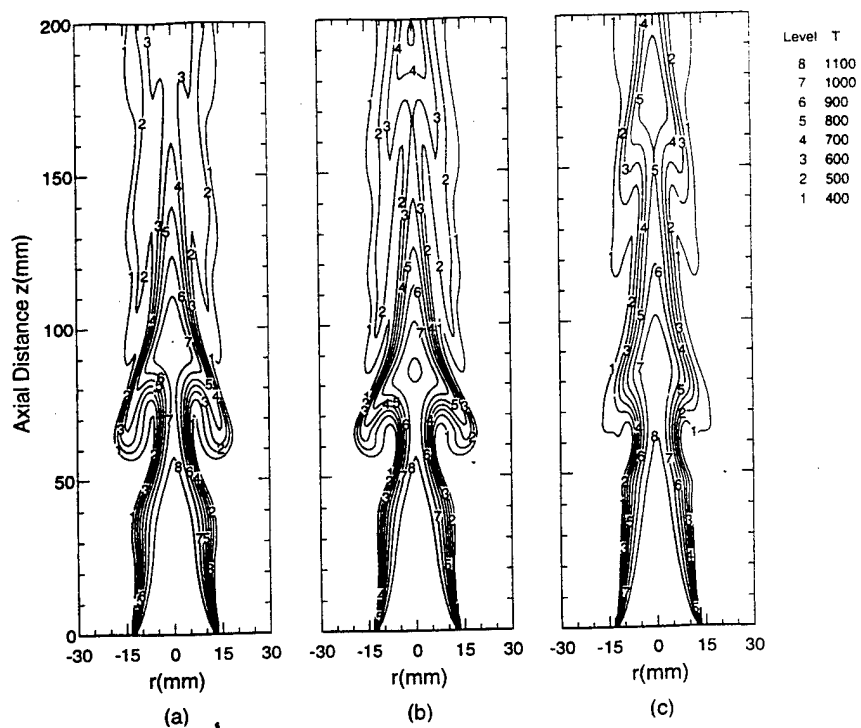


Fig. 8. Instantaneous iso-temperature contours for a 200- μm evaporating spray jet with three different mass loading values: (a) $M = 0.25$, (b) $M = 0.5$ and (c) $M = 1.0$.

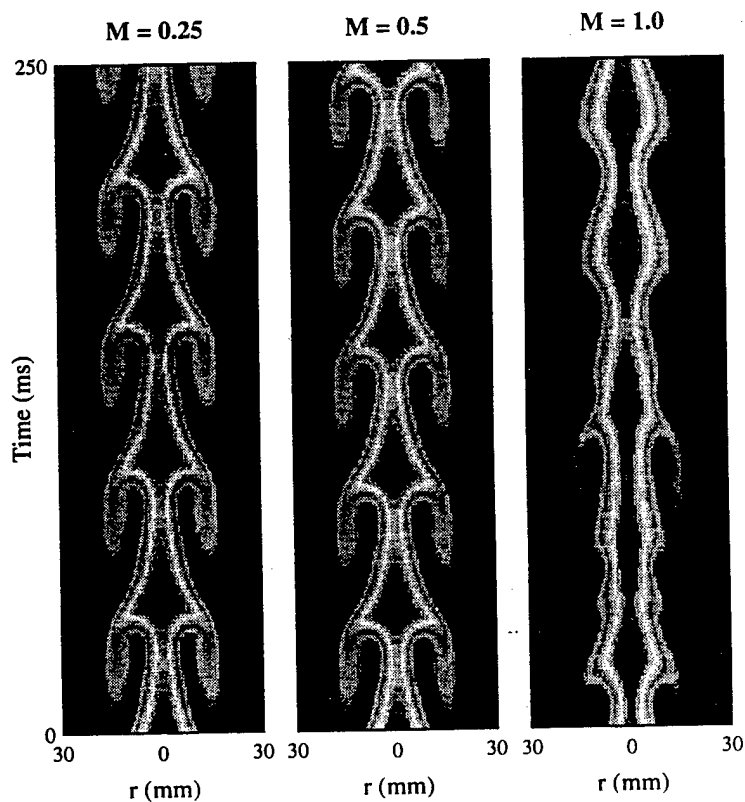


Fig. 9. Time evolution of temperature contours at a location of 7.5 cm above the inlet for the cases of Fig. 8.

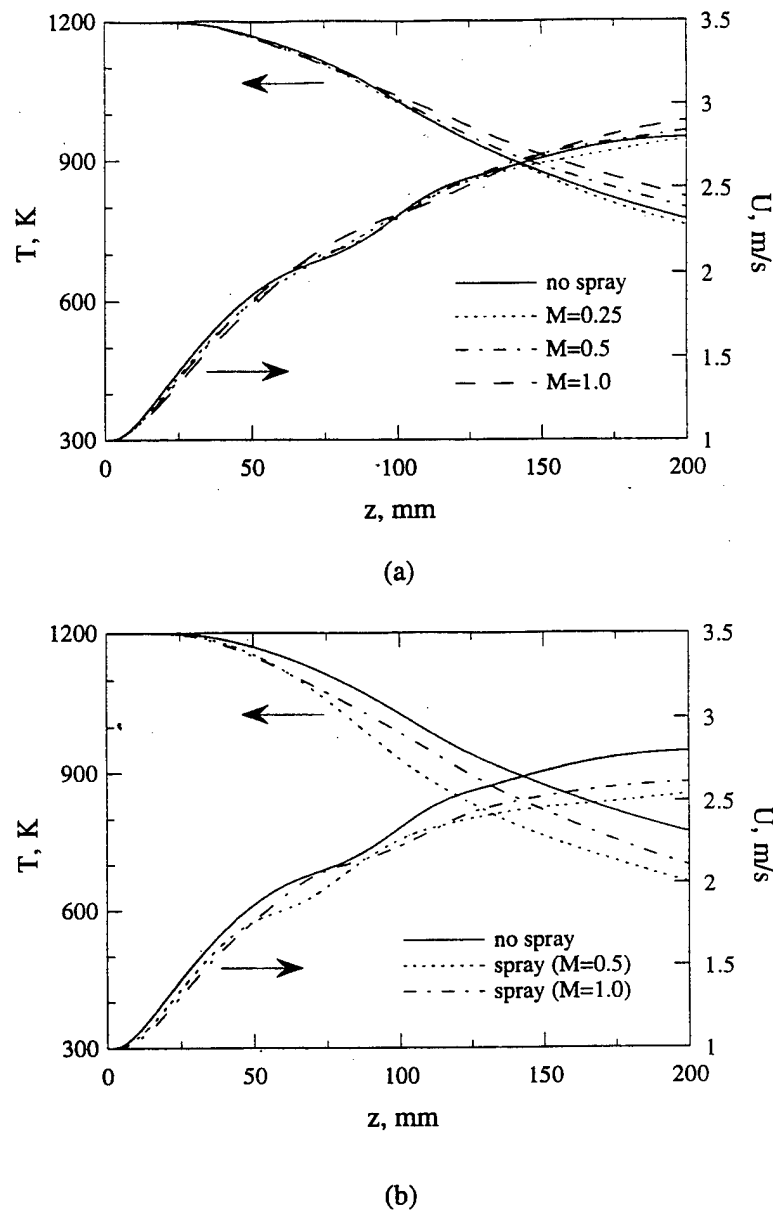


Fig. 10. Time-averaged axial profiles of gas temperature and axial velocity for (a) non-evaporating and (b) evaporating sprays with different liquid-to-gas loading ratios.

the gaseous case. Note that a reduction in the buoyant acceleration makes the vortex structures weaker as mentioned earlier.

Effect of injection characteristics

The effect of initial droplet distribution on the structural characteristics and dynamics of evaporating spray jet is studied by changing the injection characteristics. The mass loading ratio and droplet diameter are fixed at 1.0 and 200 μm , respectively. The instantaneous temperature contours for three cases having different droplet injection locations are shown in Fig. 11. The three distributions of injection locations used are as follows: (1) $r_k = 1.25$ cm, one injection

location, (2) $r_k = 0.625$ and 1.25 cm, two injection locations and (3) $r_k = 0.25, 0.50, 0.75, 1.00$ and 1.25 cm, five injection locations. The mass loading ratio is kept constant by using a different number of droplets in each group for different cases. It is seen that the characteristics of the core region near the nozzle exit are quite different for the three cases due to different droplet injection processes. The use of more injection locations apparently leads to a dynamic heated spray jet with well-organized vortical structures [Fig. 11(c)]. It is known that the vaporization of a liquid droplet absorbs thermal energy and hence reduces the local temperature. This is evident in Figs. 11(b) and (c). In the former figure a valley in the temperature contours

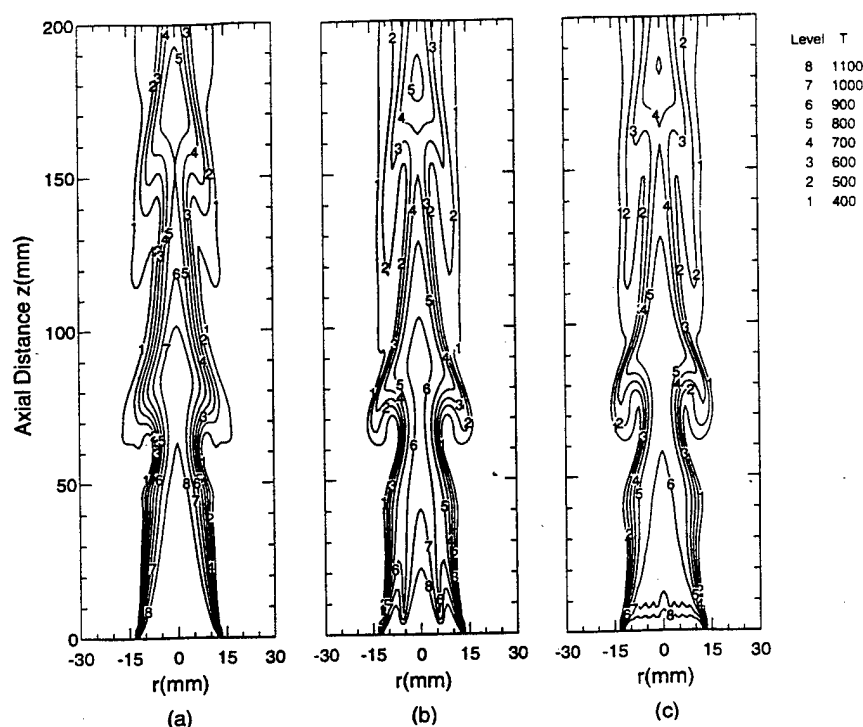


Fig. 11. Instantaneous iso-temperature contours for an evaporating spray jet with three different injection distributions; (a) $r_k = 1.25$ cm, one injection location, (b) $r_k = 0.625$ and 1.25 cm, two injection locations, (c) $r_k = 0.25, 0.5, 0.75, 1.0$ and 1.25 cm, five injection locations.

developed in the downstream region of the inner injection location (i.e. $r_k = 0.625$ cm) as the injected droplet vaporized. However, in the latter figure, the choice of more injection locations reduced the entire jet temperature uniformly leading to near flat contours for 1000 and 1100 K [contours 7 and 8 in Fig. 11(c)]. The time evolution of temperature contours at an axial location of 7.5 cm for the above three cases is plotted in Fig. 12. It clearly shows that the vortex structures are well organized and highly periodic similar to that of a single-phase flow (Fig. 3a) when the number of injection locations is increased. However, the vortex passage frequency for the spray case is different from that for the single-phase jet.

Effect of droplet size

In order to examine the effect of initial droplet size on the processes of droplet-vortex interactions, three different spray cases with initial droplet diameters of 200, 100 and 50 μm are considered. A constant mass loading ratio of $M = 1.0$ is maintained by increasing the number of droplets in each group as its initial size is decreased, and the droplets are injected in the shear layer ($r_k = 1.25$ cm). Results are portrayed in Fig. 13 in the form of snap shots of the flow field. For each case, instantaneous iso-temperature contours and velocity vectors are plotted on the left-hand and right-hand sides of the symmetric jet, respectively. It is quite evident from Fig. 13 that the initial droplet size has a strong influence on the dynamic and structural characteristics of the evaporating spray. For all three cases

shown in the figure, there is a reduction in gas temperature due to the vaporization of liquid fuel. However, as the initial droplet size decreases, there is increasingly pronounced cooling in the initial part of the jet caused by droplet vaporization, which affects both the shape and the dynamics of vortex structures. This can be seen more clearly in Fig. 14 which shows the time evolution of vortical structures for the three cases. In fact, when the initial droplet size is sufficiently small ($d_0 = 50 \mu\text{m}$), the jet temperature downstream of $z = 6$ cm is reduced to less than 500 K, and vortex structures seem to be destroyed. This drastic reduction in gas temperature is caused by the increased total liquid-phase surface area and entrainment of colder fluid into the jet interior. The latter is due to the vortex merging process and subsequent enlargement of vortex structures for the 50- μm spray case. Note that the vortex merging which occurs at an axial location between $z = 2.5$ and 5 cm is not shown in the figures (although there is some evidence of it in Fig. 13). However, the enlargement of vortex structures for the 50- μm spray can be clearly seen in Fig. 14. The vortex-merging process enhances the entrainment of colder fluid, which further reduces the gas temperature and weakens the vortex structures drastically. Figure 15 shows the effect of initial droplet size on the time-averaged axial profiles of temperature and axial velocity. The drastic reduction in gas temperature caused by droplet vaporization and entrainment of colder fluid, and the subsequent destruction of vortex structures can be clearly seen in this figure. Thus the

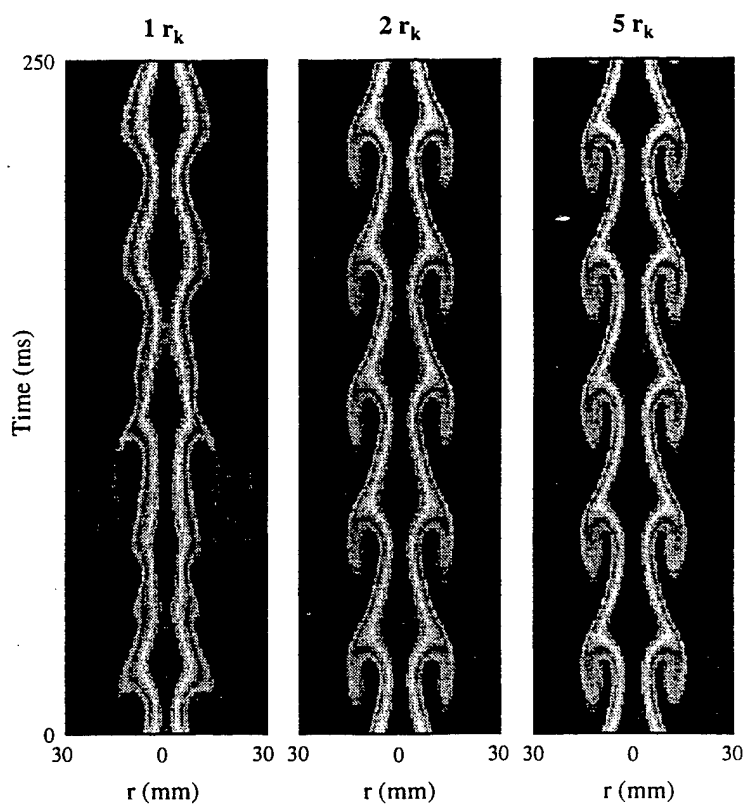


Fig. 12. Time evolution of temperature contours at axial location of 7.5 cm above inlet for the cases of Fig. 10.

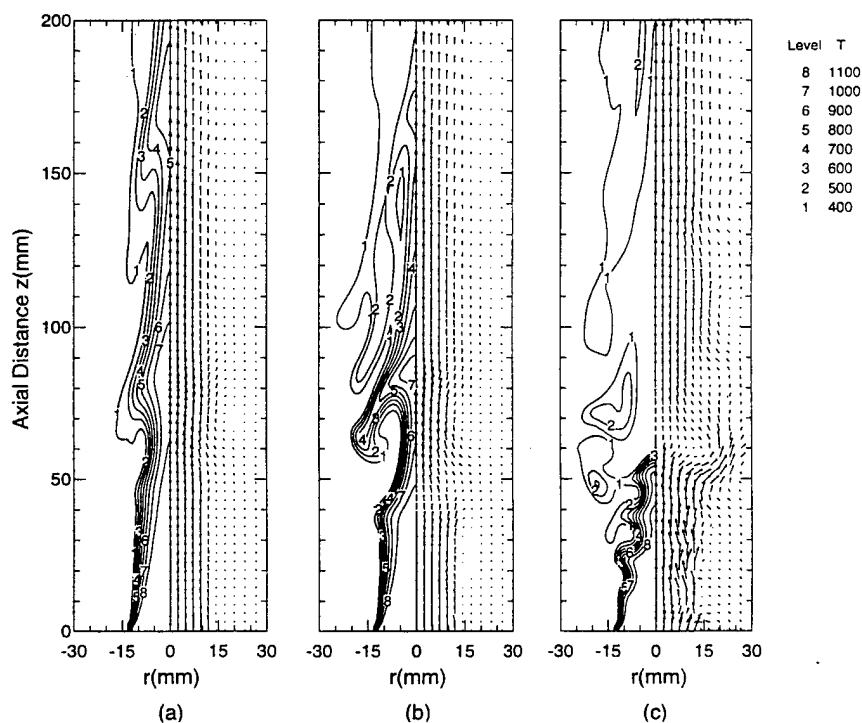


Fig. 13. Simultaneous snapshots of iso-temperature contours and velocity vectors for an evaporating spray for three different initial droplet diameters: (a) $d_o = 200 \mu\text{m}$, (b) $d_o = 100 \mu\text{m}$ and (c) $d_o = 50 \mu\text{m}$.

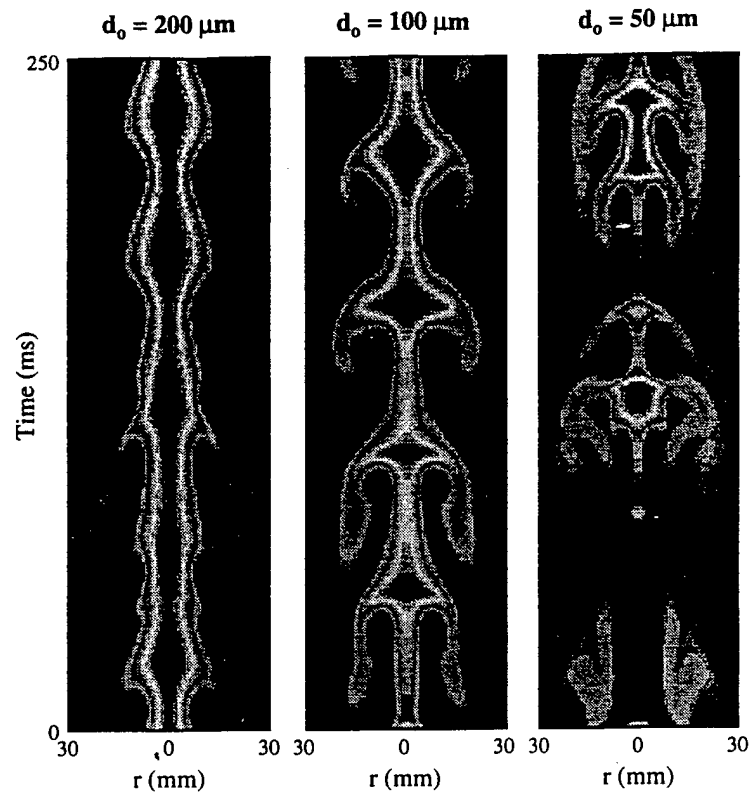


Fig. 14. Time evolution of temperature contours at a location of 7.5 cm above the inlet for the cases of Fig. 12.

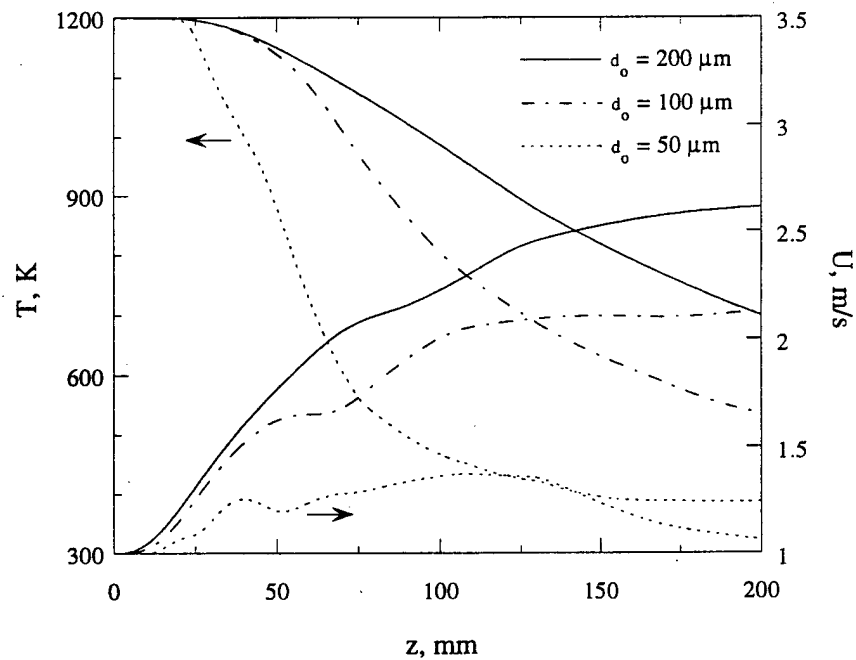


Fig. 15. Time-averaged axial profiles of gas temperature and axial velocity for an evaporating spray with three different initial droplet diameters and $M = 1.0$.

two-way nonlinear interactions seem to become stronger due to fast vaporization of 50- μm spray.

CONCLUSIONS

In this paper, we have investigated the dynamics of two-way droplet-vortex interactions and their influence on the structure of an evaporating spray. A low-speed spray formed (jet Reynolds number based on a jet temperature of 1200 K and velocity of 1.0 m s^{-1} is 154) between a droplet-laden heated nitrogen jet and a coflowing air stream has been simulated. Gravity has been used to generate large-scale vortical structures in the jet shear layer. The density difference between the heated fluid and the cold coflowing fluid gives rise to buoyant acceleration causing vortical structures to appear without any external perturbation. Liquid fuel (n-heptane) droplets are introduced into the vortex structures, and processes of droplet-vortex interactions are studied numerically by developing a time-accurate, multidimensional, two-phase algorithm. The effect of dispersed phase is incorporated through the source/sink terms in the gas-phase governing equations, representing the exchange of mass, momentum, and energy between the gas and liquid phases.

Snapshots and time evolution plots of vortex structures have been employed to analyze the effect of dispersed phase on their dynamics and time-averaged behavior under different mass loadings for both non-evaporating and evaporating sprays. The vortex structures cause droplets to disperse radially outward, and this in turn determines the fuel vapor distribution and also modifies the vortex dynamics. Thus, the dynamics and structural characteristics of the evaporating spray are strongly influenced by these interactions. The effects of initial droplet size, injection location, and liquid-to-gas mass loading ratio on the droplet-vortex interaction have been investigated by performing numerical experiments.

For both non-evaporating and evaporating sprays, the effect of dispersed phase on vortex dynamics is found to be negligible for mass loading ratio (M) less than 0.5. However, at higher loading ratios, depending upon the droplet injection characteristics, the vortex dynamics as well as the spray jet behavior may be strongly influenced by the dispersed phase. For a non-evaporating spray, the dispersed phase modifies the dynamics of vortex structures but not the time-average behavior, while it modifies both the dynamics and time-averaged behavior for an evaporating spray. For example, for 200- μm spray at $M = 1.0$ and with droplets injected into the shear layer, the vortex passage frequency is increased by about 30% and the vortex structures become weaker and less coherent compared to the gaseous jet case. This has important implications in spray applications such as gas turbine and ramjet combustors, especially when the system performance is strongly linked to some underlying unsteady phenomenon. Results also indicate that the initial droplet size has a strong influence on the two-

way interactions. Due to spray vaporization, gas temperature in the jet interior decreases, which modifies the vortex dynamics and consequently the droplet dynamics and vaporization. In fact, for 50- μm spray at $M = 1.0$, the vortex dynamics is drastically modified and a vortex pairing phenomenon is observed. The latter results in a much larger entrainment of colder fluid causing a subsequent destruction of vortex structures. Thus the spray injection characteristics have strong influence on the processes of droplet-vortex interactions.

Acknowledgements—This work was funded by the AFOSR under Grant F49620-93-1-0400 monitored by Dr Julian M. Tishkoff. Many fruitful discussions with Dr W. M. Roquemore at Wright-Patterson Air Force Base are greatly appreciated. Computations were performed on Cray C-90 at the Pittsburgh Supercomputing Center.

REFERENCES

1. G. L. Brown and A. Roshko, Density effects and large scales in the developing mixing layer. *J. Fluid Mech.* **64**, 775–816 (1974).
2. A. J. Yule, Large scale structure in the mixing layer of a round jet. *J. Fluid Mech.* **89**, 413–432 (1978).
3. V. R. Katta, L. P. Goss and W. M. Roquemore, Effect of nonunity Lewis number and finite-rate chemistry on the dynamics of a hydrogen-air jet diffusion flame. *Combust. Flame* **96**, 60–74 (1994).
4. E. K. Longmire and J. K. Eaton, Structure of a particle-laden round jet. *J. Fluid Mech.* **236**, 217–257 (1992).
5. J. N. Chung and T. R. Troutt, Simulation of particle dispersion in an axisymmetric jet. *J. Fluid Mech.* **186**, 199–222 (1988).
6. D. Hansell, I. M. Kennedy and W. Kollmann, A simulation of particle dispersion in a turbulent jet. *Int. J. Multiphase Flow* **18**, 559–576 (1992).
7. B. J. Lazaro and J. C. Lasheras, Particle dispersion in the developing free shear layer—I. Unforced flow. *J. Fluid Mech.* **235**, 143–178 (1992).
8. B. J. Lazaro and J. C. Lasheras, Particle dispersion in the developing free shear layer—II. Forced flow. *J. Fluid Mech.* **235**, 179–221 (1992).
9. M. Samimy and S. K. Lele, Motion of particles with inertia in a compressible free layer. *Phys. Fluids* **A3**, 1915–1923 (1991).
10. K. Hishida, A. Ando and M. Maeda, Experiments on particle dispersion in a turbulent mixing layer. *Int. J. Multiphase Flow* **18**, 181–194 (1992).
11. J. Uthuppan, S. K. Aggarwal, F. F. Grinstein and K. Kailasanath, Particle dispersion in a transitional axisymmetric jet: a numerical simulation. *AIAA J.* **32**, 2004–2014 (1994).
12. S. K. Aggarwal, Relationship between stokes number and intrinsic frequencies in particle laden flows. *AIAA J.* **32**, 1322–1325 (1994).
13. T. W. Park, S. K. Aggarwal and V. R. Katta, Gravity effects on the dynamics of evaporating droplets in a heated jet. *AIAA J. Propulsion Power* **11**, 519–528 (1995).
14. B. Abramzon and W. A. Sirignano, Droplet vaporization model for spray combustion calculations. *Int. J. Heat Mass Transfer* **32**, 1605–1618 (1989).
15. D. K. Edwards, V. E. Denny and A. F. Mills, *Transfer Processes: An Introduction to Diffusion, Convection and Radiation* (2nd Edn). McGraw-Hill, New York (1979).
16. S. K. Aggarwal, A. Tong and W. A. Sirignano, A comparison of vaporization models for spray calculation. *AIAA J.* **22**, 1448–1457 (1984).
17. B. P. Leonard, A stable and accurate convective mod-

- elling procedure based on quadratic upstream interpolation, *Comput. Meth. Appl. Mech. Engng* **19**, 59-98 (1979).
18. D. B. Spalding, A novel finite difference formulation for difference expressions involving both first and second derivatives, *Int. J. Numer. Meth. Engng* **4**, 551-559 (1972).
 19. P. A. Monkewitz and K. D. Sohn, Absolute instability in hot jets, *AIAA J.* **26**, (8), 911-916 (1988).
 20. S. Ragu and P. A. Monkewitz, The bifurcation of a hot round jet to limit-cycle oscillations, *Phys. Fluids A* **3**, 501-503 (1991).
 21. L.-D. Chen, J. P. Seaba, W. M. Roquemore and L. P. Gross, Buoyant diffusion flames, *Proceedings Twenty-Second International Symposium on Combustion*, pp. 677-684. The Combustion Institute, Pittsburgh, PA (1988).
 22. H. Eickhoff and A. Winandy, Visualization of vortex formation in jet diffusion flames, *Combust. Flame* **60** (1), 99-101 (1985).
 23. T. Yuan, D. Durox and E. Villermaux, An analog study for flame flickering, *Expts Fluids* **17** (5), 337-349 (1994).
 24. R. W. Davis, E. F. Moore, W. M. Roquemore, L.-D. Chen, V. Vilimpoc and L. P. Goss, Preliminary results of a numerical-experimental study of the dynamic structure of a buoyant jet diffusion flame, *Combust. Flame* **83** (3/4), 263-270 (1991).
 25. V. R. Katta, L. P. Goss and W. M. Roquemore, Numerical investigations of transitional H_2/N_2 jet diffusion flames, *AIAA J.* **32**, 84-94 (1994).

Unsteady Spray Behavior in a Heated Jet Shear Layer: Droplet-Vortex Interactions

S. K. AGGARWAL, T. W. PARK and V. R. KATTA *Department of Mechanical Engineering University of Illinois at Chicago, Chicago, IL 60607*
Innovative Scientific Solutions, Inc. Dayton, OH 45430

(Received March 1, 1996)

Abstract—Processes of droplet-vortex interactions have been studied numerically in a dynamic evaporating spray. The spray is formed between a droplet-laden heated nitrogen jet and a coflowing air stream. The jet velocity and temperature have been considered in a range, where large-scale vortex structures develop due to convective Kelvin-Helmholtz instability of the jet shear layer. Numerical simulations of the heated jet without droplets show the presence of organized vortex structures and their pairing interaction. The fundamental frequency of these structures scale with the jet diameter and velocity, yielding a Strouhal number of 0.36. Results concerning droplet dispersion indicate that 1) the dispersion of intermediate-sized droplets is enhanced due to their interaction with vortex rings during the vortex-pairing process, 2) a second Stokes number based on a droplet transit time can be used to characterize the dispersion of larger droplets, and 3) the evaporation during droplet-vortex interaction modifies dispersion significantly.

Results on the dynamics of two-way coupled system indicate that for a non-evaporating spray at a mass loading of unity, the dynamics of shear layer and vortex rings are strongly influenced by the dispersed phase. The locations of shear-layer rollup, vortex formation and pairing are shifted downstream, and their respective frequencies are reduced compared to those for the one-way coupled system. In addition, it is demonstrated that the shear-layer stability can be modulated by changing the droplet injection characteristics. For an evaporating spray, the effect of two-way coupling is more complex compared to that for a non-evaporating spray. In general, the shear-layer dynamics becomes much less organized compared to the one-way coupled system.

INTRODUCTION

Large-scale, coherent vortical structures have been found to exist in a variety of shear flows including those involving combustion (Katta *et al.* 1994) and multi-phase flows (Chung and Trout 1988; Longmire and Eaton 1992). In two-phase shear flows involving solid particles or liquid droplets, the transient interactions between dispersed phase and large vortical structures are expected to play a central role in determining the dynamics and structural characteristics of these flows. These transient interactions are strongly coupled and non-linear, and pertain to the effect of large vortical structures on droplet dispersion and gasification; which, in turn, affect the local environment near each droplet and thereby the dynamics of two-phase system under consideration. In reacting sprays, the flame dynamics and pollutant formation are expected to be strongly influenced by these interactions. A fundamental understanding of such interactions is also relevant for devising passive and active control strategies for improving the combustor performance. Many recent studies,

both numerical (Chung and Trout 1988; Uthuppan *et al.* 1994) and experimental (Longmire and Eaton 1992; Lazaro and Lasheras 1992; Hishida *et al.* 1992), have focussed on one-way coupling, characterizing the effect of vortex structures on droplet dispersion. The two-way coupling or the effects of dispersed phase on vortex dynamics, and subsequently on fuel vapor distribution and flame behavior, remain largely unexplored. In addition, the role of droplet vaporization in the dispersion process has not been investigated in previous studies.

In this paper, we report a numerical study of two-way droplet-vortex interactions in a dynamic evaporating spray. The spray is formed between a droplet-laden heated nitrogen jet and a coflowing air stream. The overall objective is to study the fundamental processes of spray diffusion flames in laminar and transitional regimes in the presence of large vortical structures. In the present study, however, the physical model is simplified by considering a heated jet issuing into a coflowing air stream, so that the complexities due to chemical reactions can be avoided. The jet velocity and temperature are considered in a range, where large-scale vortex structures develop due to convective Kelvin-Helmholtz instability of the jet shear layer (Huerre and Monkewitz 1985). In a separate study (Park 1996), we investigated the interactions of droplets with buoyancy-induced vortex structures resulting from a global instability. The dynamics of vortex structures and droplet-vortex interactions in a convectively unstable shear flow are significantly different from those associated with global instability, and are examined in the present paper. In the first part, the dispersion behavior of both non-evaporating and evaporating droplets is investigated. The objective is to examine the effect of droplet evaporation on the dispersion process. Several previous studies cited above have shown that the presence of large-scale vortex structures leads to a size-dependent dispersion behavior, such that the droplets with a response time on the order of a relevant vortex time exhibit the maximum dispersion. In many applications, especially those involving spray combustion, the size of a droplet may change significantly during its interaction with a vortex, i.e. the droplet lifetime may be of the same order of magnitude as the droplet-vortex interaction time. It is therefore relevant to investigate the effect of size change on droplet dispersion. In the second part of this study, we examine the processes of two-way interactions for both non-evaporating and evaporating droplets, and make an attempt to gain an understanding of the effects caused by momentum coupling as well as mass and energy coupling between the phases.

THE PHYSICAL-NUMERICAL MODEL

The physical system simulated in the present study is shown schematically in Figure 1. It consists of a central jet which is a two-phase mixture of gaseous nitrogen and liquid fuel (*n*-heptane) droplets and a low-speed annular air flow. The jet at a velocity of 5.0 m/s and temperature of 1200 K is issuing into a coflow which is at velocity of 0.2 m/s and temperature of 294 K. The central jet is heated primarily to enhance the fuel evaporation. The jet diameter (D) is 2.54 cm. The Reynolds number based on velocity, density and viscosity of the heated jet is 790, and the Richardson number, $Ri = gD(\rho_0 - \rho_j)/(U_j^2 \cdot \rho_j)$, is 0.031. Here U_j and ρ_j are the jet velocity and

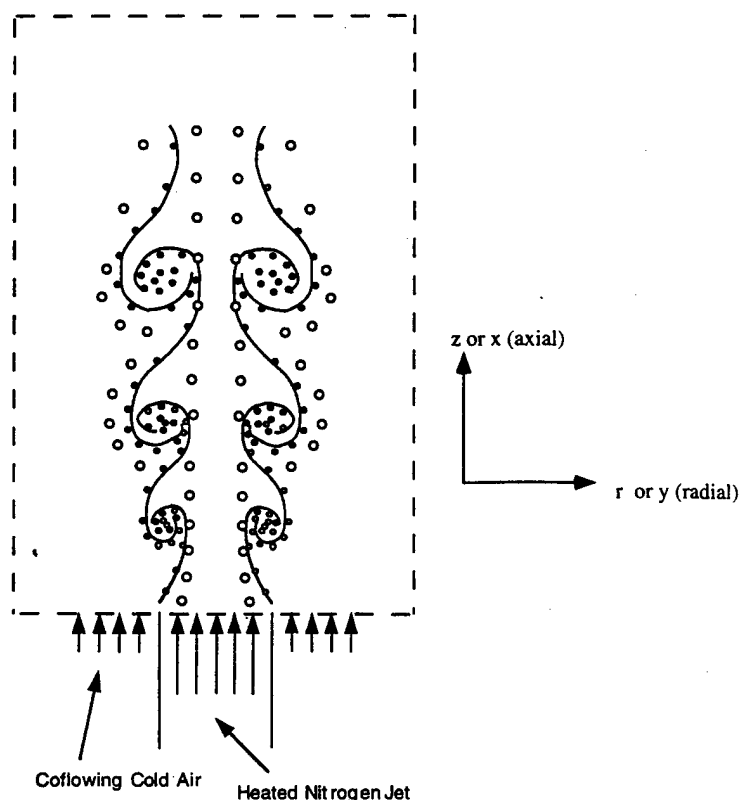


FIGURE 1 A schematic of droplet-laden heated nitrogen jet in a cold annular air flow.

density, ρ_0 the ambient density, and g the gravitational acceleration. Note that a small Richardson number $Ri = 0.031$ implies that the effect of buoyant convection is small compared to the inertial acceleration, and jet-shear-layer instability is primarily of the Kelvin-Helmholtz type. The numerical model is based on the solution of time-dependent, two-phase equations in an axisymmetric geometry. The unsteady, axisymmetric governing equations in cylindrical (z, r) coordinate system for a droplet-laden heated jet are

$$\frac{\partial(\rho\Phi)}{\partial t} + \frac{\partial(\rho u\Phi)}{\partial z} + \frac{\partial(\rho v\Phi)}{\partial r} = \frac{\partial}{\partial z} \left(\Gamma^\Phi \frac{\partial\Phi}{\partial z} \right) + \frac{\partial}{\partial r} \left(\Gamma^\Phi \frac{\partial\Phi}{\partial r} \right) - \frac{\rho v\Phi}{r} + \frac{\Gamma^\Phi}{r} \frac{\partial\Phi}{\partial r} + S_g^\Phi + S_r^\Phi. \quad (1)$$

The general form of Eq. (1) represents the continuity, momentum, species, or energy conservation equation depending on the variable used for Φ . Table I gives the transport coefficients Γ^Φ and the source terms S_g^Φ and S_r^Φ that appear in the governing equations. In this table, μ , λ , and C_p represent the viscosity, the thermal conductivity, and the specific heat, respectively. They are considered functions of temperature and species concentration.

TABLE I

Transport coefficients and source terms appearing in governing equations

Equations	Φ	Γ_g^Φ	S_g^Φ	S_l^Φ
Continuity	1	0	0	$\sum_k n_k \dot{m}_k$
Axial momentum	u	μ	$-\frac{\partial p}{\partial z} + (\rho_0 - \rho)g + \frac{\partial}{\partial z} \left(\mu \frac{\partial u}{\partial z} \right) + \frac{\partial}{\partial r} \left(\mu \frac{\partial v}{\partial z} \right) \frac{\mu}{r} \frac{\partial v}{\partial z}$ $-\frac{2}{3} \left\{ \frac{\partial}{\partial z} \left(\mu \frac{\partial u}{\partial z} \right) + \frac{\partial}{\partial z} \left(\mu \frac{\partial v}{\partial r} \right) + \frac{\partial}{\partial z} \left(\mu \frac{v}{r} \right) \right\}$	$\sum_k \left(n_k \dot{m}_k u_k - n_k M_k \frac{du_k}{dt} \right)$
Radial momentum	v	μ	$-\frac{\partial p}{\partial r} + \frac{\partial}{\partial z} \left(\mu \frac{\partial u}{\partial r} \right) + \frac{\partial}{\partial r} \left(\mu \frac{\partial v}{\partial r} \right) + \frac{\mu}{r} \frac{\partial v}{\partial r} - 2\mu \frac{v}{r^2}$ $-\frac{2}{3} \left\{ \frac{\partial}{\partial r} \left(\mu \frac{\partial u}{\partial z} \right) + \frac{\partial}{\partial r} \left(\mu \frac{\partial v}{\partial r} \right) + \frac{\partial}{\partial r} \left(\mu \frac{v}{r} \right) \right\}$	$\sum_k \left(n_k \dot{m}_k v_k - n_k M_k \frac{dv_k}{dt} \right)$
Mass fraction of fuel	Y_f	ρD_f	0	$\sum_k n_k \dot{m}_k$
Mass fraction	Y_o	ρD_o	0	0
Energy	T	λ/C_p	0	$\sum_k n_k \dot{m}_k (h_{fs} - \ell_{k,eff})$

The effect of dispersed phase on gas-phase properties is incorporated through the source/sink terms (S_g^Φ) representing the exchange of mass, momentum, and energy between the gas and liquid phases. In order to evaluate these terms, it is necessary to establish droplet trajectories, size and temperature histories. The Lagrangian approach is employed to solve the liquid-phase governing equations for the dynamics and vaporization history of each droplet group. The spray is characterized by a discrete number of droplet groups, distinguished by their injection location, initial size, and time of injection. A droplet group in a Lagrangian treatment represent a characteristic group containing a finite number of droplets. Since an axisymmetric configuration is analyzed, the liquid properties are implicitly averaged in the azimuthal direction and the number of droplets associated with each characteristic group represents droplets uniformly distributed in an annular ring. The equations governing the variation of position, velocity, and size for each droplet group and other expressions are provided in an earlier paper (Park *et al.* 1995). A comprehensive vaporization model is employed to calculate the instantaneous droplet size and surface temperature along the trajectory of each group. The model includes the effects of variable thermophysical properties, non-unity Lewis number in the gas film outside the droplet, the effect of Stefan flow on the heat and mass transfer between the droplet and the gas, and the effect of transient liquid heating. The variable thermophysical properties are calculated at reference film temperature and concentrations, obtained by using the 1/3 rule, except for the gas density which is calculated at the free stream value (Abramzon and Sirignano 1989). The Wilke rule

(Edwards *et al.* 1979) is used to calculate the dynamic viscosity and thermal conductivity of the gas film. The liquid fuel ($n\text{-C}_7\text{H}_{16}$) properties are collected from various sources and approximated as a function of the temperature (Park *et al.* 1995). The effect of transient liquid heating is incorporated by using the finite-conductivity model (Aggarwal 1984).

An implicit algorithm is employed to solve the unsteady gas-phase equations. The governing equations are integrated by using a "finite control volume" approach with a staggered, non-uniform grid system. The finite-difference forms of the momentum, energy, and species-densities equations are obtained using an implicit QUICKEST scheme (Leonard 1979). An iterative ADI (Alternative Direction Implicit) technique is used for solving the resulting sets of algebraic equations. At every time step, the pressure field is calculated by solving the pressure Poisson equations at all grid points simultaneously and utilizing the LU (Lower and Upper diagonal) matrix decomposition technique. Grid lines are clustered near the shear layer to resolve the steep gradients of the dependent variables. Boundaries of the computational domain are shifted sufficiently to minimize the propagation of disturbances into region of interest. The computational domain in the radial and axial directions is 15 cm and 40 cm respectively. Thus, the boundary in the radial direction is 5.9 nozzle diameters away from the axis of symmetry and the out-flow boundary in the axial direction is 15.7 nozzle diameters away from the nozzle exit. In our earlier studies it was found that these distances are more than sufficient to avoid the boundary influences on the region of interest (2 and 7 nozzle diameters in the radial and axial directions, respectively). The flow variables at the outflow boundary are obtained using an extrapolation procedure with weighted zero and first-order terms. The main criterion used in selecting the weighting functions is that the vortices crossing this outflow boundary should leave smoothly without being distorted.

The liquid-phase equations governing the position, velocity, and size of each droplet are advanced in time by a second-order accurate Runge-Kutta method. Since the gas-phase solution employs an implicit procedure, the temporal step size used for integrating the liquid-phase equations is usually smaller than that for gas-phase equations. An automatic procedure is implemented in order to select an optimum liquid-phase time step. The procedure to advance the two-phase solution over one gas-phase time step is as follows. Using the known gas-phase properties, the liquid-phase equations are solved over a specified number of liquid-phase subcycles. A third-order accurate Lagrangian polynomial method is used for interpolating the gas-phase properties from the non-uniform fixed grid to the droplet characteristic location. It should be noted that the interpolation scheme for the gas-phase velocities u and v is based on their respective grid cells because of the use of a staggered grid in gas-phase calculation. The droplet properties are updated after every liquid-phase subcycle. Also, during each subcycle, the liquid-phase source terms appearing in the gas-phase equations are calculated at the characteristic location, and then distributed to the surrounding gas-phase grid points. These source terms are added at each gas-phase grid points during one gas-phase time step and then used in the implicit solution of the gas-phase equations. Additional details can be found in an earlier paper (Park *et al.* 1995).

RESULTS

The dynamics of heated jet was first studied under normal-gravity and zero-gravity conditions without injecting droplets in the flow. The objective was to assess if gravity had any influence on the jet instability for the low Richardson number ($Ri = 0.031$) condition used in this, paper. Numerical experiments were also performed to validate the numerical model and examine the stability characteristics of the jet shear layer.

Numerical validation studies employed three different grids, namely 151×61 , 201×71 , and 301×91 , and three different temporal step sizes corresponding to CFL numbers of 0.1, 0.2 and 0.4. Note that CFL (Courant-Friedrichs-Lewis) number is merely used here to control the temporal step size, and does not imply any significance pertaining to numerical stability. In all the cases, a non-uniform grid was employed with grid lines clustered near the shear layer to resolve the steep gradients of the dependent variables. This implies that the additional grid points in the 201×71 grid are placed near the shear layer, thus effectively reducing the grid density for the 201×71 grid by about fifty percent compared to the 151×61 grid. Results for the two different grid sizes and two CFL numbers are presented by plotting the time-history of axial velocity in the shear layer. Figure 2 indicates that the results are reasonably independent of the grid size and temporal step size used in the simulations. Figures 2a and 2c indicate the presence of well-organized, periodic Kelvin-Helmholtz vortex rings, while Figure 2b indicates the occurrence of a vortex-pairing interaction. The spatial development of vortex rings and their pairing interaction are depicted in Figure 3, which shows the instantaneous iso-temperature contours in the jet shear layer under normal- and zero-gravity conditions. Toroidal vortex rings roll up periodically downstream of the nozzle exit due to the Kelvin-Helmholtz instability. No artificial (external) excitation is used to generate these vortices and it is believed that the noise in the calculations is providing the needed perturbation in the shear layer. It is interesting to note that even at a low Richardson number of 0.031, the vortex structures are influenced by gravity. However, the effect is small, and can be attributed to the buoyant acceleration of the low-speed annular fluid as it gets heated in the jet thermal layer. Moreover, the shear-layer rollup and large-scale vortex dynamics are essentially governed by the Kelvin-Helmholtz instability. For example, the dominant frequencies corresponding to shear layer rollup and vortex-pairing interaction remain the same whether gravity is included in the simulations or not.

Figure 3 indicates a pairing interaction starting at an axial location $z = 40$ mm as the vortices convect downstream. The dominant frequencies obtained from the fast Fourier transform of axial velocity are 70 and 35 Hz corresponding to the roll up and merging frequencies respectively. Assuming the initial momentum thickness of jet shear layer between one to two radial grid spacing, we obtain the instability Strouhal number between 0.0112–0.0224, a range which encompasses the experimental range 0.0125–0.0155 reported in the literature (Hussain and Hussain 1983). Also, according to the experimental study of Subbarao and Cantwell (1992), the jet instability frequency scales with the inertial time scale at small Ri . This yields a Strouhal number of 0.36 in the present case, which also agrees with the reported

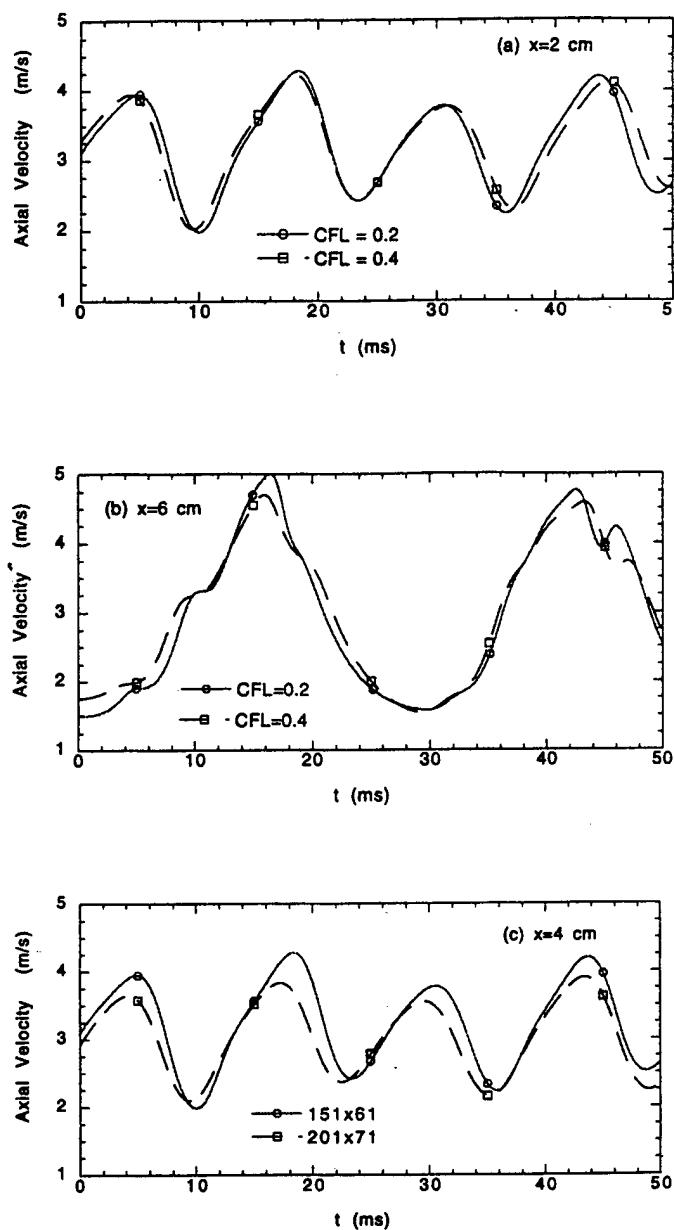


FIGURE 2 Time-history plot of axial velocity in the jet shear layer at three axial locations ((a) $x = 2$ cm, (b) $x = 6$ cm, and (c) $x = 4$ cm); effects of temporal step size and grid size.

experimental range of 0.25–0.5. The spectral analysis also indicates that the amplitude of subharmonic frequency (35 Hz) peaks at $x = 80$ mm, implying the occurrence of vortex merging at this location. This is confirmed by the iso-temperature plots in Figure 3.

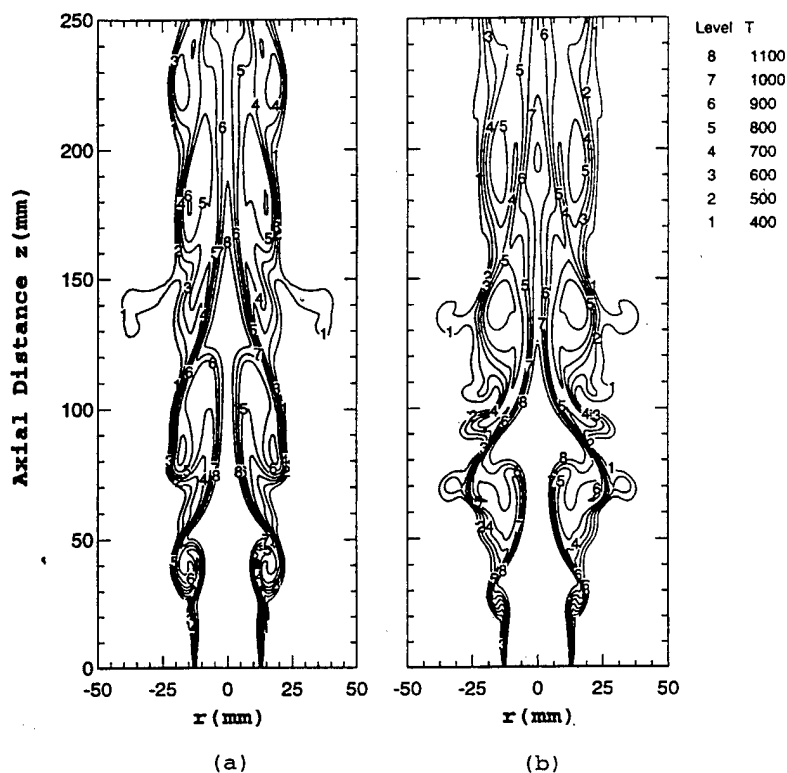


FIGURE 3 Instantaneous temperature contours for the heated nitrogen jet at (a) normal gravity and (b) zero gravity.

ONE-WAY INTERACTIONS

Results depicting the effect of large-scale structures on the dispersion of non-evaporating and evaporating droplets are summarized in Figure 4. For these results, the source terms S_j^ϕ representing the effects of dispersed phase on the gas phase (see Table I.) are identically set to zero. The instantaneous iso-temperature contours and droplet locations are plotted for both non-evaporating and evaporating droplets for four different droplet sizes. The red color in iso-temperature contours corresponds to a temperature of 1200 K while the purple corresponds to a value of 294 K, representing the temperature of coflowing stream. In order to examine the effect of vortex rings on droplet dispersion, instantaneous locations of non-evaporating and evaporating droplets are plotted on the left-hand and right-hand sides of the symmetric jet, respectively. Color representing the size of the droplet changes from red to blue as it evaporates from the initial size (at the instant of injection) to the size of a gas particle, which is taken as 10 μm or one-tenth of the initial size whichever is smaller. Since the droplets on the right-hand side of the jet represent non-evaporating ones, the color of the droplets remains red. Quantitative results on dispersion for both non-evaporating and evaporating droplets are depicted in Figure 5, which

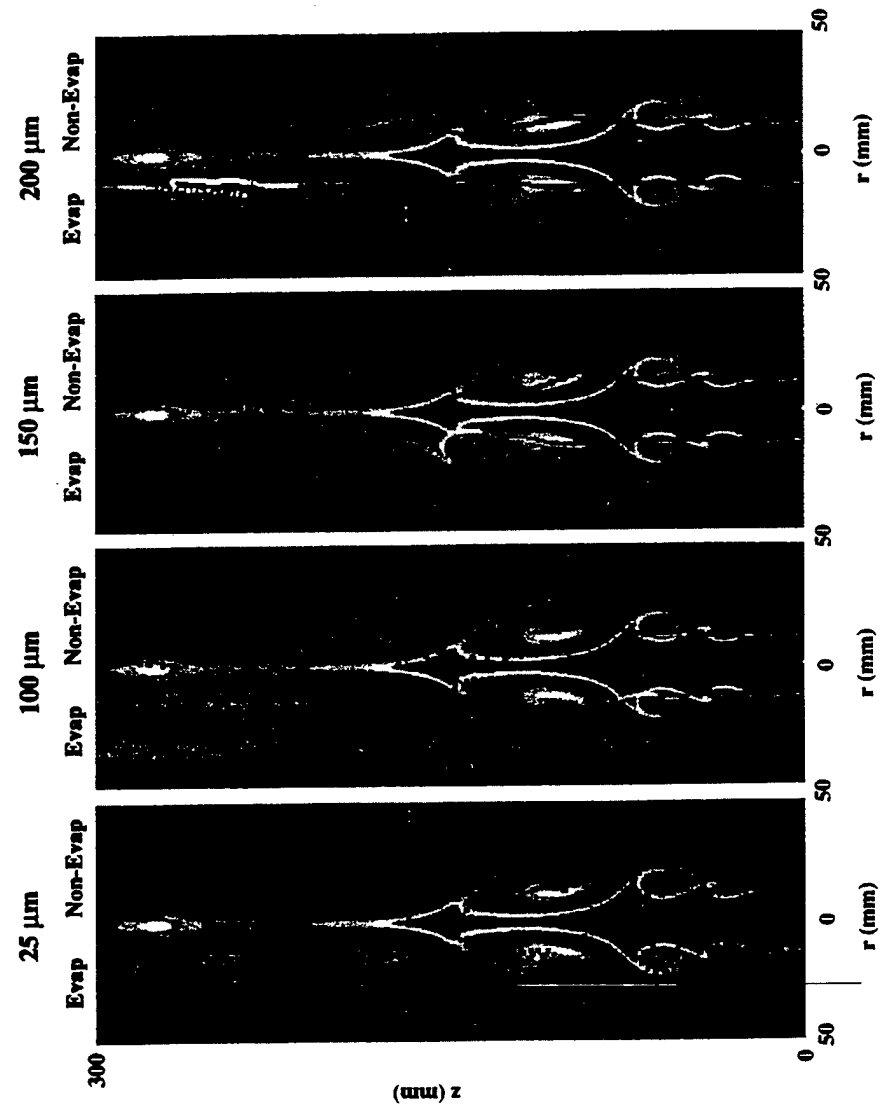


FIGURE 4. Simultaneous snapshots of the flow (iso-temperature contours) and droplets (solid squares) of different sizes; in each individual snapshot locations of the evaporating and non-evaporating droplets are plotted on the left-hand and right-hand sides of the symmetric jet, respectively. For iso-temperature contours, the red and purple colors represent the highest (1200 K) and the lowest (294 K) temperatures respectively. see COLOR PLATE XI.

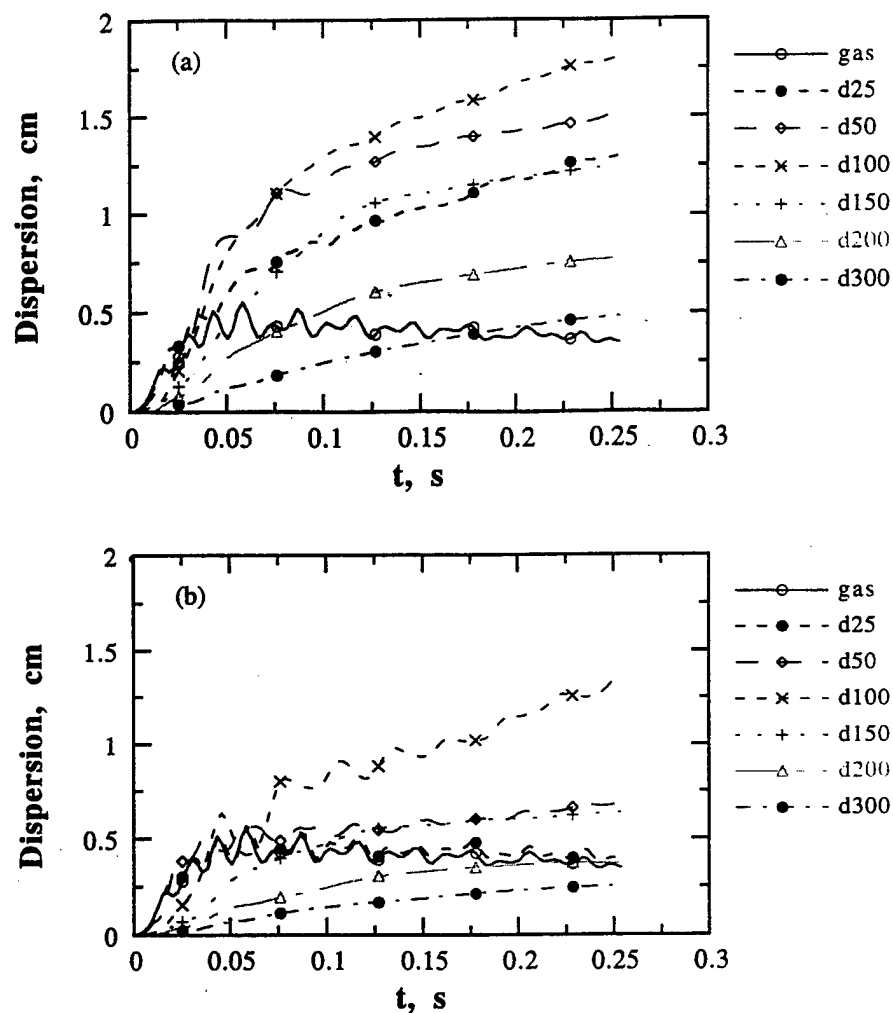


FIGURE 5 Dispersion function plotted as a function of time for (a) non-evaporating, and (b) evaporating droplets injected at a radial location of 1.27 cm.

shows the variation of dispersion function with time for different-size droplets. The dispersion function is defined as the rms (root mean squared) lateral displacement of droplets from the initial radial injection location:

$$D(t, N) = \left[\frac{\sum_{i=1}^N (r_i(t) - r_{i0})^2}{N} \right]^{1/2} \quad (2)$$

where r_i the radial location of droplet i at time t , r_{i0} the radial injection location of the same droplet at nozzle exit, and N is the total number of droplets in the flow field at time t . Results in Figure 5 indicate a typical size-selective dispersion process

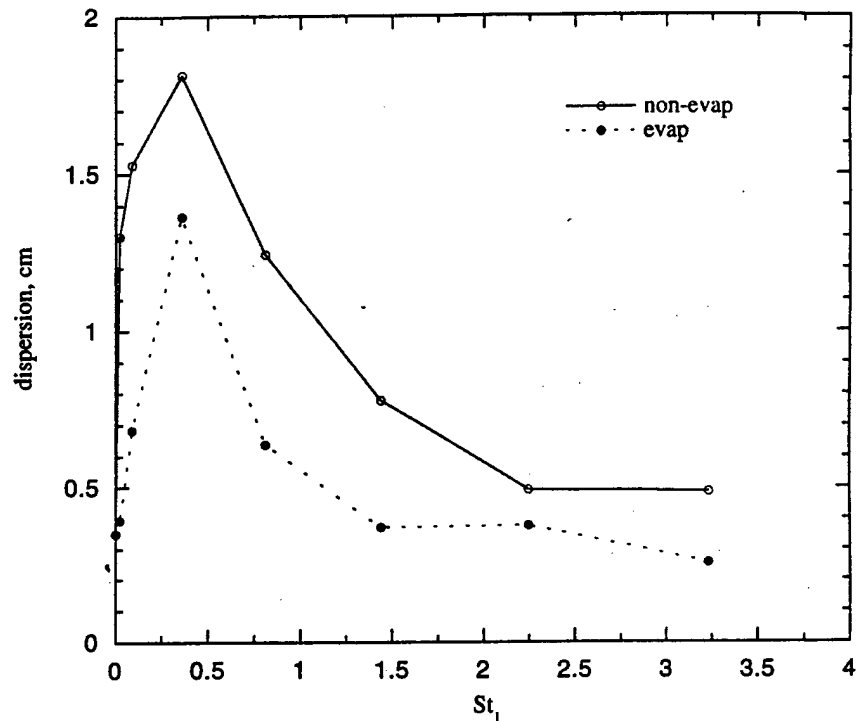


FIGURE 6 Dispersion function versus Stokes number for non-evaporating and evaporating droplets.

whereby the intermediate-sized droplets ($100\text{ }\mu\text{m}$ in the present study) exhibit the maximum dispersion. Since the effect of vortex structures on non-evaporating droplets is often characterized by the Stokes number defined as the ratio of droplet response time (t_p) to a characteristic flow time (t_f), we show the variation of dispersion function with Stokes number (St_1) for both non-evaporating and evaporating droplets in Figure 6. The value of t_f is based on the first subharmonic or vortex-merging frequency, since the detailed visualization of flow field and droplet locations indicates that droplet dispersion is influenced more strongly by the vortex-merging process.

Important observations from Figure 6 are that the dispersion of intermediate-sized droplets is enhanced due to their interaction with vortex rings, that the pairing interaction is most responsible for this dispersion enhancement, and that droplet evaporation during the transient droplet-vortex interaction modifies dispersion significantly. These observations can be explained by the instantaneous snapshots given in Figure 4. For the non-evaporating case, it can be seen that the intermediate-sized droplets exhibit higher dispersion, as these droplets are centrifuged out during the vortex-pairing interaction. The larger-sized droplets disperse less as their motion is not much affected by the pairing interaction. These droplets can be dispersed, however, by the merged vortices further downstream, provided their transit time is

comparable to their aerodynamic response time. For example, 150- μm and 200- μm droplets are dispersed following their interaction with the second (merged) and third vortex respectively. This suggests that droplet transit time may also be an important parameter in addition to the flow time, in characterizing the dispersion of larger droplets. Following Hardalupas *et al.* (1992), we define a second Stokes number (St_2) or a droplet transit Stokes number as the ratio of droplet transit time to its response time. Using this Stokes number, we are able to explain the dispersion of larger-sized droplets. The transit time for 150- μm droplets is 36 ms (based on a injection velocity of 5.0 m/s and second vortex location of 18 cm) yielding $St_2 = 0.64$. Similar calculation yields $St_2 = 0.86$ for 200- μm droplets.

Another important observation from Figures 4 and 6 is that the dispersion of evaporating and non-evaporating droplets in a dynamically evolving flow are quite different. Since the effect of vaporization is to reduce the droplet response time and thus reduce the Stokes number St_1 , one would expect that the plot of dispersion function versus St_1 should shift uniformly to the left of that for the non-evaporating case. However, the dynamic nature of droplet-vortex interaction alters this expected behavior. As noted earlier, small- and medium-sized non-evaporating droplets exhibit higher dispersion due to their interaction with vortex rings during the vortex-pairing process, while the dispersion of larger-sized droplets is due to their interaction with vortices after the pairing process. The evaporation during droplet-vortex interaction modifies this behavior significantly. The small- and medium-sized droplets vaporize completely prior to or during their interaction with vortex rings, and consequently their dispersion is similar to that of tracer particles. The larger-sized evaporating droplets on the other hand are not affected significantly by the pairing vortices. Their dispersion is determined by their interaction with vortices following the pairing interaction. Due to evaporation, however, their dispersion is reduced compared to that of non-evaporating droplets since the degree of centrifuging decreases with the decrease in droplet size. Consequently, the effect of vaporization is to reduce droplet dispersion over the entire droplet size range, as indicated in Figure 6.

TWO-WAY INTERACTIONS

Both non-evaporating and evaporating sprays are analyzed in order to distinguish the two-way interactions involving only momentum transfer between the phases from those involving mass, momentum, and energy transfer. Calculations are initially made without injecting droplets into the fuel stream. As discussed earlier, the shear layer between the 1200-K nitrogen jet and the cold annulus air flow becomes unsteady with the development of large-scale vortices. The gasphase simulation is started at $t = 0$, and the droplet injection is started at $t = 0.16$ s. During this time, the initial flow transients are convected out of the computational domain, and the vortex rings attained a periodic structure. Droplets are injected into the jet shear layer every $10\Delta t_{\text{gas}}$, where $\Delta t_{\text{gas}} = 0.03176$ ms, from a radial location of 1.25 cm. This time interval yields an average droplet spacing which is about 16 times the droplet diameter, and can be considered as sufficiently large so as to neglect interaction

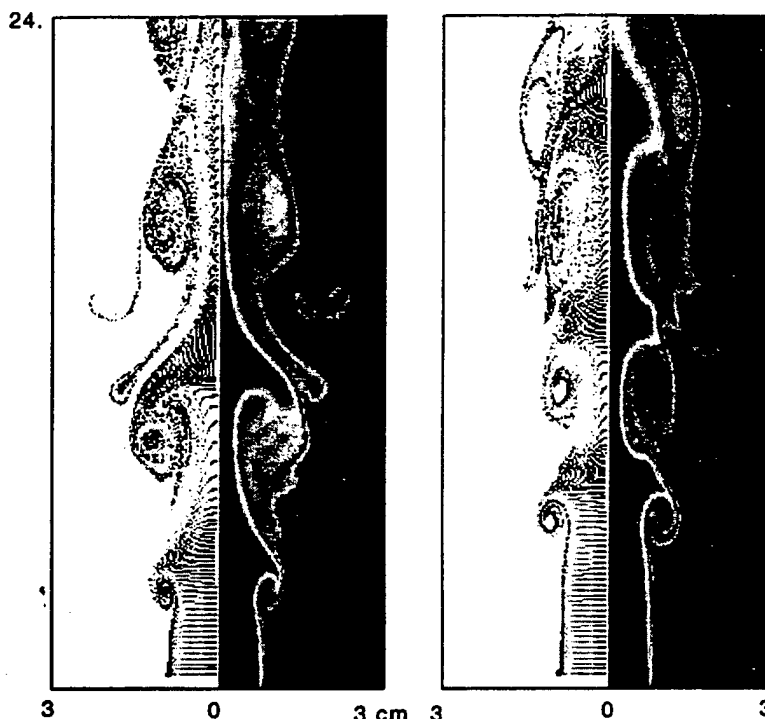


FIGURE 7 Snapshots of flow field for a non-evaporating spray with (a) one-way interaction, and (b) two-way interaction.

between the droplets. The number of droplets with each injection depends on the droplet mass loading (ratio of droplet mass flow rate to nitrogen mass flow rate in the jet), initial droplet size, and injection time interval. In the present study, a monodisperse *n*-heptane spray with an initial diameter of $d_p = 100 \mu\text{m}$ and mass loading of unity is considered. Note that $d_p = 100 \mu\text{m}$ corresponds to a Stokes number on the order of unity, and exhibits the maximum dispersion in the present case. It is also important to note that at a mass loading of unity, the volume occupied by liquid phase is about three orders of magnitude smaller than that of the gasphase volume, and the dilute-spray assumption is still valid. The initial diameter $d_p = 100 \mu\text{m}$ and mass loading of unity yields the number of droplets in each injection as 673, which is equivalent to having 673 equally distributed azimuthal injection locations.

Extensive flow visualization was used to gain a qualitative understanding of the effect of dispersed phase on large-scale vortex structures. One representative result is depicted in Figure 7, which compares snapshots of the flow field for a non-evaporating spray with one-way and two-way interactions respectively. In each snapshot, we plot instantaneous iso-temperature contours on the right, and streaklines on the left. Important observation is that the momentum coupling has a significant influence on

the dynamics of vortex structures. For the two-way coupled system, the locations of shear layer rollup and vortex pairing are shifted downstream compared to the one-way coupled system. More detailed flow visualization for the two cases indicated that for the two-way coupled system, the vortex structures are stronger, though less coherent, and entrain more lowspeed (colder) fluid compared to those for the one-way coupled system. We will discuss this aspect further when quantitative results are presented for the two-way coupled system.

Figure 8 shows simultaneous snapshots of the flow and droplets for three different cases; one-way coupled system in Figure 8b and two-way coupled evaporating and non-evaporating sprays in Figures. 8a and 8c respectively. For the non-evaporating case, due to the delayed vortex formation and pairing interaction, the occurrence of significant droplet dispersion is also moved farther downstream compared to the one-way coupled system. Figure 8 also indicates that the effect of dispersed phase on

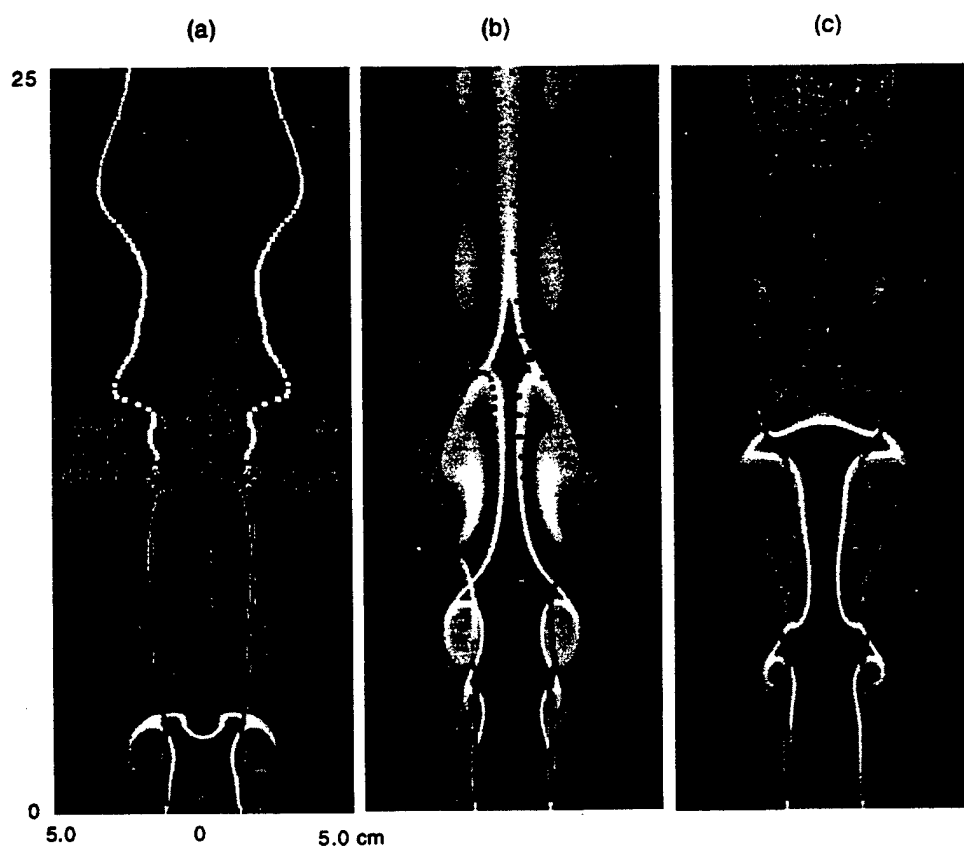


FIGURE 8 Simultaneous snapshots of the flow and droplets for (a) evaporating spray with two-way interaction, (b) spray with one-way interaction and (c) non-evaporating spray with two-way interaction. For iso-temperature contours, the red and purple colors represent the highest (1200 K) and the lowest (294 K) temperatures respectively. See COLOR PLATE XII.

the vortex structures is more significant for the evaporating case compared to the non-evaporating one. This can be attributed to the added effects of mass and energy transfer between the phases for the evaporating case. Based on a detailed visualization of the two-phase flow field for the evaporating case, the effect of dispersed phase on the temporally and spatially developing shear layer can be described as follows. As the droplets are injected into the shear layer, the rollup location initially shifts downstream from 3 cm to 5 cm, similar to the non-evaporating case. However, as the droplet evaporation becomes significant, the addition of fuel vapor with density three times that of nitrogen strongly affects the vortex formation process. In addition, the jet cooling caused by droplet heating and vaporization increases the mixture density, which further modifies shear layer dynamics. Due to these two effects, the rollup location moves upstream to about 2 cm from the nozzle exit, the vortex becomes stronger and pinches the jet more strongly compared to that for the one-way coupled system. The subsequent processes, which normally involves the convection of vortices and pairing interactions for the one-way coupled system, become much less organized for the evaporating case. In general, the pairing interactions are much less frequent and coherent, and the vortices are strongly stretched as they convect downstream. In addition, the shear layer rollup becomes less organized, with the rollup location oscillating between 2 and 5 cm from the nozzle exit.

The loss of coherency in shear layer dynamics for the two-way coupled system is better illustrated by plotting the time history of axial velocity for the three cases. As indicated in Figure 9, for the one-way coupled system, the processes of shear layer rollup and vortex formation are well organized with a frequency of 70 Hz. For the two-way coupled system, however, the shear layer dynamics is much less organized, especially for the evaporating spray. This is further indicated by the Fourier transform of axial velocity shown in Figure 10. With one-way interaction, both the shear layer rollup and the vortex pairing are highly organized with frequencies of 70 and 35 Hz respectively. For the non-evaporating spray with two-way momentum coupling, the rollup and vortex-pairing frequencies are reduced to 54 and 27 Hz respectively, and the vortices are not as organized as in the one-way coupled system. For the evaporating spray with two-way coupling, the dynamics represents a much less organized behavior without any well-defined frequency.

For the non-evaporating case discussed above, the two-way coupling modifies the shear layer dynamics such that the vortex formation and pairing occur at a downstream location, and their frequencies are reduced compared to those for the one-way coupled system. In order to examine the momentum-coupling effect further, we ran additional simulations and studied the effect of droplet injection velocity on the gas-phase dynamics. The time-averaged structure of the shear layer for different droplet injection velocities is depicted in Figure 11. The axial profiles of time-averaged gas-phase velocity indicate that the axial velocity is smaller for the two-way coupled system with $U_p = 5.0$ m/s (the base case discussed) compared to that for the one-way coupled system, indicating greater entrainment of the cold fluid. For this case, the droplets are injected at the jet velocity, i.e. the gas phase and droplets initially have the same velocity. However, as the shear layer develops spatially, the gas-phase velocity decreases in the shear layer. Since droplets now have higher velocity than the gas phase, there is momentum transfer from dispersed phase to gas

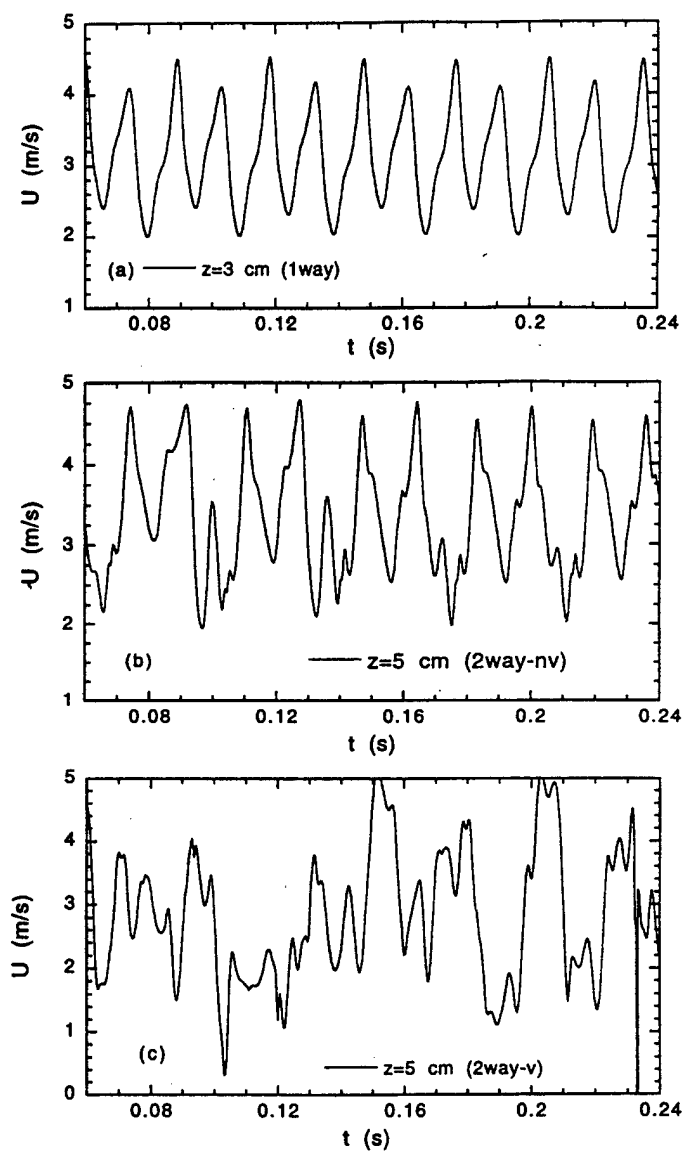


FIGURE 9 Time history of gas-phase axial velocity in the shear layer for (a) one-way interaction, (b) non-evaporating spray with two-way interaction, and (c) evaporating spray with two-way interaction.

phase, which is indicated by the fact that the gas-phase velocity is initially higher for the two-way coupled system with $U_p = 5.0$ m/s compared to that for the one-way coupled system, Figure 11a. This increases the magnitude of vorticity in the shear layer, and thus strengthens the vortex structures. However, if the droplets are injected at a velocity smaller than the jet velocity, the momentum transfer occurs in the reverse direction, reducing vorticity magnitude in the shear layer. Consequently, as

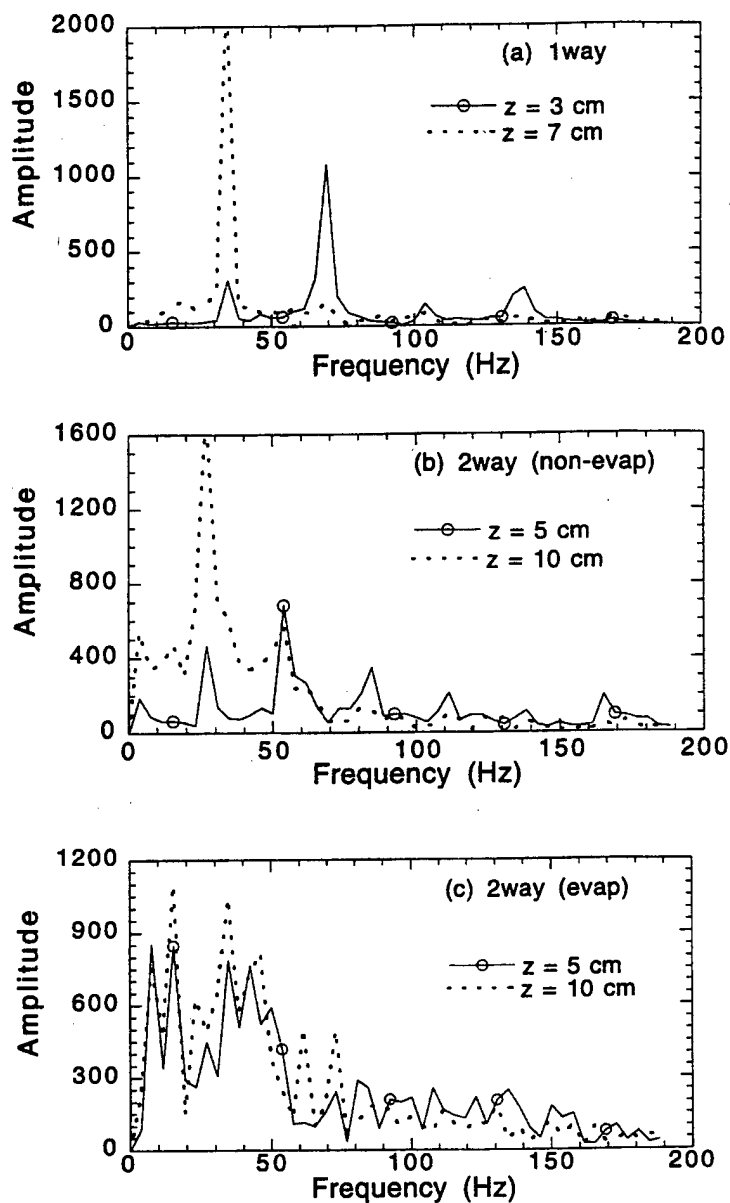


FIGURE 10 Frequency spectrum of axial gas velocity for (a) one-way interaction, (b) two-way non-evaporating spray, and (c) two-way evaporating spray.

the droplet injection velocity is decreased compared to the jet velocity, the shear layer stability is enhanced, and entrainment of the colder fluid is reduced. The axial profiles of gas-phase temperature shown in Figure 11b are consistent with those of gas-phase velocity. For the two-way case with $U_p = 5.0$ m/s, the gas temperature

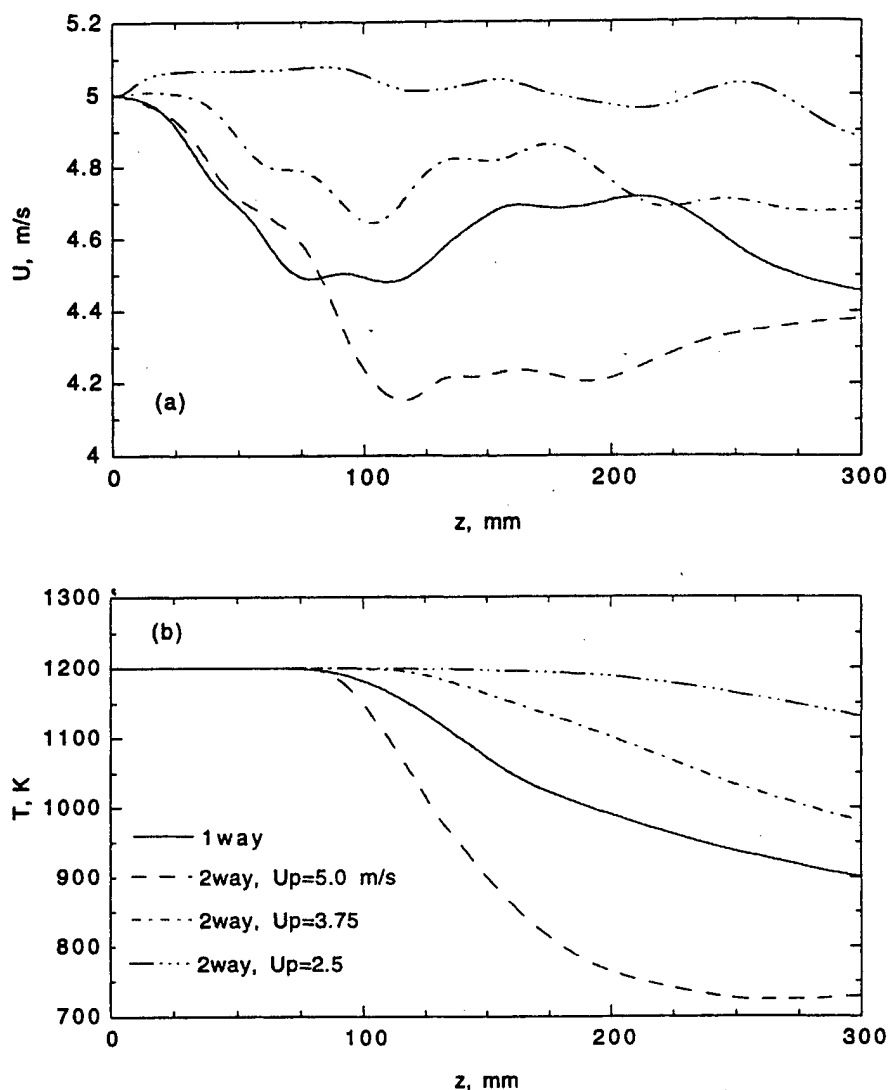


FIGURE 11 Axial profiles of time-averaged gas velocity and temperature for four different cases.

decreases faster compared to that for the one-way case, indicating greater entrainment of colder fluid in the shear layer for the former. However, as the droplet injection velocity is reduced, the shear layer becomes more stable, as indicated by a slower rate of decrease of gas temperature for $U_p = 3.75$ m/s and 2.5 m/s. The increased shear layer stability was also confirmed by employing detailed visualization of the temporally and spatially developing shear layer for different droplet injection velocities. Another confirmation is provided in Figure 12, which shows the

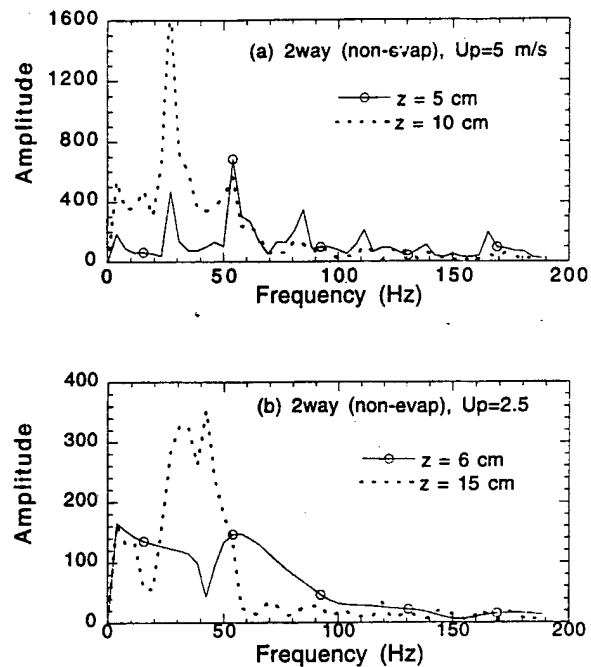


FIGURE 12 Frequency spectrum of axial gas velocity for a two-way coupled non-evaporating spray with (a) droplet injection velocity $U_p = 5.0$ m/s, and (b) $U_p = 2.5$ m/s.

Fourier spectrum of gas-phase axial velocity for two different droplet velocities. For $U_p = 2.5$ m/s, the shear layer stability is significantly enhanced with a formation of a weak vortex far downstream ($z = 15$ cm), as indicated by the significantly reduced amplitude and the absence of a dominant frequency for this case. Thus, the important observation is that at a liquid mass loading of unity, the dispersed phase has a strong effect on the stability and dynamic characteristic of jet shear layer, and this effect can be modulated by changing the droplet injection characteristics.

CONCLUSIONS

In this paper, we have investigated the effect of droplet evaporation on dispersion, and the dynamics of two-way droplet-vortex interactions and their influence on the structure of both non-evaporating and evaporating sprays. A spray formed between a droplet-laden heated nitrogen jet and a coflowing air stream has been simulated. The jet velocity and temperature have been considered in a range, where large-scale vortex structures develop due to the convective Kelvin-Helmholtz instability of the jet shear layer. Liquid fuel (*n*-heptane) droplets are introduced into the vortex structures, and processes of droplet-vortex interactions have been studied numerically by employing a third-order time-accurate, multidimensional, two-phase algorithm. The

effect of dispersed phase is incorporated through the source/sink terms in the gas-phase governing equations, representing the exchange of mass, momentum, and energy between the gas and liquid phases. Numerical results have been shown to be independent of the grid and temporal step size used in the simulation. In addition, simulation of the jet shear layer without droplets reproduced the large-scale features that have been observed in laboratory experiments and previous numerical simulations. For example, the simulation yields a Strouhal number of 0.36, based on the fundamental frequency of large-scale structures, which is within the reported experimentally range of 0.25–0.5. Detailed flow visualization has been employed to gain further understanding of the dispersion of evaporating droplets, and the effect of dispersed phase on the dynamics and time-averaged structure of the shear layer.

Results for the one-way coupled system indicate that the dispersion of intermediate-sized droplets is enhanced due to their interaction with vortex rings during the vortex-pairing process, that the dispersion enhancement can be characterized by a Stokes number based on the vortex-pairing frequency, that a second Stokes number based on a droplet transit time can be used to characterize the dispersion of larger droplets, and that the evaporation during droplet-vortex interaction has a significant influence on dispersion. Results on the dynamics of two-way coupled system indicate that for a non-evaporating spray at a mass loading of unity, the dynamics of shear layer and vortex rings are strongly influenced by the dispersed phase. The locations of shear layer rollup, vortex formation and pairing are shifted downstream, and their frequencies are reduced compared to those for the one-way coupled system. In addition, it is demonstrated that the shear layer stability can be modulated by changing the droplet injection characteristics. This has important implication for the dynamic behavior of two-phase flow systems, such as gas turbine combustors and liquid propellant rocket engines. For an evaporating spray, the effect of two-way coupling is much more complex compared to that for a non-evaporating spray. In general, the dynamics of shear layer and vortex structures for a two-way coupled evaporating spray become much less organized compared to the one-way coupled system.

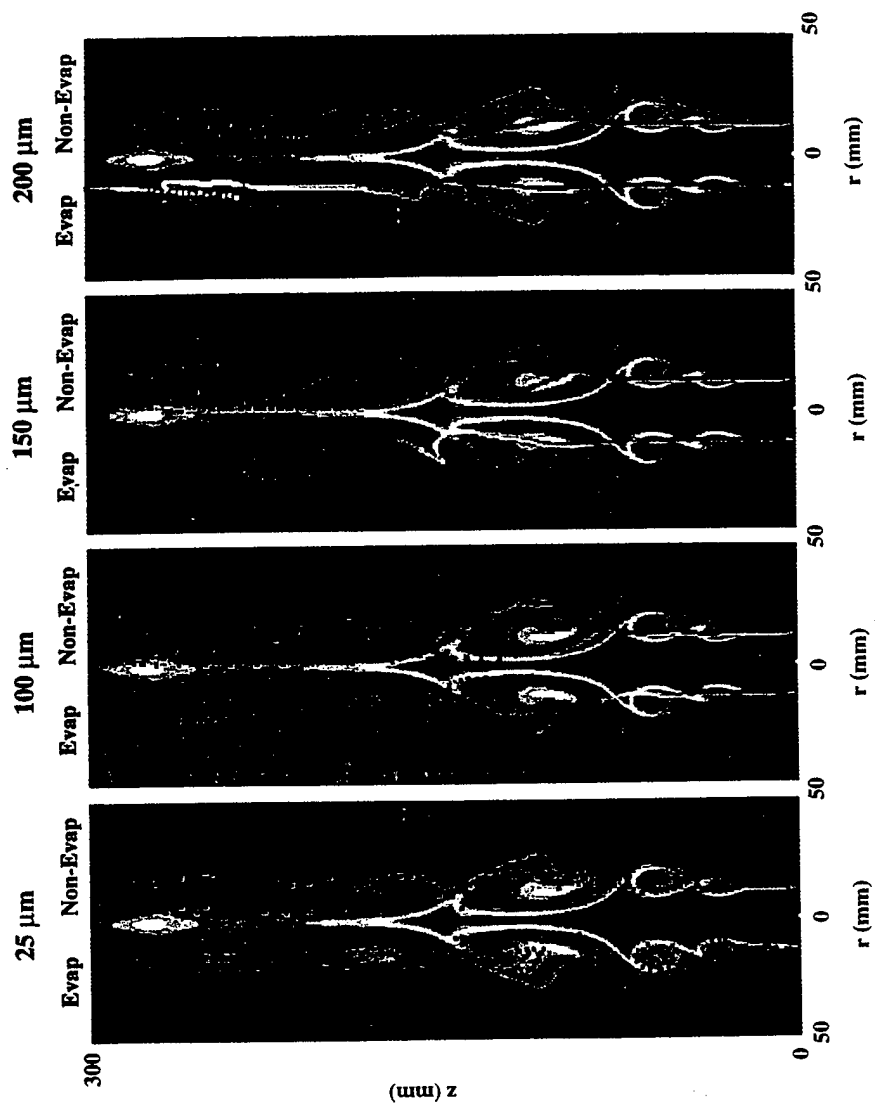
ACKNOWLEDGEMENTS

This work was funded by the AFOSR under Grant F49620-93-1-0400 monitored by Dr. Julian M. Tishkoff. Computations were performed on Cray C-90 at the Pittsburgh Supercomputing Center. Correspondence should be directed to S.K. Aggarwal. E-mail Suresh K. Aggarwal@uic.Edu

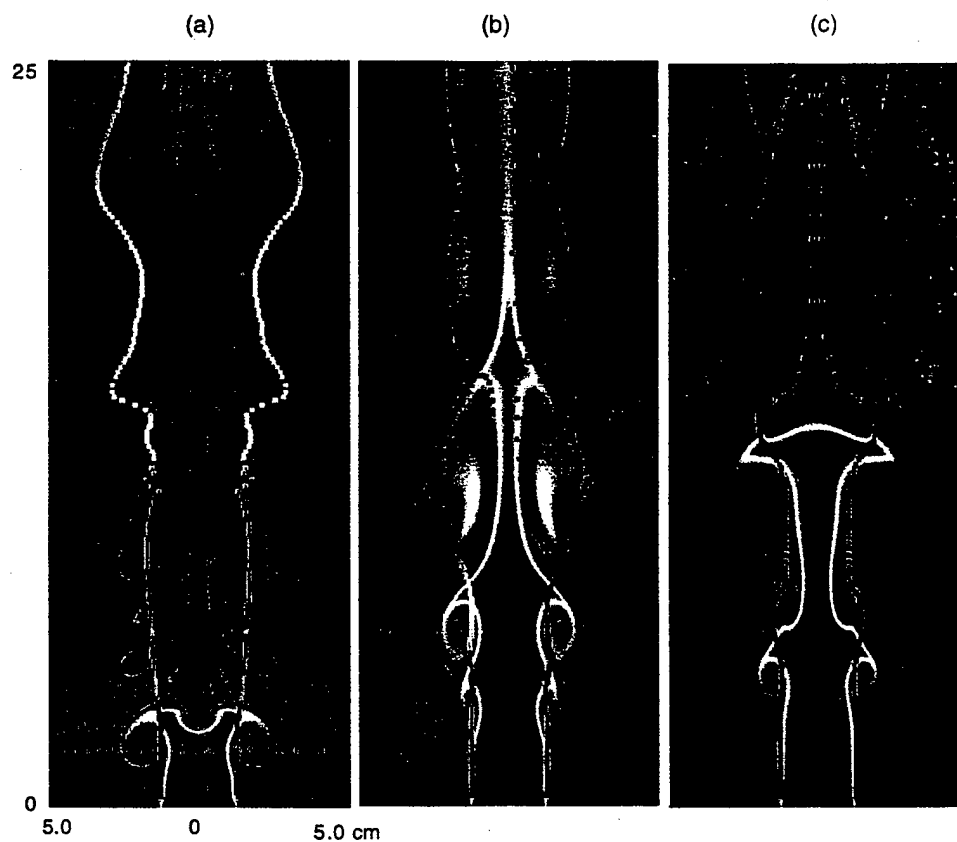
REFERENCES

- Abramzon, B. and Sirignano, W. A. (1989). *Int. J. Heat Mass Transfer*, **32**, 1605–1618.
- Aggarwal, S. K., Tong, A. and Sirignano, W. A. (1984). A Comparison of Vaporization Models for Spray Calculation. *AIAA Journal*, **22**, 1448–1457.
- Chung, J. N. and Troutt, T. R. (1988). Simulation of Particle Dispersion in an Axisymmetric Jet. *J. of Fluid Mech.*, **186**, 199–222.
- Hardalupas, Y., Taylor, A. M. K. P. and Whitelaw, J. H. (1992). Particle dispersion in a vertical round sudden-expansion flow. *Phil. Trans. R. Soc. Lond. A.*, **341**, 411–442.
- Hishida K., Ando, A. and Maeda, M. (1992). Experiments on Particle Dispersion in a Turbulent Mixing Layer. *International Journal of Multiphase Flow*, **18**, 181–194.

- Huerre, P. and Monkewitz, P. A. (1985). Absolute and Convective Instabilities in Free Shear Layers. *J. Fluid Mech.*, **159**, 151-168.
- Hussain, Z. D. and Hussain, A. K. M. F. (1983). Natural Instability of Free Shear Layers. *AIAA Journal* **21**, 1512-1517.
- Katta, V. R., Goss, L. P. and Roquemore, W. M. (1994). *Combustion and Flame*, Vol. **96**, pp. 60-74.
- Lazaro, B. J. and Lasheras, J. C. (1992). Particle Dispersion in the Developing Free Shear Layer, Part 2- Forced Flow. *J. Fluid Mech.*, **235**, 179-221.
- Leonard, B. P. (1979). A Stable and Accurate Convective Modelling Procedure Based on Quadratic Upstream Interpolation. *Comput. Methods in Applied Mechanics and Eng.*, **19**, 59-98.
- Longmire, E. K. and Eaton, J. K. (1992). Structure of a Particle-Laden Round Jet. *J. Fluid Mech.*, **236**, 217-257.
- Park, T. W., Aggarwal, S. K. and Katta, V. R. (1995). Gravity Effects on the Dynamics of Evaporating Droplets in a Heated Jet. *J. of Propulsion and Power*, **11**, 519-528.
- Park, T. W., Aggarwal, S. K. and Katta, V. R. (1996). A Numerical Study Of Droplet-Vortex Interactions In an Evaporating Spray, *Int. J. of Heat & Mass Transfer*, To appear.
- Subbarao, E. R. and Cantwell, B. J. (1992). Investigation of a coflowing buoyant jet - experiments on the effect of Reynolds number and Richardson number. *J. of Fluid Mech.*, **245**, 69-90.
- Uthuppan, J., Aggarwal S. K., Grinstein, F. F. and Kailasanath, K. (1994). Particle Dispersion in a Transitional Axisymmetric Jet: A Numerical Simulation. *AIAA Journal*, **32**, 2004-2014.



COMBUSTION SCIENCE AND TECHNOLOGY, Vols. 113-114 COLOR PLATE XI. See S. K. Aggarwal *et al.* Figure 4.



COMBUSTION SCIENCE AND TECHNOLOGY, Vols. 113-114 COLOR PLATE XII. See S. K. Aggarwal *et al.* Figure 8.

ON THE DYNAMICS OF A TWO-PHASE, NON-EVAPORATING SWIRLING JET

T. W. PARK* and V. R. KATTA**
Wright-Patterson Air Force Base, Ohio 45430

and

S. K. AGGARWAL+
Department of Mechanical Engineering
University of Illinois at Chicago, Chicago, IL 60607

(Received 1 August 1996; in revised form 23 May 1997)

+Corresponding author

Phone: (312) 996-2235 Fax: (312) 413-0447
email: ska@uic.edu

* NRC Post-Doctoral Fellow

** Innovative Scientific Solutions, Inc. Dayton, OH 45430

ON THE DYNAMICS OF A TWO-PHASE, NON-EVAPORATING SWIRLING JET

ABSTRACT

In this paper, we present direct numerical simulation of a droplet-laden swirling jet, and examine the effects of swirl and two-phase momentum coupling on the jet dynamics and structural characteristics. A time-dependent, multidimensional, two-phase algorithm is developed for the simulation. Results for the single-phase swirling jet at a Reynolds number of 800 indicate that the dynamics of large scale structures is strongly affected by the degree of swirl imparted to the incoming flow. For low and intermediate swirl intensities, the vortex rings rollup closer to the nozzle exit, their frequency increases, and pairing interactions become progressively stronger as the swirl number (S) is increased. Thus the addition of swirl to a transitional jet appears to modify its vortex dynamics in a way that enhances the beneficial effects of both swirl and vortex structures on the shear layer growth and entrainment. For a strongly swirling jet, the presence of a central stagnant zone and recirculation bubble cause a dramatic increases in the jet spreading angle, and this has a very dramatic effect on vortex dynamics. Based on a detailed visualization of the dynamic structure, we speculate that vortex structures in turn play an important role in determining the location and size of recirculation bubble. Results for the two-phase swirling jet indicate that for a mass loading ratio of unity, the jet dynamic and time-averaged behavior are strongly affected by both the interphase momentum coupling and swirl intensity. For a nonswirling two-phase jet, the momentum coupling modifies the dynamics of large vortex structures, including their rollup location and frequency, which leads to enhanced mixing and entrainment of colder fluid into the shear layer. In contrast, for weakly and moderately swirling two-phase jets ($S < 0.5$), the momentum coupling reduces the shear layer growth, as well as mixing and entrainment rate. As the swirl number is increased, the effect becomes progressively stronger, manifested by the reduced rate of decay of gas velocity and temperature along the jet axis. In addition, the relation between rollup frequency and swirl is modified in that the frequency increases with S for a single-phase jet, while it becomes independent of S for the corresponding two-phase jet. Consequently, the vortex pairing interactions, which are responsible for enhanced mixing and entrainment for single-phase swirling jets, are suppressed for two-phase jets. For strongly swirling two-phase jets ($S > 0.5$), the effect of momentum coupling becomes even more dramatic. Results for $S = 0.75$ indicate a drastic reduction in the size of the recirculation bubble for the two-phase jet.

INTRODUCTION

Swirling jet flows are utilized in a wide range of applications. By imparting swirl to the incoming flow, the structure of both nonreacting and reacting flows can be changed in a dramatic manner (Lilley 1977). The structure of swirling jet, for example, is strongly affected by the degree of swirl, characterized by a swirl number (S) which is defined as the ratio of axial flux of swirl or azimuthal momentum to that of axial momentum. For a weakly swirling nonreacting jet ($S < 0.4$), the jet growth, entrainment and decay are enhanced progressively as S is increased. For a corresponding strongly swirling jet ($S > 0.5$), the behavior changes more dramatically due to the formation of a recirculation bubble. In combustion applications, the recirculation bubble perhaps represents the most significant and useful effect of swirl, as it plays a central role in flame stabilization and enhanced combustor performance.

Extensive research efforts have been expended in understanding and characterizing the effects of swirl in nonreacting and reacting flows (Lilley 1977; Ribeiro & Whitelaw 1980;

Leschziner & Rodi 1984). A commonly used configuration in both experimental and computational studies involves a confined or free swirling jet. Most of these studies, however, deal with the time-averaged behavior of swirling single-phase (Leschziner & Rodi 1984; Dellenbach et al. 1988; Durst & Wennerberg 1991) and two-phase jets (Sommerfeld & Qui 1993). The transient aspects, particularly those associated with large-scale vortex structures, have not been examined, although these structures have been shown to have a dominant effect on the near jet flow dynamics of non-swirling jets. Numerous experimental and numerical studies (Crow & Champagne 1971; Yule 1978) have shown that toroidal vortex rings form periodically in the near field of round jets and convect downstream. These axisymmetric structures roll around due to the inhomogeneous flow field, and may also undergo pairing interactions, depending on the flow conditions, such as initial disturbance level and other experimental conditions. In addition, their dynamics can be modified significantly by external forcing (Reynolds & Bouchard 1981). There are also other mechanisms that can modify their temporal and spatial growth characteristics. These include acoustic (pressure) fluctuations (Kailasanath et al. 1989), which can modify the dominant frequency associated with large scale structures, compressibility effects (Shau et al. 1993) and density variations caused by a variation in temperature or molecular weight (Subbarao & Cantwell 1992). Yet another mechanism that may alter the dynamic of large scale structures pertains to the effect of swirl, which induces a body force in the radial momentum equation, and an adverse pressure gradient in the axial direction. For weakly swirling jets, the axial adverse pressure gradient caused by swirl can modify the processes of vortex rollup and pairing interactions. For strongly swirling jets, the jet spreading and recirculation zone created by the swirl effect can have a more dramatic effect on the dynamics of vortex rings. To our knowledge, these aspects dealing with the dynamic interactions between large scale structures and swirl, and those between large structures and droplets in a swirling shear flow, have not been investigated in previous studies.

In this paper, we present a numerical simulation of a droplet-laden swirling jet. The major objective of this study is to investigate the dynamics of large scale structures under different swirl conditions, and their interactions with the droplets injected in the shear layer of an axisymmetric swirling jet. A direct numerical solver without any turbulence or subgrid model is employed. The simulation first examines the dynamics of vortex rings and their interactions with the swirling flow field in a transitional heated jet. Then, a droplet-laden swirling jet is simulated in order to examine the effects of two-phase momentum coupling on the jet dynamics and structural behavior. The jet Reynolds number based on a jet velocity of 5.0 m/s, diameter of 25.4 mm, and kinematic viscosity of heated jet fluid is 800. In our earlier study (Aggarwal et al. 1996), the dynamics of a nonswirling two-phase jet was investigated, and it was shown that the shear layer stability and vortex dynamics can be modified significantly by controlling the droplet injection characteristics.

The present study extends that work to a swirling two-phase jet, and examines the effects of both swirl and two-phase momentum coupling on its dynamic and time-averaged structure.

PHYSICAL-NUMERICAL MODEL

A cartoon of the two-phase swirling jet investigated in the present study is shown in Fig. 1. It consists of a central swirling jet which is a two-phase mixture of air and liquid fuel (n-heptane) droplets and a low-speed annular air flow. The jet at axial velocity of 5.0 m/s and temperature of 1200 K is issuing into a coflow with a velocity of 0.2 m/s without swirl and temperature of 294 K. Note that the use of high jet temperature is based on the consideration that we plan to investigate an evaporating spray in a subsequent study. In the present study, a nonevaporating spray is simulated in order to examine the effects of two-phase momentum coupling in the near region of a swirling jet. The jet-shear-layer instability is primarily of the Kelvin-Helmholtz type (Aggarwal et al. 1996).

The numerical model is based on solving the time-dependent, two-phase equations in an axisymmetric geometry. The unsteady, axisymmetric governing equations in cylindrical (z, r) coordinates for a droplet-laden swirling jet are

$$\frac{\partial(\rho\Phi)}{\partial t} + \frac{\partial(\rho u\Phi)}{\partial z} + \frac{\partial(\rho v\Phi)}{\partial r} = \frac{\partial}{\partial z} \left(\Gamma^\Phi \frac{\partial\Phi}{\partial r} \right) + \frac{\partial}{\partial r} \left(\Gamma^\Phi \frac{\partial\Phi}{\partial z} \right) - \frac{\rho v\Phi}{r} + \frac{\Gamma^\Phi}{r} \frac{\partial\Phi}{\partial r} + S_s^\Phi + S_r^\Phi. \quad (1)$$

The general form of Eq. (1) represents the continuity, three momentum, and energy conservation equations depending on the variable used for Φ . The transport coefficients Γ^Φ and the source terms S_s^Φ and S_r^Φ that appear in the governing equations are listed in Table 1. Note that the equations in Table 1 correspond to an evaporating two-phase flow. For the present study, which simulates a non-evaporating two-phase flow, the species equations are not considered, and droplet vaporization rate (\dot{m}_k) is taken identically equal to zero. The transport coefficients Γ^Φ and source terms contain the fluid properties such as viscosity (μ), thermal conductivity (λ), and specific heat (C_p). They are considered functions of temperature and species concentration.

The effect of dispersed phase on gas-phase properties is incorporated through the source/sink terms (S_i^Φ), representing the exchange of momentum between the gas and dispersed phases. In order to evaluate these terms, it is necessary to establish droplet trajectories. The Lagrangian approach is employed to solve the liquid-phase governing equations for the dynamics of each droplet group. The spray is characterized by a discrete number of droplet groups, distinguished by their injection location, initial size, and time of injection. A droplet group in a Lagrangian treatment represents a characteristic group containing a finite number of droplets. Since an axisymmetric configuration is analyzed, the liquid properties are implicitly averaged in the azimuthal direction and the number of droplets associated with each characteristic group represents

droplets uniformly distributed in an annular ring. The equations governing the variation of position and velocity of each droplet are as follows:

$$\frac{dz_k}{dt} = u_k \quad (2)$$

$$\frac{dy_k}{dt} = v_k$$

$$\frac{du_k}{dt} = \frac{3C_D\rho_g}{4d_k\rho_k}|u - u_k|(u - u_k) + \left(\frac{\rho_g}{\rho_k} - 1\right)g \quad (3)$$

$$\frac{dv_k}{dt} = \frac{3C_D\rho_g}{4d_k\rho_k}|v - v_k|(v - v_k) + \frac{w_k^2}{y_k}$$

$$\frac{dw_k}{dt} = \frac{3C_D\rho_g}{4d_k\rho_k}|w - w_k|(w - w_k) - \frac{v_k w_k}{y_k}$$

where

$$C_D = \frac{24}{\text{Re}_k} \left(1 + \frac{\text{Re}_k^{2/3}}{6} \right) \quad (4)$$

$$\text{Re}_k = \frac{\rho_g \left\{ (u - u_k)^2 + (v - v_k)^2 + (w - w_k)^2 \right\}^{1/2} d_k}{\mu_g} \quad (5)$$

In the above equations, z_k and y_k are respectively the instantaneous axial and radial locations of a droplet group, while u_k , v_k , and w_k are respectively its axial, radial, and azimuthal velocity components. Further, d_k , ρ_k , and Re_k are respectively the droplet size, material density and Reynolds number, whereas ρ_g and μ_g are the gas density and viscosity respectively. In the present simulation, we consider nonevaporating n-heptane droplets. In a subsequent study, we plan to extend the analysis to evaporating droplets. The density of n-heptane fuel is assumed to be 649.4 kg/m³, which yields a value of more than 100 for the ratio of droplet density to gas density, with the latter value based on an average gas temperature of 750 K. This sufficiently large density ratio allows us to neglect the Basset force, pressure gradient and other contributions from flow non-uniformities and consider only the quasi-steady drag and gravity forces in Eq. 3.

The numerical solution of the unsteady two-phase equations employs an implicit algorithm for solving the gas-phase equations, and an explicit Runge-Kutta procedure for the liquid-phase

equations. The finite-difference forms of the momentum equations are obtained using an implicit QUICKEST scheme (Leonard 1979), while those of energy equations are obtained using an hybrid scheme of upwind and central differencing (Spalding 1972). A "finite control volume" approach with a nonuniform staggered-grid system is utilized. An orthogonal grid having expanding cell sizes in both the axial and the radial direction is employed. An iterative ADI (Alternative Direction Implicit) technique is used for solving the resulting sets of algebraic equations. At every time step, the pressure field is calculated by solving all the pressure Poisson equations simultaneously and utilizing the LU (Lower and Upper diagonal) matrix decomposition technique.

Axisymmetric calculations are made on a physical domain of 400 x 150 mm utilizing a 151 x 61 nonuniform grid system. The computational domain is bounded by the axis of symmetry and an outflow boundary in the radial direction and by the inflow and another outflow boundary in the axial direction. The outer boundaries in the z and r directions are located sufficiently far from the nozzle exit (16 nozzle diameters) and the axis of symmetry (6 nozzle diameters), respectively, to minimize the propagation of boundary-induced disturbances into the region of interest (7 and 2 nozzle diameters in the axial and radial directions, respectively). A flat profile for axial velocity and a linear profile for swirl velocity (swirl velocity being a linearly increasing function of radius) are used at the inflow boundary. It is important to mention that for a given swirl number, one can employ different swirl velocity profiles at the inflow boundary, and this may affect the jet development. However, a linear velocity profile provides a good approximation to the real situation, and has often been used in computational studies (Ribeiro & Whitelaw 1980; Leschziner & Rodi 1984). A zero-gradient boundary condition with an extrapolation procedure with weighted zero- and first-order terms is used to estimate the flow variables at the outflow boundary. The weighting functions are selected using the trial-and-error approach, and the main criterion used is that the vortices crossing the outflow boundary leave smoothly without being distorted. For the given flow conditions, a steady-state solution was first obtained by neglecting the unsteady terms in the governing equations. Then, the unsteady two-phase swirling jet simulations were performed using the previously obtained steady-state solution as the initial flow condition.

The liquid-phase equations governing the position of each droplet group are advanced in time by a second-order accurate Runge-Kutta method. Since the gas-phase solution employs an implicit procedure, the temporal step size used for integrating the liquid-phase equations is usually smaller than that for gas-phase equations. An automatic procedure is implemented in order to select an optimum liquid-phase time step. The procedure to advance the two-phase solution over one gas-phase time step is as follows. Using the known gas-phase properties, the liquid-phase equations are solved over the specified number of liquid-phase subcycles. A third-order accurate Lagrangian polynomial method is used for interpolating the gas-phase properties from the nonuniform fixed grid to the droplet characteristic location. It should be noted that the interpolation scheme for the

gas-phase velocities u and v is based on their respective grid cells because of the use of a staggered grid in gas-phase calculation. The droplet properties are updated after every liquid-phase subcycle. Also, during each subcycle, the liquid-phase source terms appearing in the gas-phase equations are calculated at the characteristic location, and then distributed to the surrounding gas-phase grid points. These source terms are added at each gas-phase grid points during one gas-phase time step and then used in the implicit solution of the gas-phase equations. It is also important to note that the integration of droplet equations (Eq. 3) in cylindrical coordinates require special care near the axis of symmetry, where a specular boundary condition is imposed. This implies that as a droplet approaches the left boundary, it is replaced by another droplet entering the domain at the reflected angle.

Numerical validation studies for both single-phase and two-phase jets, as well as for low-speed diffusion flames, employing different grids and temporal step sizes have been reported previously (Aggarwal et al. 1996; Katta et al. 1994). Some additional results showing grid independence are depicted in Fig. 2. The time-history of gas velocity computed for two different grid sizes, 151×61 and 226×91 for non-swirling and swirling jets is plotted in figs 2a and 2b, while the profiles of time-averaged velocity along the jet axis for three different swirl numbers are plotted in Fig. 2c. Since a non-uniform grid is employed with grid lines clustered near the shear layer to resolve the steep gradients of the dependent variables, additional grid points in the 226×91 grid are placed near the shear layer, thus effectively reducing the grid density for this grid by nearly hundred percent compared to the 151×61 grid. The time-history plots of gas velocity clearly depicts the highly periodic nature of jet vortex rings associated with the Kelvin-Helmholtz instability. For the non-swirling jet, the Strouhal number associated with this instability obtained from the fast Fourier transform of axial velocity is 0.33, which agrees with the reported experimental range of 0.25-0.5 (Hussain & Hussain 1983). The aspects pertaining to the dynamic and time-averaged jet behavior for different swirl numbers are discussed in the next section. Important observation here is that the 151×61 grid is able to capture the periodic behavior, including frequency and phase of the vortex structures, as well as the time-averaged structure of both non-swirling and swirling jets.

RESULTS

The swirl number is defined as

$$S = \frac{1}{r_o} \frac{\int_0^{r_o} u w r^2 dr}{\int_0^{r_o} u^2 r dr} \quad (6)$$

where r_0 is the radial extent of computational domain, r is the radial coordinate, and u and w are respectively the gas axial and azimuthal velocity components. This definition treats S as a function of axial distance. Thus, at the inflow boundary r_0 becomes equal to the jet radius.

First, we examine the dynamics of single-phase swirling jets at different swirl numbers (S). The objective is to understand and characterize the dynamic interactions between swirl and large scale structures, and the effects of these interactions on the jet behavior. Since the jet dynamics and structural characteristics are strongly influenced by the presence of both swirl and large scale structures, it is of interest to examine how the vortex dynamics is affected by swirl, and how the distribution of swirl and its decay rate are modified by vortex structures. The latter effect is important since the swirl decay rate determines the pressure distribution, and thereby the jet gross behavior, especially the onset, location and extent of the recirculation bubble at high swirl numbers. The above interactions are examined by employing flow visualization (snapshots of the flow field), as well as the instantaneous and time-averaged properties.

Figure 3 shows some representatives snapshots of the flow field for different swirl numbers. In each snapshot, we plot instantaneous iso-temperature contours on the right, and streaklines on the left. Simulations for the nonswirling jet indicate the presence of well-organized vortex rings. Toroidal vortex rings roll up periodically near $z = 4$ cm ($z/D = 1.6$) from the nozzle exit, convect downstream, and undergo a weak pairing interaction near $z = 16$ cm. The snapshot for $S=0$ clearly indicates a vortex rollup occurring near $z = 4$ cm, and a pairing interaction near $z = 16$ cm. These results were confirmed by the fast Fourier transform of axial velocity recorded at several axial locations, shown in Fig. 4a, which yields dominant frequencies of 64 and 32 Hz corresponding to the roll up and merging frequencies respectively. Results for $S = 0.375$, Fig. 3, indicate a more dramatic effect of swirl on the dynamics of large scale structures. First of all, the vortex rollup location is shifted upstream and frequency is increased from 64 to 75 Hz compared to the nonswirling case. Second, the vortex pairing becomes a prominent feature of shear layer dynamics in the near jet region, which, we speculate, is caused by the adverse pressure gradient effect of swirl. Since, the pressure increases along the center line for the swirling case, the center-line velocity for the swirling jet decays faster compared to that for the nonswirling jet. This is indicated clearly in Fig. 5a, which shows the variation of time-averaged gas velocity along the center line for different swirl numbers. As a result, the leading toroidal vortex is slowed down, causing a well-organized pairing interaction to occur near $z = 7$ cm. The faster decay of center-line velocity also causes the occurrence of second vortex pairing near $z = 12$ cm. The processes of shear layer rollup and pairing interactions for $S=0.375$ are clearly depicted in Fig. 3. The corresponding frequencies, obtained from the fast Fourier transform of axial velocity and displayed in Fig. 4b, are 74, 37, and 19 Hz respectively. The occurrence of multiple vortex pairings in a swirling jet has an

important implication with regard to the effect of swirl-vortex interaction on the jet development and entrainment. Since the presence of multiple vortex pairings is known to enhance shear layer growth and entrainment, the numerical results indicate that the addition of swirl modifies vortex dynamics in a way which further enhances the beneficial effects of swirl.

As the swirl intensity is increased, the above effects become progressively stronger. The increased swirl strength promotes greater jet spreading, mixedness, and reduction of the potential core. In addition, the vortex rollup occurs earlier (more upstream), and the convecting toroidal vortex slows down considerably, as it moves radially outward (due to jet spreading) and the center-line velocity decays more rapidly. Consequently, with increased swirl, vortex pairings occur earlier and with greater intensity, further promoting shear layer growth and entrainment. For $S = 0.5$, as noted in Fig. 3, the locations of vortex rollup, and first and second pairing interactions are approximately at $z = 2, 5$, and 8 cm respectively, compared with the corresponding values of $3, 7$, and 10 cm for $S = 0.375$. In addition, the corresponding frequencies are higher and a third pairing interaction is observed for $S = 0.5$; see Fig. 4c. The above observations are also confirmed by the axial profiles of time-averaged gas velocity and temperature shown in Fig. 5. As S is increased, the centerline temperature decreases more rapidly, indicating a pronounced increase in the shear layer growth and entrainment of colder fluid into the hot jet. This is a significant result in that the overall effect of swirl-vortex interaction at low to intermediate swirl intensities ($S < 0.5$) is to augment the effect of each. Note that both the addition of swirl and the presence of large vortex structures are known to enhance shear layer growth and entrainment. Our results indicate that an increase in swirl intensity promotes multiple vortex pairings, which further enhances shear layer growth and entrainment, i.e. large structures augment the effect of swirl and vice versa.

A more dramatic effect occurs as the swirl number exceed 0.5 , which represents the onset of recirculation bubble in the jet flow. For $S > 0.5$, a stagnant region develops near the center line due to the reverse flow caused by adverse pressure gradient, and a toroidal recirculation bubble appears. Both the central stagnation region and recirculation bubble can be seen clearly from the time-averaged velocity vector plots in Fig. 6. Also notable in this figure is the presence of a secondary recirculation zone for $S = 0.75$, located just upstream of the primary recirculation bubble. The stagnation region and reverse flow are also quite evident in the time-averaged axial velocity profile for $S = 0.75$ given in Fig. 5. In addition, as noted in Fig. 6, the jet shear layer for $S = 0.75$ is shifted significantly outward in the radial direction, and exhibits a highly dynamic structure. It is interesting to note that while at subcritical swirl numbers ($S < 0.5$), toroidal vortices are an intrinsic part of jet dynamics, their existence becomes less obvious at supercritical swirl numbers ($S > 0.5$). Thus, an important issue to be addressed here pertains to the existence and nature of large scale structures for strongly swirling jets, and whether the transient jet behavior can be attributed to these structures. One may argue that these structures get destroyed due to the rapid

decay of shear and increased mixing in a strongly swirling jet. Based on an extensive visualization of the swirling jet dynamics for $S = 0.75$, we speculate that large vortex structures are still present, though their behavior is markedly different from those for the weakly and moderately swirling jets ($S < 0.5$). The vortex structures for $S = 0.75$ are shifted outward in the radial direction and do not look like the Kelvin-Helmholtz vortex rings that are typically observed in a transitional jet. However, a series of snapshots (not shown) indicates that they do exhibit the processes of rollup and pairing interactions, though in a significantly less organized manner. The snapshots further indicate that a pair of counter-rotating toroidal vortices (an outer Kelvin-Helmholtz type vortex rotating clockwise and an inner vortex rotating counter-clockwise; the latter may be due to the presence of central stagnation region) is generated periodically. As these vortices convect downstream, they grow in size, and the outer structure roll around the inner structure since the latter is in a nearly stagnant region. In addition, both outer and inner vortices undergo pairing interactions with other (trailing) outer and inner vortices respectively. We also speculate, based on the flow visualization and time-averaged velocity vector plots shown in Fig. 6, that the size and location of recirculation bubble is determined by these dynamic swirl-vortex interactions, and not by the adverse pressure gradient (swirl effect) alone. In other words, due to the effect of swirl, the outer vortex is shifted outward in the radial direction, and its subsequent dynamics as well as that of inner vortex are determined by the swirling flow field. These vortices in turn play a major part in determining the location of recirculation zone; it appears that the recirculation zone is established at a location where the outer vortex structure is pulled in radially.

Two-Phase Momentum Coupling Effects

We now examine the effects of two-phase momentum coupling on the dynamics and time-averaged characteristics of a droplet-laden swirling jet. Droplets of a given size are injected from the nozzle rim, and their motion is followed by integrating Eqs. (2-3) using a second-order Runge-Kutta scheme. At low mass loadings, the effect of droplets on the jet dynamics is negligible, although their motion and concentration field are strongly influenced by the rotating toroidal vortices. As the dispersed-phase mass loading is increased, the effects due to the exchange of mass, momentum, and energy between the phases become increasingly important. In the present study, a nonevaporating two-phase jet is considered in order to isolate momentum coupling effects from those due to mass and energy coupling. These effects depend on several parameters, including liquid-to-air mass loading ratio and injection characteristics such as initial droplet size, location, and velocity. For the present study, we consider mass loading of unity* and initial droplet

* In an earlier study [16], it is shown that at unity mass loading, two-phase momentum coupling has a significance influence on the jet dynamics and structural characteristics.

diameter of 100 μm , with the droplets injected in the shear layer with axial velocity same as the jet velocity, and zero radial and azimuthal velocities. Note that the choice of droplet diameter is based on the consideration that it yields a Stokes number of near unity for the nonswirling jet. The Stokes number here is defined as the ratio of droplet response time to a characteristic flow time, the latter based on the dominant vortex frequency. Several experimental (Longmire & Eaton 1992) and numerical studies (Chung & Troutt 1988; Uthuppan et al. 1994; Park et al. 1996) have shown that the interaction of large structures with droplets is maximized near a Stokes number of unity.

Flow visualization is used to assess qualitatively the effects of dispersed phase on the dynamics of large scale structures under different swirl conditions. In the following discussion, case A refers to single-phase jets, while B refers to two-phase jets. Figure 7 depicts representative snapshots of the flow field for different swirl numbers. For these results, a droplet group is introduced every tenth computational time step, and the computations are performed for a total of 10000 time steps. Thus, there are 1000 droplet groups for the two-phase results shown in Fig. 7. Comparison of the snapshots, for nonswirling ($S = 0$) single-phase and two-phase jets, given in Figs. 3 and 7 respectively, indicates that the vortex rollup location, dynamics, and pairing interactions are strongly modified due to momentum coupling. In addition, it is observed that for the two-phase jet (case B), the vortex structures are stronger and entrain more low-speed (colder) fluid compared to those for the single-phase jet (case A). The comparison of snapshots for swirling jets also indicates a significant modification of vortex dynamics due to the momentum coupling effect. For low to moderate swirl numbers ($S < 0.5$), the vortex pairing is a prominent feature of jet dynamics for case A, while it is not observed for case B. For the strong swirl case ($S = 0.75$), an important effect of two-phase momentum coupling is a drastic reduction in the size of recirculation bubble, even though the central stagnation region still exists. This can be seen more clearly in terms of time-averaged velocity vector plots in Fig. 11. The effect of momentum coupling on the time-averaged structure is discussed in the following section.

The above observations are confirmed by obtaining the spectral and time-averaged properties for the two cases. Figure 8 shows the time history of gas-phase axial velocity for single-phase and two-phase jets at different swirl numbers. Results of the fast Fourier transform of these axial-velocity histories are depicted in Figs. 4 and 9. As discussed earlier, for single-phase jets with low to moderate swirl numbers ($S < 0.5$), the processes of shear layer roll-up and vortex formation are well organized. In addition, the roll-up frequency increases and pairing interactions become more prominent as the swirl number is increased. These results are quite evident in Fig. 4; the roll-up frequencies are 64, 72, and 80 Hz for $S = 0$, 0.375, and 0.5 respectively. Also noteworthy in Fig. 4 are the first and second pairing interactions at frequencies of 36 and 18 Hz respectively for $S = 0.375$, and at 40 and 20 Hz respectively for $S = 0.5$. In contrast, for the corresponding two-phase jets (case B), the shear layer dynamics is relatively less organized, and

the roll-up frequency decreases and becomes independent of the swirl number. As indicated in Figs. 8 and 9, the roll-up frequency is 50 Hz for $S = 0, 0.375$, and 0.5 . Another important observation from Fig. 9 is the absence of pairing interactions for case B, which is also evident in Fig. 7. This is attributable to the fact that the interphase momentum coupling modifies the distribution of swirl intensity in the axial direction, resulting in a decrease of adverse pressure gradient and jet spreading angle. As noted earlier, the adverse pressure gradient caused by swirl is responsible for the enhanced vortex pairings in single-phase jets. For corresponding two-phase jets, there is a transfer of azimuthal momentum from the gas phase to droplets, which reduces swirl intensity near the nozzle. Further downstream, however, the momentum is transferred from droplets to gas phase, increasing the gas-phase swirl intensity. The resulting redistribution of swirl intensity reduces the adverse pressure gradient for the two-phase jet. This was confirmed by plotting the time-averaged azimuthal velocity contours (not shown) and axial velocity vectors, shown in Fig. 11. As a consequence, the vortex pairing, which is prominent feature of moderately swirling ($S < 0.5$) single-phase jets, is not observed for corresponding two-phase jets.

Momentum-Coupling Effect on the Time-Averaged Jet Structure

The effect of two-phase momentum coupling on the time-averaged jet behavior is depicted in Figs. 10 and 11. In Fig. 10, the time-averaged axial gas velocity and temperature are plotted along the jet center line, while Fig. 11 shows the time-averaged velocity vectors for different swirl numbers. The important observations from these results is that at a mass loading of unity, the dispersed phase significantly modifies the time-averaged structure of the jet shear layer, and the degree of modifications depends on the swirl intensity. For the non-swirling jet ($S = 0$), as the shear layer develops, the gas-phase velocity decreases along the center line. Since the droplets are injected at the jet velocity, they now have higher velocity than the gas phase resulting in a transfer of momentum from the dispersed phase to gas phase. This seems to enhance the shear layer instability resulting in enhanced mixing and entrainment of colder fluid, as evidenced by a faster decay of centerline temperature and velocity for the two-phase jet compared to those for the single-phase jet. This effect is modified significantly by the introduction of swirl. As noted earlier, the addition of swirl ($S = 0.375$) to a single-phase jet causes a faster decay of the centerline velocity (compared to a non-swirling jet), resulting in vortex pairing. This leads to enhanced mixing and entrainment of colder fluid into the shear layer; note a sharp increase in the rate of decrease of centerline velocity near an axial location of 120 mm for the single-phase jet. For the corresponding two-phase jet, the transfer of azimuthal momentum from the gas phase to droplets reduces the swirl intensity near the nozzle. This initially ($z < 120$ mm) causes a faster decay of centerline velocity for the two-phase jet compared to that for the single-phase jet. Further downstream, however, the direction of azimuthal momentum transfer is reversed, resulting in a slower decay of centerline

velocity for the two-phase jet. In addition, the absence of vortex pairing for two-phase jet further reduces the rate of decay of centerline velocity. Consequently, the centerline velocity of two-phase jet becomes higher than that of single-phase jet for $z > 120$ mm. The absence of vortex pairing also results in reduced mixing and entrainment for the two-phase jet. Consequently, as indicated in Fig 10b, the centerline temperature decreases less rapidly for the two-phase jet.

The above effects become progressively stronger as the swirl number is increased. For $S = 0.5$, as shown in Fig. 10a, the centerline velocity of single-phase jet first decreases quite rapidly due to the combined effects of shear layer growth, adverse pressure gradient, and vortex pairings, and then ($z > 100$ mm) increases due to the transfer of axial momentum in the radial direction; see also Fig. 6. For the corresponding two-phase jet, the centerline velocity decreases much less rapidly, again due to the reduced pressure gradient and the absence of vortex pairings. The centerline temperature also decreases slowly for the two-phase jet, again implying reduced mixing and entrainment due to the momentum coupling effect. Another effect of momentum coupling is seen from the comparison of time-averaged velocity vectors for single-phase and two-phase jets given in Figs. 6 and 11 respectively. The comparison of these figures show that due to the momentum transfer from droplets to gas phase in the jet shear layer, the jet width is decreased and the potential core is lengthened for the swirling two-phase jet. The effect becomes more distinguishable for $S = 0.5$ and 0.75 , where the momentum coupling generates a curtain (or envelope) type of high-velocity narrow region inside the shear layer. An important consequence of this high-velocity curtain is the near disappearance of the stagnation region for swirling two-phase jet for $S = 0.5$, and that of recirculation bubble for $S = 0.75$. The presence of a large recirculation bubble is perhaps the most distinguishing feature of a strongly swirling ($S = 0.75$) single-phase jet; see Figs. 3 and 6. For the corresponding two-phase jet, our results indicate that the recirculation bubble becomes nearly non-existent, even though the central stagnation and reverse flow regions still exist inside the high-velocity curtain. The disappearance of recirculation bubble for the strongly swirl case may be attributed to the momentum coupling effect, i. e., the transfer of various momentum components between the phases. Initially, there is a transfer of swirl momentum from the gas phase to dispersed phase, causing swirling intensity to decrease much more rapidly for two-phase jet (case B) compared to that for single-phase jet (case A). At some downstream location, however, the direction of azimuthal momentum transfer reverses, since droplets have higher momentum there. Secondly, the jet spreading rate is reduced for case B due to the radial momentum transfer from the gas phase to dispersed phase. In addition, there is a reverse transfer of axial momentum, i. e., from the dispersed phase to gas phase, since the gas-phase axial velocity decreases more rapidly than that of dispersed phase, generating the high-velocity curtain mentioned earlier. All of these effects, i. e., reduced entrainment, more rapid decay of swirl velocity initially, and increase of gas velocity, lead to a near disappearance of the recirculation

77

bubble for the strongly swirling two-phase jet. Consequently, for strongly swirling jets ($S > 0.5$), the jet spreading angle, shear layer growth and entrainment are reduced significantly due to the effect of interphase momentum coupling.

CONCLUSIONS

In this paper, we have investigated the effects of swirl and two-phase momentum coupling on the dynamics and structural behavior of a droplet-laden swirling jet. A direct numerical solver based on an Eulerian-Lagrangian formulation, but without any turbulence or subgrid model, has been employed to simulate the transient behavior of a transitional swirling jet. Numerical results have been shown to be grid-independent both in terms of the global predictions and the detailed spatio-temporal profiles of relevant gas-phase profiles at different swirl numbers. In addition, the predicted Strouhal number associated with the large-scale structures for the non-swirling jet has been shown to be in agreement with the available experimental data. Then, a detailed flow visualization based on numerical simulation has been used to examine the dynamics of large scale structures and their interactions with the droplets in weakly and strongly swirling jet shear layers. In addition, the effects of swirl and dispersed phase on the time-averaged jet structure have been characterized. Important observations are as follows.

Results for single-phase swirling jets indicate that the dynamics of large scale structures is strongly affected by the degree of swirl imparted to the incoming jet. For low and intermediate swirl intensities, the vortex rings rollup closer to the nozzle exit, their frequency increases, and pairing interactions become progressively stronger as the swirl number is increased. For example, there is one weak vortex merging near $z/D = 6$ for the nonswirling jet, and two vortex mergings near $z/D = 3$ and 5 for $S=0.375$, while for $S = 0.5$, the vortex mergings become stronger and occur near $z/D = 2$ and 3 respectively. Consequently, the interaction of vortex rings with the swirling flow field gives rise to a mechanism, which seems to be responsible for the enhanced shear layer growth and entrainment, and has not been observed in previous studies. This may be an important result, with the implication that the addition of moderate swirl to a transitional jet modifies its vortex dynamics in a way that further enhances the beneficial effects of both swirl and vortex structures on shear layer growth. For a strongly swirling jet, the presence of a central stagnant zone and recirculation bubble causes a drastic increase in the jet spreading angle, and this has a rather dramatic effect on vortex dynamics. Detailed visualization of the shear layer dynamics indicates that as the shear layer is shifted radially outward, a pair of counter-rotating toroidal vortices is generated periodically, and the eventual shear layer structure, including the location of recirculation bubble, is determined by the dynamic interactions of these structures with the stagnant zone and recirculation bubble.

Results for the two-phase swirling jet indicate that at a mass loading ratio of unity, the jet dynamics and structural characteristics are strongly modified by the interphase momentum coupling. Depending upon the amount of swirl imparted to the jet, the momentum coupling can cause varied and in some cases dramatic effects on the dynamic and time-averaged jet structure. For a nonswirling jet, the momentum coupling alters the dynamics of large vortex structures, modifying their rollup location and frequency, and causing enhanced mixing and entrainment of colder fluid into the shear layer. In contrast, for weakly and moderately swirling jets, the momentum coupling reduces the amount of adverse pressure gradient, and suppresses the vortex pairing interactions. These effects are caused by the redistribution of gas-phase axial, radial, and swirl momentum components due to the dispersed phase, and lead to significantly reduced shear layer growth, mixing and entrainment rates for two-phase jets compared to those for single-phase jets. In addition, the correlation between vortex frequency and swirl number is modified due to momentum coupling. For example, the dominant vortex frequency of single-phase jets increases with increasing swirl number, while that of two-phase jets appears to be independent of S .

At high swirl numbers ($S > 0.5$), the effects of momentum coupling on the jet structure appears to be even more dramatic compared to those at moderate swirl numbers. Results for $S = 0.75$ indicate that momentum coupling can significantly modify the rate of decay of swirl intensity, and increase the gas axial momentum in the jet shear layer, leading to a dramatic reduction in the size of recirculation bubble.

ACKNOWLEDGMENT

This work was in part funded by the AFOSR under Grant F49620-93-1-0400 monitored by Dr. Julian M. Tishkoff. One of the authors (TWP) was supported by the NRC Fellowship. Computations were performed on Cray C-90 at the Pittsburgh Supercomputing Center.

REFERENCES

- Aggarwal, S. K., Park, T. W. & Katta, V. R. 1996 Unsteady Spray Behavior in a Heated Jet Shear Layer: Droplet-Vortex Interactions, *Combustion Science and Technology*, **113-114**, 429-450.
- Chung, J. N. & Troutt, T. R. 1988 Simulation of Particle Dispersion in an Axisymmetric Jet, *J. Fluid Mech.* **186**, 199-222.
- Crow, S. C. & Champagne, F. H. 1971 Orderly Structure in Jet Dynamics, *J. Fluid Mech.* **48**, 547-591.
- Dellenbach, P.A., Metzger, D.E. & Neitzel, G.P. 1988 Measurements in Turbulent Swirling Flow Through an Abrupt Axisymmetric Expansion, *AIAA Journal* **26**, 669-681.
- Durst, F. & Wennerberg, D. 1991 Numerical Aspects on Calculation of Confined Swirling Flows with Internal Circulation, *Computation of Strongly Swirling Axisymmetric Jets*, *Int. J. Numer. Meth. Fluids* **12**, 203-224.
- Hussain, Z.D. & Hussain, A.K.M.F. 1983 Natural Instability of Free Shear Layers. *AIAA Journal* **21**, 1512-1517.

- Kailasanath, K., Gardner, J. H., Boris, J. P. & Oran, E. S. 1989 Acoustic-Vortex Interactions and Low-Frequency Oscillations in Axisymmetric Combustors, *J. Propulsion and Power*, **5**, No. 2, 24-36.
- Katta, V. R. Goss, L. P. and Roquemore, W. M. 1994 Combustion and Flame **96**, 60-74.
- Leonard, B. P. 1979 A Stable and Accurate Convective Modelling Procedure Based on Quadratic Upstream Interpolation, *Comput. Methods in Applied Mechanics and Engineering* **19**, 59-98.
- Leschziner, M. A. & Rodi, W. 1984 Computation of Strongly Swirling Axisymmetric Jets, *AIAA Journal* **22**, No. 12, 1742-1747.
- Lilley, D. G. 1977 Swirling Flows in Combustion: A Review, *AIAA Journal* **15**, No. 8, 1063-1078.
- Longmire, E. K. and Eaton, J. K. 1992 Structure of a Particle-Laden Round Jet, *J. Fluid Mech.* **236**, 217-257.
- Park, T. W. Aggarwal, S. K. & Katta, V. R. 1996 A Numerical Study Of Droplet-Vortex Interactions In an Evaporating Spray, *Int. J. of Heat & Mass Transfer*, **39**, No. 6, 741-754.
- Ribeiro, M.M. & Whitelaw, J. H. 1980 Coaxial Jets With and Without Swirl, *J. Fluid Mech.* **96**, 769-795.
- Reynolds, W. C. & Bouchard, E. E. 1981 The Effect of Forcing on the Mixing Region of a Circular Jet, *Unsteady Turbulent Shear Layer Flows*, Springer, New York, 401-411.
- Shau, Y. R., Dolling, D. S. & Choi, K. Y. 1993 Organized structure in a compressible turbulent shear layer, *AIAA Journal*, **31**, No. 8, 1398-1405.
- Sommerfeld, M. & Qui, H.-H. 1993 Characterization of Particle-Laden, Confined Swirling Flows by Phase-Doppler Anemometry and Numerical Calculation, *Int. J. Multiphase Flow* **19**, No. 6, 1093-1127.
- Spalding, D. B. 1972 A Novel Finite Difference Formulation for Difference Expressions involving both First and Second Derivatives, *Int. J. for Numerical Methods in Engineering* **4**, 551-559.
- Subbarao, E. R. & Cantwell, B. J. 1992 Investigation of a coflowing buoyant jet- experiments on the effect of Reynolds number and Richardson number. *J. of Fluid Mech.* **245**, 69-90.
- Uthuppan, J. Aggarwal, S. K., Grinstein F. F. and Kailasanath, K. 1994 Particle Dispersion in a Transitional Axisymmetric Jet: A Numerical Simulation, *AIAA Journal* **32**, 2004-2014.
- Yule, A. J. 1978 Large-Scale Structure in the Mixing Layer of a Round Jet. *J. Fluid Mech.* **89**, Part 3, 413-432.

TABLE I: TRANSPORT COEFFICIENTS AND SOURCE TERMS APPEARING IN GOVERNING EQUATIONS

Equations	Φ	Γ^Φ	S_x^Φ	S_r^Φ
Continuity	1	0	0	$\sum_k n_k \dot{m}_k$
Axial momentum	u	μ	$-\frac{\partial p}{\partial z} + (\rho_0 - \rho)g + \frac{\partial}{\partial z} \left(\mu \frac{\partial u}{\partial z} \right) + \frac{\partial}{\partial r} \left(\mu \frac{\partial v}{\partial z} \right) + \frac{\mu}{r} \frac{\partial v}{\partial z}$ $- \frac{2}{3} \left[\frac{\partial}{\partial z} \left(\mu \frac{\partial u}{\partial z} \right) + \frac{\partial}{\partial z} \left(\mu \frac{\partial v}{\partial r} \right) + \frac{\partial}{\partial r} \left(\mu \frac{\partial v}{r} \right) \right]$	$\sum_k \left(n_k \dot{m}_k u_k - n_k M_k \frac{du_k}{dt} \right)$
Radial momentum	v	μ	$-\frac{\partial p}{\partial r} + \frac{\partial}{\partial z} \left(\mu \frac{\partial u}{\partial r} \right) + \frac{\partial}{\partial r} \left(\mu \frac{\partial v}{\partial r} \right) + \frac{\mu}{r} \frac{\partial v}{\partial r} - 2\mu \frac{v}{r^2}$ $+ \rho \frac{w^2}{r} - \frac{2}{3} \left[\frac{\partial}{\partial r} \left(\mu \frac{\partial u}{\partial z} \right) + \frac{\partial}{\partial r} \left(\mu \frac{\partial v}{\partial r} \right) + \frac{\partial}{\partial r} \left(\mu \frac{v}{r} \right) \right]$	$\sum_k \left(n_k \dot{m}_k v_k - n_k M_k \frac{dv_k}{dt} \right)$
Swirl momentum	w	μ	$-\left(\frac{\mu}{r^2} + \rho \frac{v}{r} + \frac{1}{r} \frac{\partial \mu}{\partial r} \right) w$	$\sum_k \left(n_k \dot{m}_k w_k - n_k M_k \frac{dw_k}{dt} \right)$
Mass fraction of fuel	Y_f	$\rho D_{f, N_2}$	0	$\sum_k n_k \dot{m}_k$
Mass fraction of other species	Y_i ($i=1, N_2, CO_2$)	$\rho D_{i, N_2}$	0	0
Energy	H	$\frac{\lambda}{C_p}$	0	$\sum_k n_k \dot{m}_k (h_k - \ell_{k,0})$

Figure Captions

- Fig. 1: Schematic of a droplet-laden swirling jet.
- Fig. 2: Time-history plots of center-line gas velocity (figs. a and b) and axial profiles of time-averaged center-line gas velocity (fig. c) for non-swirling and swirling (swirl number $S = 0.375$) jets obtained by using two different grid sizes.
- Fig. 3: Snapshots of the flow field for a swirling jet without droplets for four different swirl numbers. In each snapshot, iso-temperature contours are plotted on the right-hand side of the symmetric jet, and streaklines on the left. For iso-temperature contours, the red and purple colors represent the highest (1200 K) and the lowest (294 K) temperatures respectively. The times of the snapshots are 0.21, 0.24, 0.25, 0.2 s for $S = 0, 0.375, 0.5$, and 0.75 respectively.
- Fig. 4: Frequency spectra of axial gas velocity for a swirling jet without droplets for different swirl numbers.
- Fig. 5: Axial profiles of time-averaged gas velocity and temperature for a swirling jet without droplets for different swirl numbers.
- Fig. 6: Time-averaged velocity vector plots for a swirling jet without droplets for different swirl numbers.
- Fig. 7: Snapshots of the flow field for a swirling jet with droplets. In each snapshot, iso-temperature contours are plotted on the right-hand side of the symmetric jet, and streaklines on the left. For iso-temperature contours, the red and purple colors represent the highest (1200 K) and the lowest (294 K) temperatures respectively.
- Fig. 8: Time history of gas-phase axial velocity for single-phase and two-phase jets with different swirl numbers.
- Fig. 9: Frequency spectra of axial gas velocity for a swirling jet with droplets for different swirl numbers.
- Fig. 10: Axial profiles of time-averaged gas velocity and temperature for a swirling jet without and with two-way momentum coupling for different swirl numbers.
- Fig. 11: Time-averaged velocity vector plots for a two-phase swirling jet for different swirl numbers

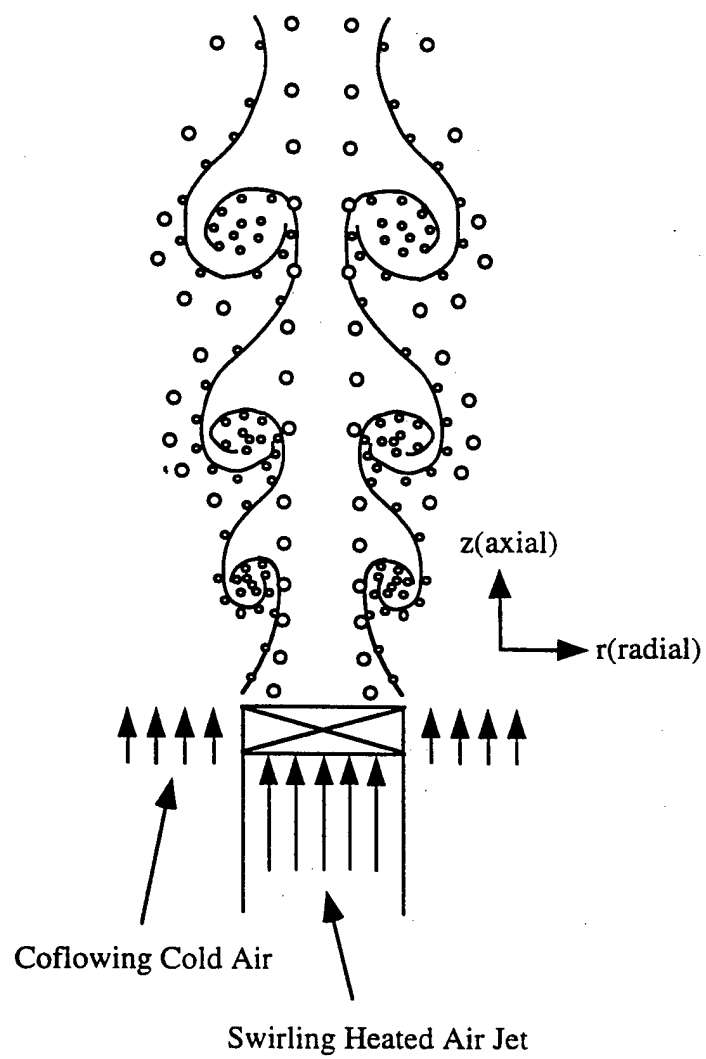
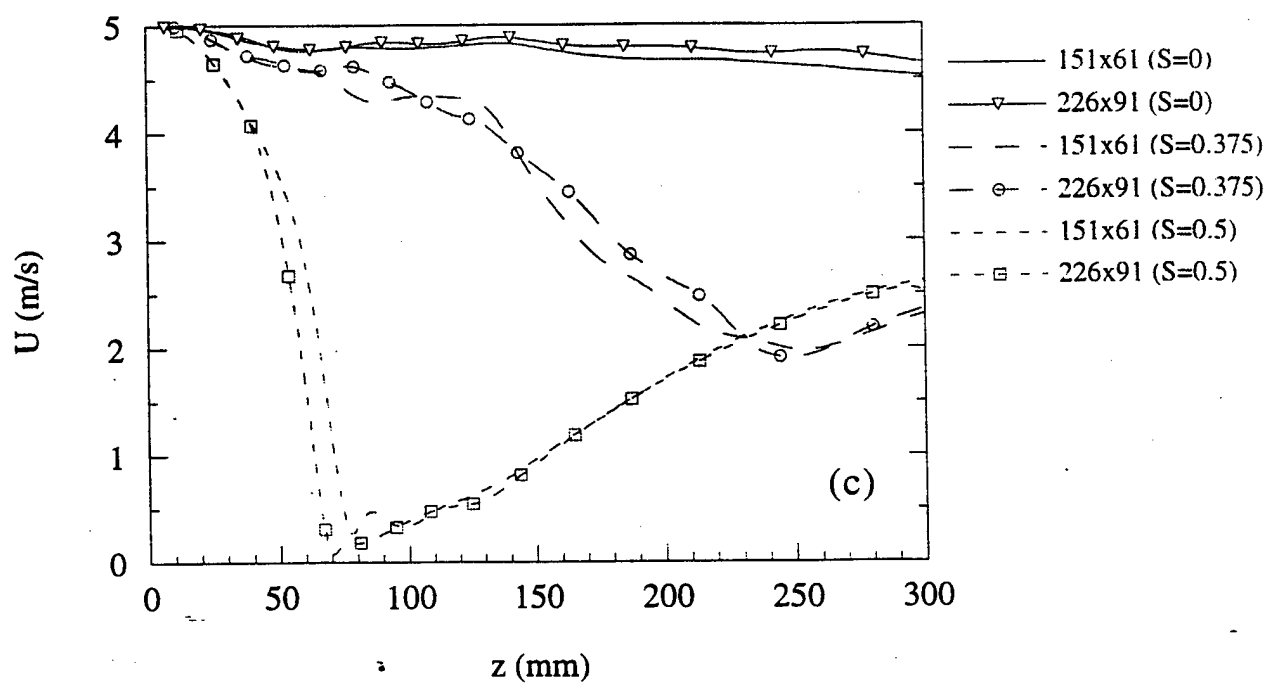
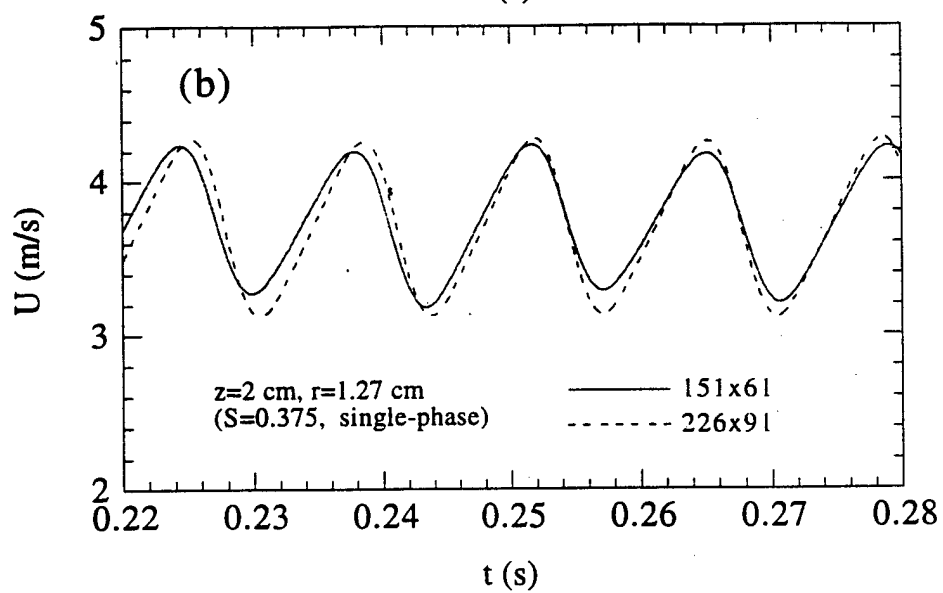
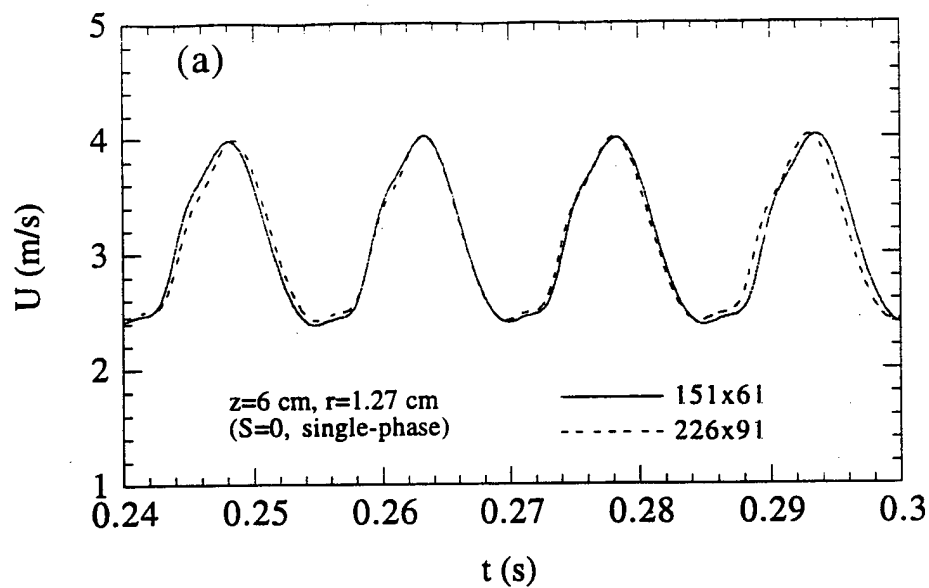
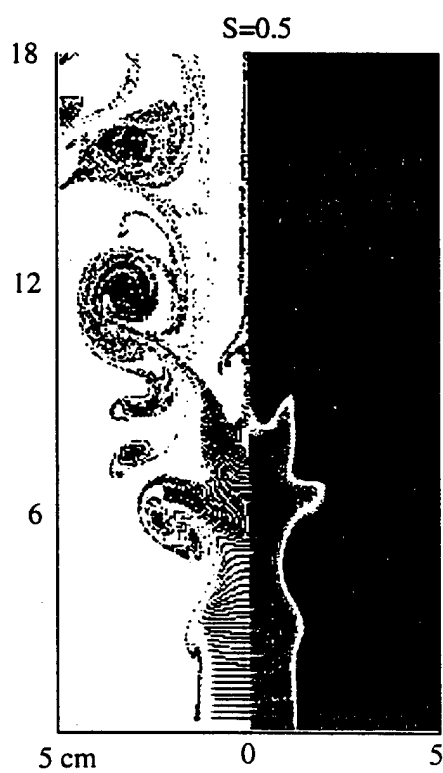
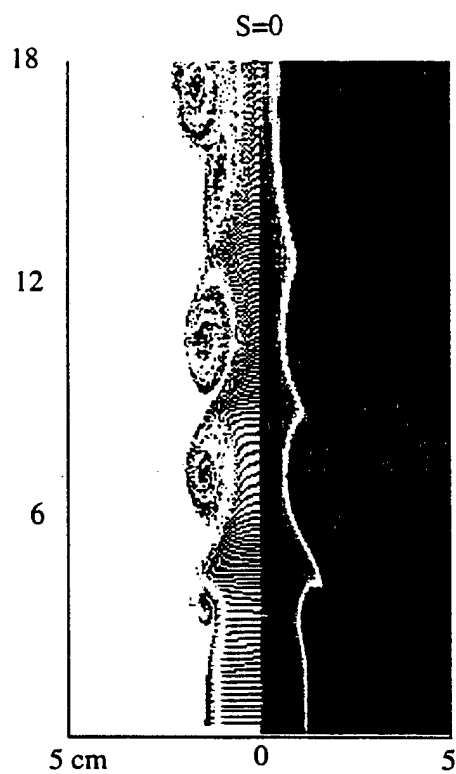
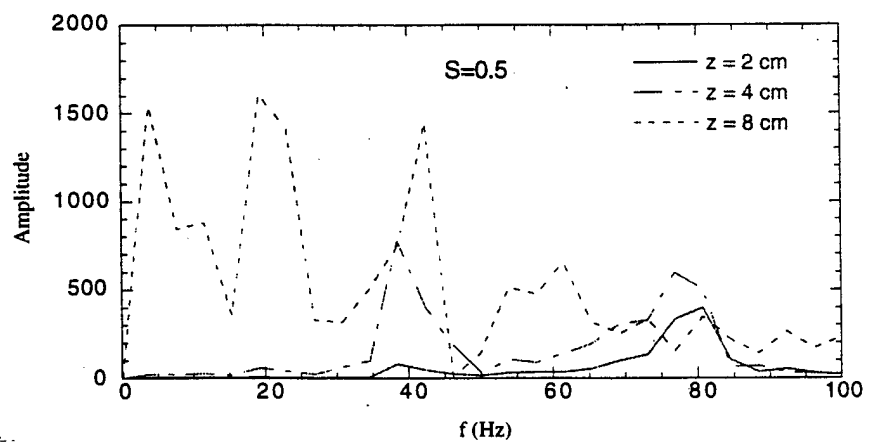
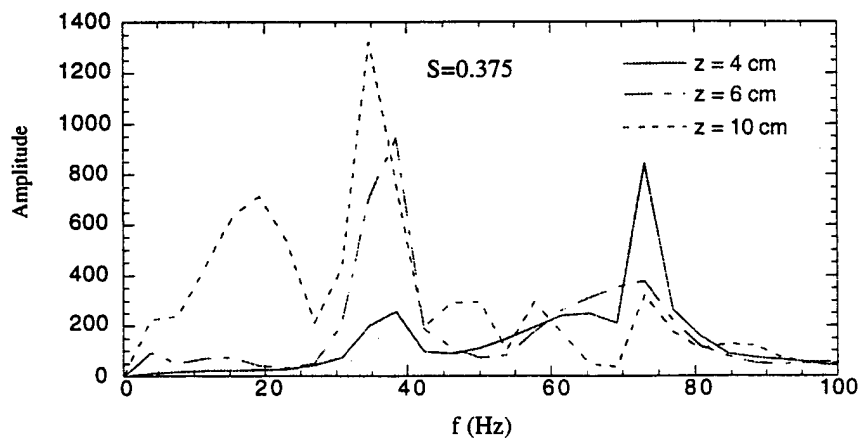
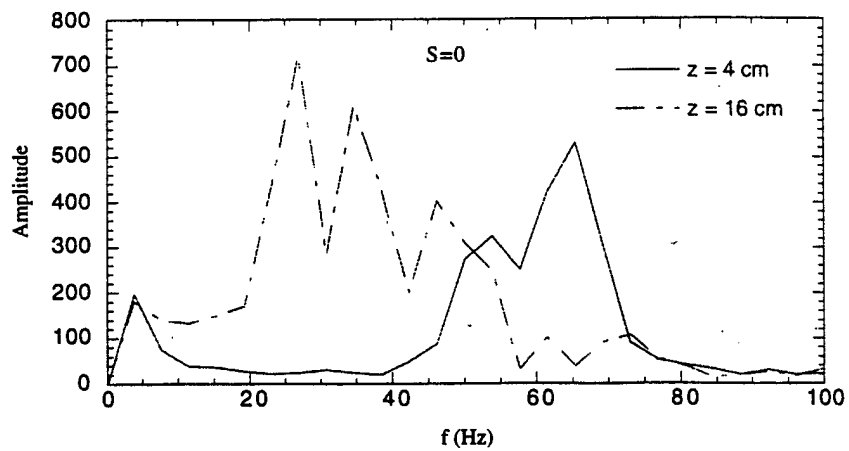
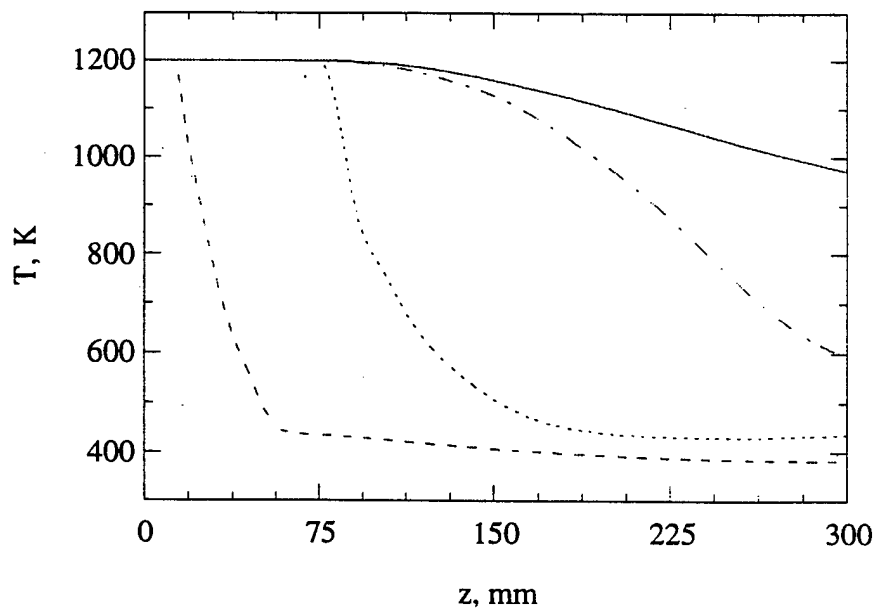
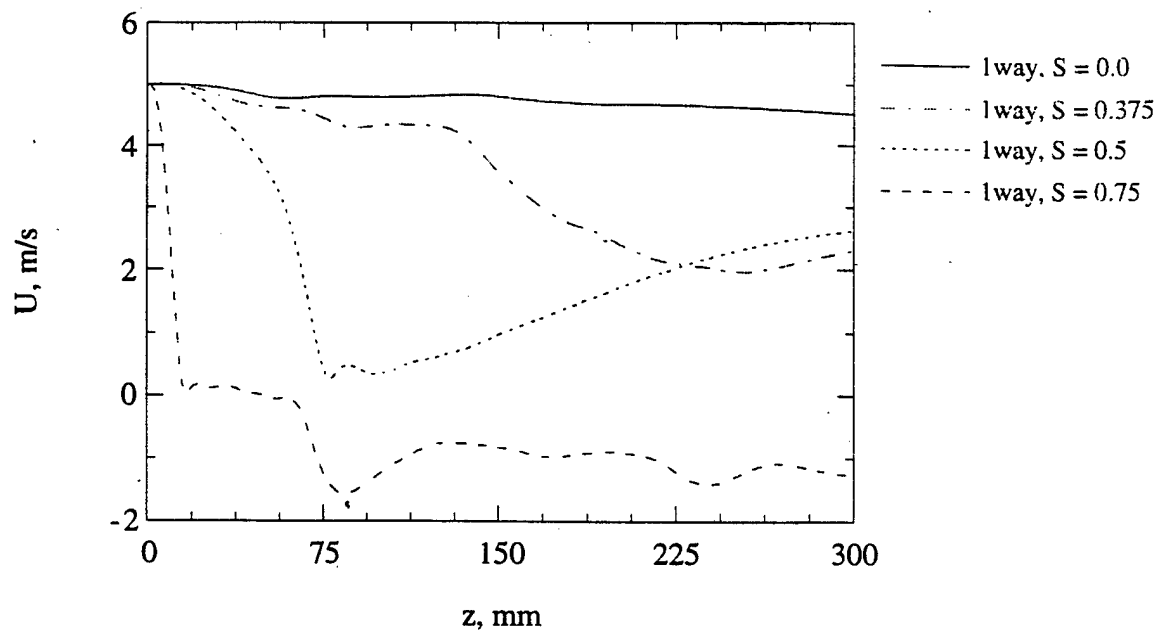


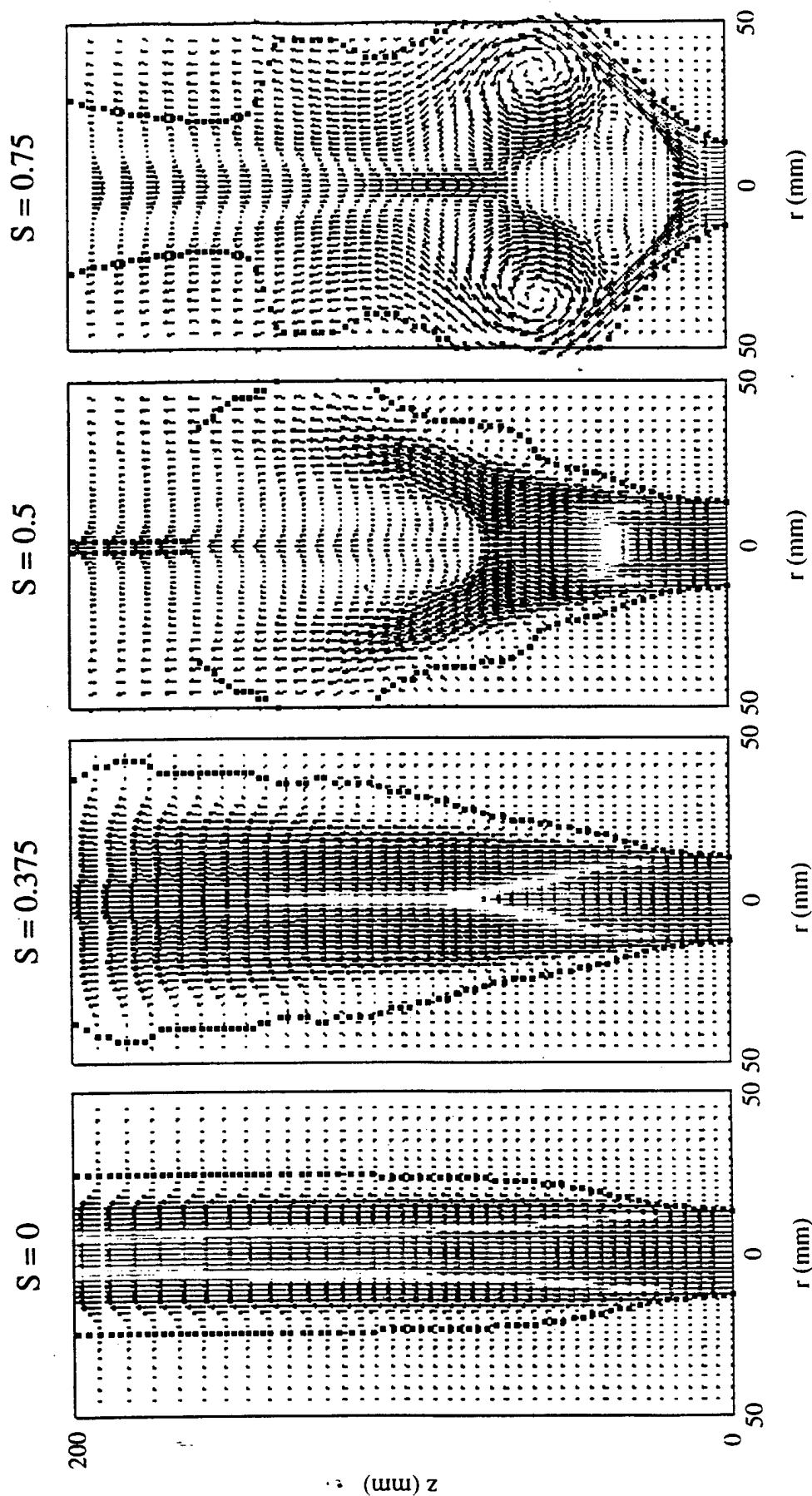
Fig. 1 Schematic of droplet-laden swirling jet.



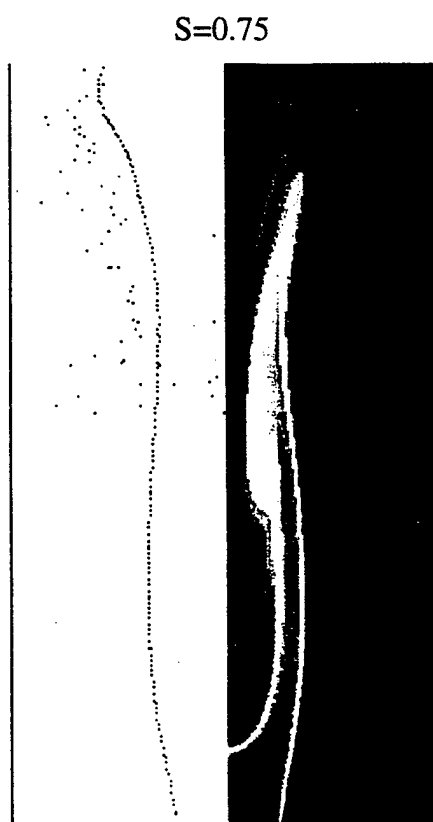
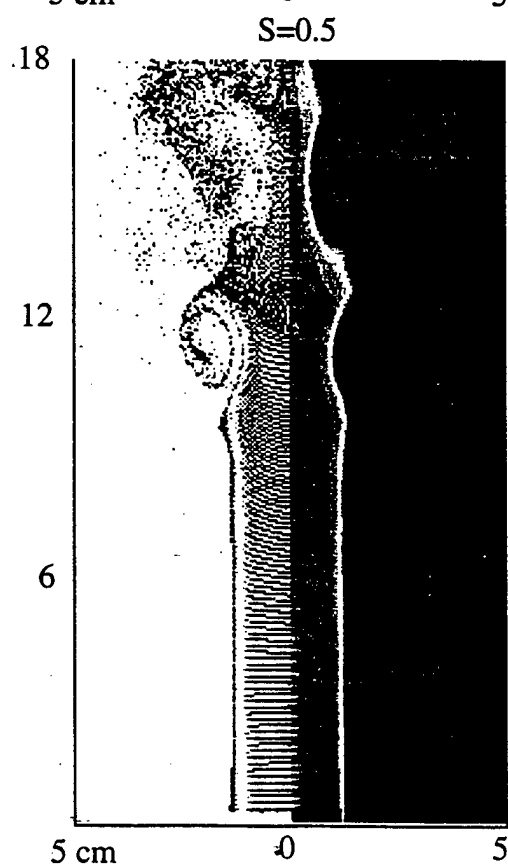
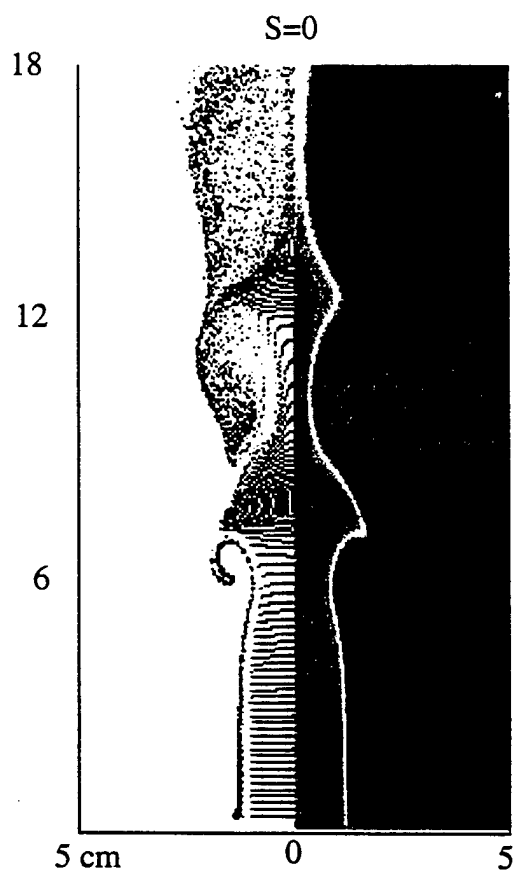








Two-way Coupling



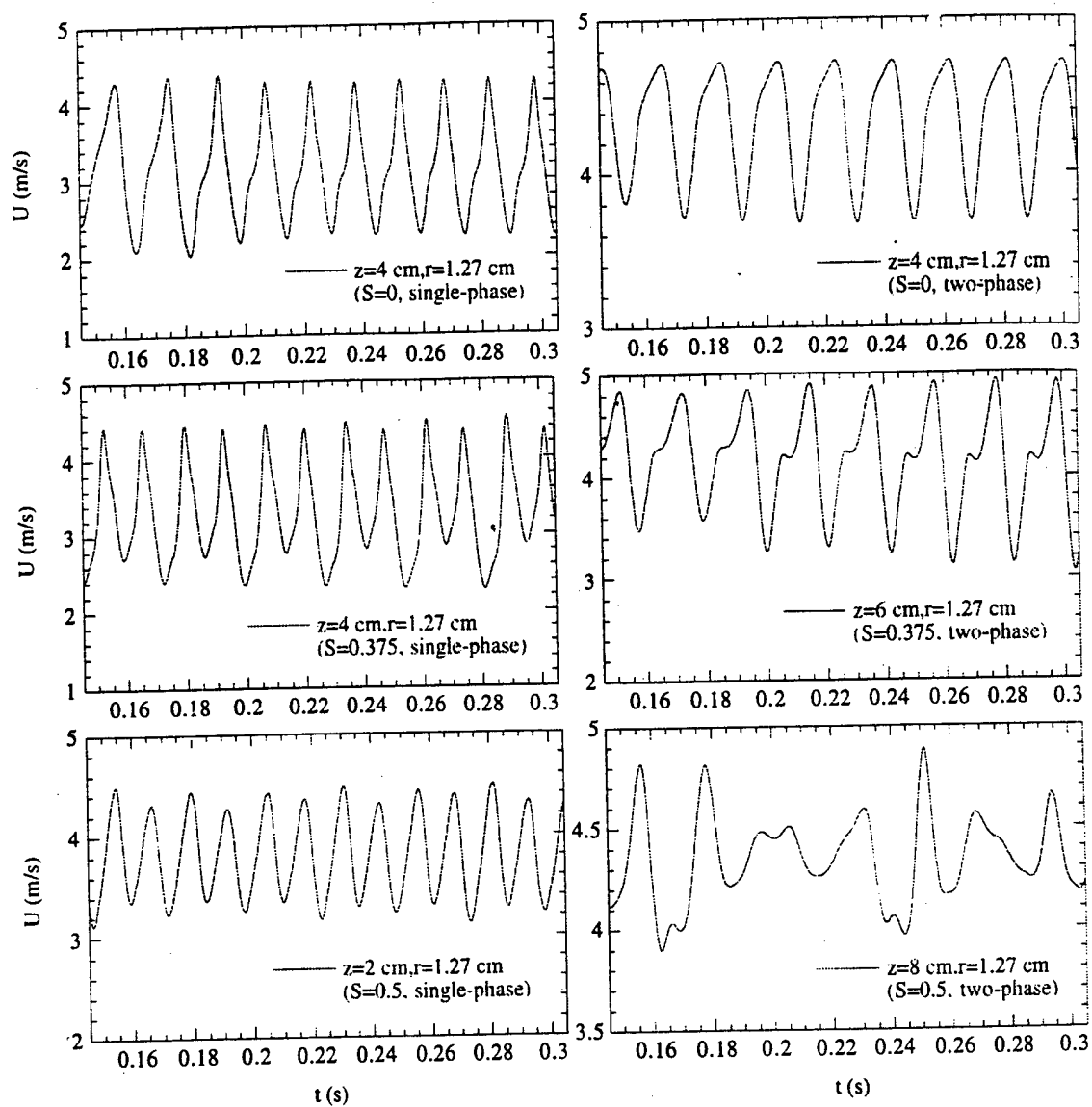


Fig. 8 Time history of gas-phase axial velocity for six different cases.

